# SYSTEMATIC SEARCH FOR EXTREME BEHAVIOR IN 3D NAVIER-STOKES FLOWS BASED ON THE LADYZHENSKAYA-PRODI-SERRIN CONDITIONS

By ELKIN WBEIMAR RAMÍREZ, M.Sc.

A Thesis Submitted to the School of Graduate Studies in Partial Fulfilment of the Requirements for or the Degree of Doctor of Philosophy

McMaster University © Copyright by Elkin Ramírez, October 2025

#### Abstract

One of the most famous problems in theoretical fluid mechanics concerns the question whether the 3D Navier-Stokes equations always produce smooth solutions. More specifically, it is not known whether all sufficiently smooth initial data lead to the existence of regular solutions for all time or if singularities may form in finite time. One approach to study this problem is based on the so called "conditional regularity results"; if such statements are shown to hold, this would imply that the corresponding flows are regular and satisfy the Navier-Stokes system in the classical sense. Arguably, the best known result of this type is the enstrophy condition. It has inspired recent works attempting to search for initial conditions that maximize the enstrophy over a certain time window to identify the worst-case scenarios that could result in singularity formation in finite time. Motivated by these studies, in this investigation we conduct a systematic computational search for potential singularities in three-dimensional Navier-Stokes flows using the Ladyzhenskaya-Prodi-Serrin conditions. They assert that for a solution  $\mathbf{u}(t)$  of the Navier-Stokes system to be regular on an interval [0,T], the integral  $\int_0^T \|\mathbf{u}(t)\|_{L^q(\Omega)}^p dt$ , where 2/p + 3/q = 1, q > 3, must be bounded. Our main contribution is to conduct a systematic search for flows that might become singular and violate this condition, by solving a family of variational PDE optimization problems on a periodic domain  $\Omega$ . In these problems, we identify initial conditions  $\mathbf{u}_0$  that locally maximizes the integral  $\int_0^T \|\mathbf{u}(t)\|_{L^q(\Omega)}^p dt$  for a range of different values of q and p, different time windows T and several sizes  $\|\mathbf{u}_0\|_{L^q(\Omega)}$  of the initial data. Such local maximizers are found numerically with a state-of-the-art adjoint-based Riemannian gradient method. Four formulations are considered with optimal solutions sought in Hilbert-Sobolev and Lebesgue function spaces. This is the first time the worst-case behavior of Navier-Stokes flows is thoroughly investigated through the lens of the Ladyzhenskaya-Prodi-Serrin conditions. In order to study how a hypothetical singularity could develop, we analyze the rate of growth of  $\|\mathbf{u}(t)\|_{L^{q}(\Omega)}$  and of the enstrophy in the extreme flows obtained by solving the optimization problems. We derive and analyze explicit bounds on the rate of growth for the  $L^q(\Omega)$  norm of Navier-Stokes flows for which singularity formation is impossible. By combining them with existing bounds on the rate of growth of  $\|\mathbf{u}(t)\|_{L^q(\Omega)}$ , we identify specific regimes such that if the corresponding rate of growth is sustained, this would lead to singularity formation in finite time in Navier-Stokes flows. Although we did not find any evidence for blow-up, these relations allow us to quantify how "close" the extreme flows arising in such worst-case scenarios come to producing a singularity.

# Acknowledgments

I would like to express my deepest gratitude to my supervisor, Dr. Bartosz Protas, for his time, guidance, and unconditional support throughout this journey. Although the path has not been easy, I never felt alone, thanks to him. Since I started working with him as a Master's student, he provided me with constructive feedback and valuable advice that have brought me to this point in life. Without his support, this work would not have been possible. I also would like to thank my supervisory committee members, Dr. Dmitry Pelinovsky and Dr. Nicholas Kevlahan, for their time spent reading this thesis, as well as their questions and comments, which have helped improve this work. I would like to express my special thanks to Dr. John Bowman for his insightful comments that have greatly enhanced this work.

I also wish to extend my gratitude to current and former postdocs, Dr. Fabian Bleitner, Dr. Di Kang, and Dr. Xinyu Zhao, for their assistance in various aspects of this thesis.

I would like to thank MITACS for granting me with a Globalink Research Award, which took me to Tokyo. Special thanks to Dr. Tsuyoshi Yoneda for welcoming me to Japan, for making my stay smooth, and for all the weekly discussions we had. I also want to thank Dr. Zhongyang Gu for the enlightening conversations and the great dinners we enjoyed around Tokyo after work.

I extend my thanks to the Department of Mathematics for providing me with financial support during my time at McMaster University. Special thanks to Dr. Aaron Childs and Dr. Adam Van Tuyl for always being there whenever I had teaching-related questions. Many thanks to Emily, Julie and Rabia for all their help with administrative matters.

I wish to thank to Digital Research Alliance of Canada for providing the computational resources and hardware support that were essential for the completion of this research.

I have special gratitude to McMaster University, for giving me the opportunity to come to Canada and for providing a safe environment to pursue my studies. Thanks to this, I have met wonderful people who have made my time in Hamilton incredibly meaningful. In particular, I want to thank my friends Jie, Lizbeth, Mariana, Subhajit, Uyen and Carlos for always being there during both the good and difficult times.

Last but certainly not least, I want to thank my family for their unconditional love and support during the preparation of this thesis. Thank you to my sister, Aura Elena; my nephew, Mathías; my aunt, Sandra Liliana; and my cousins, Maria Paula and Dairon, for your enduring presence in my life. Finally, thanks to my mother, Rosa Elena, for her boundless love, support, and countless memories we have shared, specially on our trips. Her constant encouragement has been the foundation of my journey, and this accomplishment is as much hers as it is mine.

# Contents

1	Intr	ntroduction				
2	Conditional Regularity Results					
	2.1	Definitions of Key Quantities	8			
<ul><li>2.2 Some Key Results</li></ul>			11			
			12			
		2.3.1 The Enstrophy Condition	13			
		2.3.2 Ladyzhenskaya-Prodi-Serrin Conditions	17			
	2.4	A Priori Bounds for $\frac{d}{dt} \ \mathbf{u}(t)\ _{L^q(\Omega)}$	18			
		2.4.1 Gibbon's Conditions	21			
	2.5	Properties of Weak Solutions	22			
3	Optimization Formulations 24					
3.1 Motivation		Motivation	24			
	3.2	Choice of the Lebesgue and Sobolev Spaces	25			
	3.3	Optimization Problems	26			
4 Solution Approach		ıtion Approach	<b>2</b> 9			
	4.1	The Steepest Ascent Method	29			
	4.2	Riemannian Optimization	30			
	4.3	Evaluation of the Gradient	33			

Ph.	D.	Thesis	– Elkin Ramírez	McMaster University		
		4.3.1	Gradient in $L^2$			
		4.3.2	Gradient in the Sobolev Space $H^s$			
		4.3.3	Gradient in the Lebesgue Space $L^q$			
4	1.4	Limiti	$ng Case q = 3 \dots \dots \dots \dots$			
4	4.5	Projec	tion, Retraction and Arc-Maximization			
4	4.6					
		4.6.1	Hilbert Space Formulation	43		
		4.6.2	Riemannian Optimization	44		
		4.6.3	Riemannian Formulation in a Lebesgue Space	ce 46		
4	1.7	Nume	rical Implementation	47		
		4.7.1	Discretization in Space	47		
		4.7.2	Discretization in Time	49		
<b>5</b> I	Numerical Results					
Ę	5.1	Extre	mal Flows in $L^4(\Omega)$			
		5.1.1	Branches of Local Maximizers	57		
		5.1.2	Structure of the Extremal Flows	62		
Ę	5.2	Extre	mal Flows in $L^5(\Omega)$	69		
		5.2.1	Branches of Local Maximizers			
		5.2.2	Structure of the Extremal Flows			
Ę	5.3	Extre	mal Flows in $L^9(\Omega)$			
		5.3.1	Branches of Local Maximizers	87		
		5.3.2	Structure of the Extremal Flows	90		
Ę	5.4	Extre	mal Flows in $L^3(\Omega)$	93		
		5.4.1	Branches of Local Maximizers	97		
		5.4.2	Structure of the Extremal Flows	102		
Ę	5.5	Diagn	ostic Quantities in the Extremal Flows	107		

Ph.D. Thesis – Elkin Ramírez	McMaster University
6 Summary and Conclusions	111
A Rederivation of Inequality (2.31)	117
B Proof of Theorem 6.1	119
C Validation of the Gradients	121

# Chapter 1

## Introduction

One of the most important models in the field of fluid dynamics are the Navier-Stokes equations. They are essential for studying fluid flows in different applications across a wide range of spatio-temporal scales, from representing blood flow to helping design bioartificial pancreas [56] to modeling tsunami waves [57], numerical weather prediction [49] and aircraft design [19], in addition to many other important applications. In this thesis, we will consider the incompressible Navier-Stokes system defined on the 3D torus  $\Omega = \mathbb{T}^3 := \mathbb{R}^3/\mathbb{Z}^3$ , where ":=" means "equal to by definition", with periodic boundary conditions

$$\partial_t \mathbf{u} + (\mathbf{u} \cdot \nabla_{\mathbf{x}}) \mathbf{u} + \nabla_{\mathbf{x}} p - \nu \Delta \mathbf{u} = 0$$
 in  $\Omega \times (0, T]$ , (1.1a)

$$\nabla_{\mathbf{x}} \cdot \mathbf{u} = 0$$
 in  $\Omega \times [0, T]$ , (1.1b)

$$\mathbf{u}(0) = \mathbf{u}_0, \tag{1.1c}$$

where the vector  $\mathbf{u} = [u_1, u_2, u_3]^T$  is the velocity field, p is the pressure,  $\nu > 0$  is the coefficient of kinematic viscosity,  $\nabla_{\mathbf{x}}$  denotes the gradient with respect to the space variable  $\mathbf{x} = [x_1, x_2, x_3]^T$  (this notation is needed to distinguish it from another notion of a gradient that will be introduced later) and  $\mathbf{u}_0$  is the initial condition. The velocity gradient  $\nabla_{\mathbf{x}} \mathbf{u}$  is a tensor with components  $[\nabla_{\mathbf{x}} \mathbf{u}]_{ij} = \partial_j u_i$ , i, j = 1, 2, 3. For

simplicity and unless stated otherwise, both the fluid density  $\rho$  and the viscosity  $\nu$  are assumed to be equal to unity ( $\nu = 1$ ,  $\rho = 1$ ). The choice of this domain  $\Omega$  is motivated by our interest in intrinsic mechanisms governing flow evolution, without considering interactions with the boundary.

As it is usual in the theory of Partial Differential Equations (PDEs), several notions of solutions are often defined in order to study their most fundamental properties: existence, uniqueness and regularity. These general properties are important as they determine whether or not a given mathematical model is well posed and can therefore serve as a description of natural phenomena. For the Navier-Stokes system (1.1), one typically works with strong (or classical) solutions, mild and weak solutions, including Leray-Hopf weak solutions. Classical or strong solutions are time-dependent vector fields  $\mathbf{u}(\mathbf{x},t)$  with enough regularity to directly satisfy the PDE at each point in time and space. Weak solutions, however, may lack in smoothness and can be defined in several ways depending on how regular the velocity field  $\mathbf{u}$  should be, which is determined by how one performs integration by parts. Here, we define weak solutions as vector fields  $\mathbf{u}$  that satisfy the following identity [13, 51]

$$\int_{0}^{s} -\langle \mathbf{u}, \partial_{t} \boldsymbol{\varphi} \rangle dt + \int_{0}^{s} \langle \mathbf{\nabla}_{\mathbf{x}} \mathbf{u}, \mathbf{\nabla}_{\mathbf{x}} \boldsymbol{\varphi} \rangle dt + \int_{0}^{s} \langle (\mathbf{u} \cdot \mathbf{\nabla}_{\mathbf{x}} \mathbf{u}, \boldsymbol{\varphi}) dt = \langle \mathbf{u}_{0}, \boldsymbol{\varphi}(0) \rangle - \langle \mathbf{u}(s), \boldsymbol{\varphi}(s) \rangle, \quad (1.2)$$

for all test functions  $\varphi$  and almost every s > 0. Here,  $\langle f, g \rangle := \int_{\Omega} f(\mathbf{x}) \cdot g(\mathbf{x}) d\mathbf{x}$  is the  $L^2$  inner product and test functions belong to the set

$$\left\{\boldsymbol{\varphi}\in C_c^{\infty}(\Omega\times[0,\infty)):\boldsymbol{\nabla}_{\mathbf{x}}\cdot\boldsymbol{\varphi}(t)=0\quad\text{for all}\quad t\in[0,\infty)\right\},$$

where  $C_c^{\infty}(\Omega \times [0, \infty))$  is the space of infinitely differentiable functions with compact support on  $\Omega \times [0, \infty)$ . If, in addition, the weak solution **u** satisfies the energy inequality

$$\frac{1}{2} \|\mathbf{u}(t)\|_{L^{2}(\Omega)}^{2} + \int_{0}^{t} \|\mathbf{\nabla}_{\mathbf{x}} \,\mathbf{u}(\tau)\|_{L^{2}(\Omega)}^{2} \,d\tau \le \frac{1}{2} \|\mathbf{u}(0)\|_{L^{2}(\Omega)}^{2},\tag{1.3}$$

for almost all times  $t \in (0, \infty)$ , **u** is called a Leray-Hopf weak solution of the Navier-Stokes system. In expression (1.3),  $\|\cdot\|_{L^2(\Omega)}$  is the norm in the  $L^2(\Omega)$  space induced by the  $L^2$  inner product defined above. We can find other definitions of weak solutions in the literature, however, in the present work we will focus on weak solutions of the Leray-Hopf type.

The study of the existence and uniqueness of Navier-Stokes flows dates back to the beginning of the 20th century, but the problem still lacks resolution. Due to the wide variety of applications of this set of equations, ranging from physics to engineering, it is of an extreme importance to build a solid mathematical framework concerning the existence and uniqueness of their solutions. In fact, this is one of the 'millennium problems' named by the Clay Mathematics Institute [18]. It can stated as follows: given a smooth initial vector field  $\mathbf{u}_0$ , does system (1.1) have a unique classical solution that exists for all t > 0? The question can be addressed on a periodic domain or  $\mathbb{R}^3$ .

Major progress concerning the existence of weak solutions on  $\mathbb{R}^3$  was made by Leray in 1934 [32]. Later in 1951, Hopf [25] established global existence of weak solutions, but without uniqueness, on bounded domains. It is worth mentioning that inequality (1.3) holds for the weak solutions that Hopf and Leray considered. In 1959, J.-L. Lions [33] proved global existence and uniqueness of Leray-Hopf weak solutions of the Navier-Stokes equations with hyper-viscosity i.e., he considered equation (1.1a) with the Laplacian  $\Delta$  replaced with the fractional Laplacian  $(-\Delta)^{\theta}$  with  $\theta \geq 5/4$ . As regards uniqueness, Luo & Titi (2020) [38] proved non uniqueness of weak solutions with finite kinetic energy for  $\theta < 5/4$ . This implies that  $\theta = 5/4$  is a critical value with respect to uniqueness of weak solutions. However, uniqueness of Leray-Hopf weak solutions is a problem that remains open. In 2022, Albitron, Brué & Colombo [3] were able to prove non uniqueness of Leray-Hopf weak solutions in the 3D Navier-Stokes system with a time-dependent force. They also showed that, if the source term has a certain form, it might lead to blow up. In the same year, 2022, Hou [27] presented numerical evidence

of a potentially singular behavior of solutions to the 3D Navier-Stokes equations in a cylindrical domain periodic in the axial direction which was verified by applying the enstrophy and the Ladyzhenskaya-Prodi-Serrin conditions. This is an intriguing result that motivates a systematic search for singularities in the Navier-Stokes system.

One approach to study the regularity of Leray-Hopf weak solutions of the Navier-Stokes equations (1.1) is by using the so-called "conditional regularity results". These are conditions, which if met by the weak solutions, will ensure the regularity of these solutions. In Chapter 2, we will discuss some conditional regularity results that we will use in this thesis in detail, namely, the enstrophy [20] and the Ladyzhenskaya-Prodi-Serrin [51] conditions.

Although solving the problem of existence and uniqueness of solutions for the Navier-Stokes equations is a mathematical analysis question, several computational studies have been carried out exploring the possibility of a finite-time blow-up in the 3D setting. Some of these investigations are Brachet [11] and Orlandi, Pirozzoli & Carnevale [43]. However, no evidence for blow-up has been found from the computations.

Another model that has received considerable attention is the inviscid Euler system obtained by setting the viscosity  $\nu = 0$  in the 3D Navier-Stokes equation (1.1)

$$\partial_t \mathbf{u} + (\mathbf{u} \cdot \nabla_{\mathbf{x}}) \mathbf{u} = -\nabla_{\mathbf{x}} p \quad \text{in } \Omega \times (0, T],$$
 (1.4a)

$$\nabla_{\mathbf{x}} \cdot \mathbf{u} = 0$$
 in  $\Omega \times [0, T]$ , (1.4b)

$$\mathbf{u}(0) = \mathbf{u}_0,\tag{1.4c}$$

where  $\Omega$ , p, T,  $\mathbf{u}_0$  are as in (1.1). It describes the dynamics of incompressible ideal fluids. Unlike for the Navier-Stokes equations, there is some numerical evidence of blow-up for the 3D inviscid Euler equations while using certain type of initial data, Luo & Hou [36, 37].

A novel method to tackle certain questions related to understanding the extreme and possibly singular behavior in Navier-Stokes flows was introduced by Doering & Lu in [34]. Recognizing that the regularity of classical solutions to the 3D Navier-Stokes system is controlled by the enstrophy, they proposed a variational optimization problem to study the sharpness of an a priori estimate on the rate of growth of enstrophy. More specifically, they studied the maximum rate of growth of enstrophy, not only for the Navier-Stokes equations, but also for the 1D Burgers equation. This method was later adopted and expanded by Ayala & Protas [6, 7], where they analyzed the sharpness of various energy-type a priori estimates for the 1D Burgers and 2D Navier-Stokes equations. Although these two systems are known to be globally well-posed under certain conditions, understanding the sharpness of those estimates could provide insights also for the 3D Navier-Stokes problem. Kang et al. also adapted the method in [29, 28]. They worked with the 3D Navier-Stokes equations this time and searched for initial data that could potentially produce finite-time singularities by considering the enstrophy and the Ladyzhenskaya-Prodi-Serrin conditions. Zhao & Protas [59] also used the same idea but in the context of the 3D Euler equations, where they presented numerical evidence of a possible singularity in finite time. An overview of the research program focusing on a systematic search for extreme and singular behavior in the Navier-Stokes and other models can be found in [47].

In this thesis, we are extending Kang's & Protas' work [28]. They analyzed extreme behavior in Navier-Stokes flows using the Ladyzhenskaya-Prodi-Serrin conditions. They formulated several optimization problems in order to identify initial conditions that maximize a certain quantity controlling the regularity of solutions. As a limitation of their approach, they focused on finding initial conditions within a certain Sobolev space with Hilbert structure embedded in the Lebesgue space  $L^q(\Omega)$  in which the optimization problem would otherwise be naturally formulated. This simplification was crucial for the solution of the optimization problems, using a gradient descent method. The presence of an inner product allowed them to define the gradient directly using the Riesz theorem based on the solution of the adjoint system. In our study, however, we will take a different approach. Our optimization problems will be formulated

within more general function spaces, namely, suitable Lebesgue spaces. In addition to formulating the optimization problems in a different, larger, function space, we will also analyze a large family of the Ladyzhenskaya-Prodi-Serrin conditions. The lack of Hilbert structure significantly complicates the solution of the optimization problem from the numerical point of view, specially while evaluating the gradient. Therefore, we will have to compute the gradient using different tools, adopting ideas from Protas [46].

In terms of technical innovations, our two main contributions are the development of an efficient computational approach to solve PDE optimization problems formulated on function spaces without Hilbert structure and identification of the regimes of the rate of growth of the different  $L^q(\Omega)$  norms where a singularity will occur. Firstly, we consider a Riemannian gradient descent method on a Hilbert space, and extend it to the more general case of Banach spaces. The mathematical problems considered are generalizations of the problems studied by Kang & Protas [28, 46]. Although a novel conjugate gradient method is also introduced to tackle constrained optimization problems in Banach spaces, it will not be used to produce results in this document for reasons that will be explained later. Secondly, we examine well-known a priori bounds on integrals of the  $L^q(\Omega)$  norm of the solutions of the Navier-Stokes equations and derive conditions under which singularities cannot form. This allows us to identify growth rate regimes of the  $L^q(\Omega)$  norm, where the solution must lie if a singularity is to develop. These conditions will serve as a useful indicator on how "close" the extreme flows found by solving optimization problems come to forming a singularity.

Although we found no numerical evidence of unbounded growth for Navier-Stokes flows in the  $L^q(\Omega)$  spaces, this research provides insights into how flows that maximize objective functionals based on the Ladyzhenskaya-Prodi-Serrin conditions behave when subject to constraints in Lebesgue spaces, as well as in Sobolev spaces embedded within the latter spaces. In both cases, we construct sequences of initial conditions that

approach optimal solutions locally maximizing the objective functionals. We observe that initial conditions become less regular as we approach local maximizers. In general, we found that optimal initial conditions in the Sobolev-Hilbert spaces produce larger values of the objective functional compared to those found in the Lebesgue spaces. Additionally, we established that local maximizers in the Sobolev-Hilbert spaces are also local maximizers in the Lebesgue spaces.

The structure of this thesis is as follows: In Chapter 2, we will define key quantities and state certain well-known conditional regularity conditions, namely, the enstrophy and Ladyzhenskaya-Prodi-Serrin conditions. Additionally, we will introduce some a priori bounds for the norms of the Navier-Stokes flows in Lebesgue spaces together with their rates of change; in Chapter 3, we will formulate our optimization problems, emphasizing how these formulations generalize those used by Kang & Protas; then, in Chapter 4, we will discuss numerical approaches to solving optimization problems on general Banach spaces, particularly, on Lebesgue spaces; two main methods are studied here: the gradient descent method and the conjugate gradient method; it will be also explained in detail how to evaluate such gradients in both Sobolev and Lebesgue spaces; finally, in Chapter 5, we will present our main numerical results and compare them with what was found in earlier studies.

# Chapter 2

# Conditional Regularity Results

In this chapter, we will first state relevant definitions and theorems [2] followed by a summary of some conditional regularity results for the Navier-Stokes equations. Additionally, we will present some known bounds for the norms of solutions of the Navier-Stokes equations in Lebesgue spaces. Furthermore, we identify growth rate regimes of the  $L^q(\Omega)$  norm of the velocity such that, if a solution of the Navier-Stokes system (1.1) is to develop a singularity, the rate of growth of the norm must fall within these regimes. For brevity, the space, and occasionally time, dependence of certain vector fields is sometimes omitted when it does not cause confusion. Although  $\nu$  was set equal to 1 in the previous chapter, in the interest of generality in this section we derive estimates in which explicit dependence on  $\nu$  is retained.

## 2.1 Definitions of Key Quantities

Relevant definitions used in this thesis are presented below.

**Definition 2.1** (Lebesgue space). We denote

$$L^q(\Omega) := \left\{ \boldsymbol{f}: \Omega \to \mathbb{R}^3: \boldsymbol{f} \text{ is measurable and } \|\boldsymbol{f}\|_{L^q(\Omega)} < \infty \right\}$$

where  $q \in [1, \infty]$  and the norm is defined as

$$\|\boldsymbol{f}\|_{L^{q}(\Omega)} := \left(\int_{\Omega} |\boldsymbol{f}(\mathbf{x})|^{q} d\mathbf{x}\right)^{\frac{1}{q}} \tag{2.1}$$

for  $1 \le q < \infty$  and

$$\|\mathbf{f}\|_{L^{q}(\Omega)} := \operatorname{ess\,sup}_{\mathbf{x} \in \Omega} |\mathbf{f}(\mathbf{x})|,$$

$$= \inf \{ a \in \mathbb{R} : \mu \left( \{ \mathbf{x} \in \Omega : |\mathbf{f}(\mathbf{x})| \ge a \} \right) = 0 \}$$
(2.2)

for  $q=\infty$ , in which  $|\cdot|$  and  $\mu$  denote the Euclidean vector norm and the Lebesgue measure, respectively.

**Definition 2.2.** The Fourier expansion of a real-valued function  $f \in L^1(\Omega)$  has the form

$$f(\mathbf{x}) = \sum_{k \in \mathbb{Z}^3} \widehat{f}_k \, e^{2\pi i k \cdot \mathbf{x}},\tag{2.3}$$

where  $\hat{\boldsymbol{f}}_{\boldsymbol{k}} \in \mathbb{C}, \, \boldsymbol{k} \in \mathbb{Z}^3$ , are the Fourier coefficients of  $\boldsymbol{f}$  defined as

$$\widehat{\boldsymbol{f}}_{k} = \int_{\Omega} e^{-2\pi i \boldsymbol{k} \cdot \mathbf{x}} \boldsymbol{f}(\mathbf{x}) \, d\mathbf{x}. \tag{2.4}$$

**Definition 2.3.** For  $s \geq 0$ , the Sobolev space  $H^s(\Omega)$  is defined as

$$H^{s}\left(\Omega\right):=\left\{ oldsymbol{f}\in L^{2}\left(\Omega\right):\|oldsymbol{f}\|_{H^{s}\left(\Omega\right)}^{2}<\infty
ight\} ,$$

where the norm of f is defined in terms of its Fourier coefficients as

$$\|\mathbf{f}\|_{H^{s}(\Omega)}^{2} := \sum_{\mathbf{k} \in \mathbb{Z}^{3}} \left[ 1 + (2\pi k)^{2} \right]^{s} |\widehat{\mathbf{f}}_{\mathbf{k}}|^{2},$$
 (2.5)

where  $k := |\mathbf{k}|$ .

It is useful to define the seminorm  $\|\cdot\|_{\dot{H}^s(\Omega)}$  as the expression

$$\|\boldsymbol{f}\|_{\dot{H}^{s}(\Omega)}^{2} := \sum_{\boldsymbol{k} \in \mathbb{Z}^{3}} (2\pi k)^{2s} |\widehat{\boldsymbol{f}}_{\boldsymbol{k}}|^{2}, \tag{2.6}$$

for any  $\mathbf{f} \in H^s(\Omega)$ .

**Definition 2.4** (Gevrey class). For  $\sigma$ , s > 0 given, we define the Gevrey class  $G^{\sigma}$  as the set of all divergence-free functions  $\mathbf{f} \in C^{\infty}(\Omega)$  (the space of functions continuously differentiable infinitely many times) such that they admit a Fourier series representation (2.3), and

$$\sum_{\boldsymbol{k}\in\mathbb{Z}^3}e^{2\sigma(2\pi\,k)^{2s}}\;|\widehat{\boldsymbol{f}}_{\boldsymbol{k}}|^2<\infty.$$

We can think the Gevrey class as a bridge between  $C^{\infty}$  and analytic functions, for which the Fourier coefficients vanish exponentially fast as  $k \to \infty$ .

**Definition 2.5** (Enstrophy). The enstrophy<sup>1</sup> of a time-dependent velocity field  $\mathbf{u}(t)$  is defined as

$$\mathcal{E}(\mathbf{u}(t)) := \frac{1}{2} \int_{\Omega} |\boldsymbol{\omega}(\mathbf{x}, t)|^2 d\mathbf{x} = \frac{1}{2} \|\boldsymbol{\omega}(t)\|_{L^2(\Omega)}, \tag{2.7}$$

where  $\boldsymbol{\omega}(\mathbf{x},t) := \nabla_{\mathbf{x}} \times \mathbf{u}(\mathbf{x},t)$  is the vorticity of  $\mathbf{u}$ .

For incompressible flows with periodic or no-slip boundary conditions, we have the following useful identity [15]

$$\|\boldsymbol{\omega}(t)\|_{L^{2}(\Omega)} = \int_{\Omega} |\boldsymbol{\omega}(\mathbf{x}, t)|^{2} d\mathbf{x}$$

$$= \int_{\Omega} (\nabla_{\mathbf{x}} \times \mathbf{u}(\mathbf{x}, t)) \cdot (\nabla_{\mathbf{x}} \times \mathbf{u}(\mathbf{x}, t)) d\mathbf{x}$$

$$= \int_{\Omega} [\nabla_{\mathbf{x}} \times (\nabla_{\mathbf{x}} \times \mathbf{u}(\mathbf{x}, t))] \cdot \mathbf{u}(\mathbf{x}, t) d\mathbf{x} \qquad \text{(integration by parts)}$$

$$= \int_{\Omega} [\nabla_{\mathbf{x}} (\nabla_{\mathbf{x}} \cdot \mathbf{u}(\mathbf{x}, t)) - \Delta \mathbf{u}(\mathbf{x}, t)] \cdot \mathbf{u}(\mathbf{x}, t) d\mathbf{x} \qquad \text{(double cross-product identity)}$$

$$= \int_{\Omega} -\Delta \mathbf{u}(\mathbf{x}, t) \cdot \mathbf{u}(\mathbf{x}, t) d\mathbf{x} \qquad \text{(divergence-free condition)}$$

$$= \int_{\Omega} |\nabla_{\mathbf{x}} \mathbf{u}(\mathbf{x}, t)|^{2} d\mathbf{x} \qquad \text{(integration by parts)}$$

$$= \|\nabla_{\mathbf{x}} \mathbf{u}(t)\|_{L^{2}(\Omega)},$$

<sup>&</sup>lt;sup>1</sup>The enstrophy is often defined without the factor of 1/2. However, for consistency with earlier studies belonging to this research program [5, 6, 7, 8, 58, 29], we choose to retain this factor here.

where all the boundary terms resulting from integration by parts vanish due to the boundary conditions on  $\mathbf{u}(\mathbf{x},t)$ . Then, we can also compute the enstrophy as

$$\mathcal{E}(\mathbf{u}(t)) = \frac{1}{2} \| \mathbf{\nabla}_{\mathbf{x}} \, \mathbf{u}(t) \|_{L^{2}(\Omega)} = \frac{1}{2} \| \mathbf{u}(t) \|_{\dot{H}^{1}(\Omega)}. \tag{2.8}$$

For simplicity, when there is no risk of confusion, we will denote  $\mathcal{E}(t) = \mathcal{E}(\mathbf{u}(t))$ .

**Definition 2.6** (Kinetic energy). The kinetic energy of a time-dependent flow  $\mathbf{u}(t)$  is defined as

$$\mathcal{K}(\mathbf{u}(t)) := \frac{1}{2} \int_{\Omega} |\mathbf{u}(\mathbf{x}, t)|^2 d\mathbf{x} = \frac{1}{2} ||\mathbf{u}(t)||_{L^2(\Omega)}^2.$$
(2.9)

At t = 0, we write  $\mathcal{K}_0 := \mathcal{K}(\mathbf{u}(0))$  and  $\mathcal{E}_0 := \mathcal{E}(\mathbf{u}(0))$ .

**Definition 2.7** (Dual Space). Let X be a Banach space. The dual space of X,  $X^*$ , is the space of all continuous linear functionals from X to  $\mathbb{R}$ .

In the case of the Lebesgue spaces,  $L^q(\Omega)$ , we have that  $(L^q(\Omega))^*$  is isometrically isomorphic to the space  $L^p(\Omega)$ , where  $\frac{1}{q} + \frac{1}{p} = 1$ . Additionally, we use the notation

$$\langle f, g \rangle_{(L^q(\Omega))^* \times L^q(\Omega)} = \langle f, g \rangle_{L^p(\Omega) \times L^q(\Omega)} := \int_{\Omega} f(\mathbf{x}) g(\mathbf{x}) d\mathbf{x}$$
 (2.10)

to denote the duality pairing between the elements  $f \in L^p(\Omega)$  and  $g \in L^q(\Omega)$ .

### 2.2 Some Key Results

In this section we state some well-known results that we use throughout this thesis [2, 12, 17, 51].

**Theorem 2.1** (Sobolev embedding). Let  $\Omega \subset \mathbb{R}^3$  be any smooth bounded domain or  $\Omega = \mathbb{R}^3$  or  $\Omega = \mathbb{T}^3$ . If  $0 \le s < 3/2$ , then

$$H^s(\Omega) \hookrightarrow L^{6/(3-2s)}(\Omega),$$
 (2.11)

i.e., the identity mapping  $i: H^s(\Omega) \to L^{6/(3-2s)}(\Omega)$  is a continuous operator, meaning that there exists a constant C, which depends only on  $\Omega$ , such that

$$\|\mathbf{u}\|_{L^{6/(3-2s)}(\Omega)} \leq C\|\mathbf{u}\|_{H^s(\Omega)}, \quad \text{for all} \quad \mathbf{u} \in H^s(\Omega).$$

**Lemma 2.1** (Grönwall). Let  $\eta:[0,T]\to[0,\infty)$  be an absolutely continuous function that satisfies the differential inequality

$$\eta'(t) \le \phi(t)\eta(t) + \psi(t),\tag{2.12}$$

where  $\phi$  and  $\psi$  are non-negative integrable functions. Then

$$\eta(t) \le e^{\int_0^t \phi(\tau) d\tau} \left[ \eta(0) + \int_0^t \psi(\tau) d\tau \right] \quad \text{for all } t \in [0, T].$$
(2.13)

**Theorem 2.2** (Hölder's inequality). Let  $\Omega$  be a measurable set in  $\mathbb{R}^n$ , either bounded or unbounded. If  $f \in L^p(\Omega)$  and  $g \in L^q(\Omega)$ , where

$$\frac{1}{p} + \frac{1}{q} = 1, \quad 1 \le p, \ q \le \infty,$$

then  $fg \in L^1(\Omega)$  and

$$\int_{\Omega} |f(\mathbf{x})g(\mathbf{x})| \, d\mathbf{x} \le ||f||_{L^{p}(\Omega)} ||g||_{L^{q}(\Omega)}. \tag{2.14}$$

**Theorem 2.3** (Riesz representation). Let H be a Hilbert space with an inner product  $\langle \cdot, \cdot \rangle_H$ . Given any continuous linear map  $\varphi : H \to \mathbb{R}$ , there exists a unique  $f \in H$  such that

$$\varphi(g) = \langle f, g \rangle_H \quad \forall g \in H. \tag{2.15}$$

## 2.3 Conditional Regularity Results

It is common to find conditions on quantities defined on solutions of the Navier–Stokes system that will guarantee the smoothness of these solutions. While we do not know whether these conditions are true, if they are satisfied for a given solution  $\mathbf{u}$ , they guarantee that  $\mathbf{u}$  is smooth and satisfies the Navier-Stokes system in the classical sense. Here we will mention some of the best results of this type.

#### 2.3.1 The Enstrophy Condition

The first result we will state is based on the enstrophy of the time-dependent velocity field  $\mathbf{u}(t)$  [20, 51].

**Theorem 2.4** (Foias & Temam (1989)). Assume that there exist a Leray-Hopf weak solution  $\mathbf{u}(t)$  of the Navier-Stokes system (1.1) on [0,T]. Then,

$$\sup_{0 \le t \le T} \mathcal{E}(\mathbf{u}(t)) < \infty \tag{2.16}$$

holds up to a certain time T > 0, if and only if  $\mathbf{u}(t)$  satisfies the Navier-Stokes system in the classical sense on [0, T).

Foias & Temam (1989) presented the previous theorem as an implication; i.e., the boundedness of the enstrophy implies that the solution is classical. However, the reverse is also true since classical solutions of (1.1) are actually analytic functions on (0,T] [51]. This means that their Fourier coefficients decay to zero exponentially fast, which in turns implies that the enstrophy is a bounded function.

Theorem 2.4 then implies that if a singularity is formed in a classical solution  $\mathbf{u}(t)$  of the Navier-Stokes system (1.1), there exists a time  $0 < T^* < \infty$  where

$$\lim_{t \to T^{*^-}} \mathcal{E}(\mathbf{u}(t)) = \infty. \tag{2.17}$$

Although it is not known whether relation (2.16) holds for all smooth initial data and arbitrary large time windows, Leray-Hopf weak solutions (1.3) satisfy

$$\int_0^T \mathcal{E}(\mathbf{u}(t)) dt < \infty,$$

for all times T (see expression (2.22)).

A priori upper bounds on the rates of growth of quantities of interest, such as the enstrophy, typically have the general form

$$\frac{d\mathcal{E}}{dt} < C\mathcal{E}^{\alpha}, \quad \alpha > 1, \text{ and } C > 0.$$
 (2.18)

Hereafter, C will denote a generic positive constant whose numerical value may be different from instance to instance. Under the assumption that system (1.1) admits a classical solution on [0, T], Lu & Doering [34] found a sharp bound for the instantaneous rate of change of the enstrophy

$$\frac{d\mathcal{E}}{dt} \le \frac{27}{8\pi^4 \nu^3} \mathcal{E}^3. \tag{2.19}$$

By integrating both sides in time, it yields

$$\mathcal{E}(\mathbf{u}(t)) \le \frac{\mathcal{E}_0}{\sqrt{1 - \frac{27}{4\pi^4 \nu^3} \mathcal{E}_0^2 t}},\tag{2.20}$$

which provides an a priori bound on the enstrophy valid only up to the time  $t^* = 4\pi^4/(27\mathcal{E}_0^2)$ . Global bounds on the enstrophy and  $\int_0^T \mathcal{E}^2(\mathbf{u}(t)) dt$  remain as open problems. However, when  $1 < \alpha \le 2$  in (2.18), it is possible to prove that the enstrophy is bounded for all times. To do that, we need a relation between the kinetic energy and the enstrophy valid for the classical solutions of the 3D Navier-Stokes system (1.1), which is obtained as

$$\begin{split} \frac{d\mathcal{K}}{dt} &= \frac{1}{2} \frac{d}{dt} \int_{\Omega} |\mathbf{u}|^2 d\mathbf{x} \\ &= \int_{\Omega} \mathbf{u} \cdot \partial_t \mathbf{u} d\mathbf{x} \\ &= \int_{\Omega} \mathbf{u} \cdot (-(\mathbf{u} \cdot \nabla_{\mathbf{x}}) \mathbf{u} - \nabla_{\mathbf{x}} p + \nu \Delta \mathbf{u}) d\mathbf{x} \\ &= -\int_{\Omega} \mathbf{u} \cdot [(\mathbf{u} \cdot \nabla_{\mathbf{x}}) \mathbf{u}] d\mathbf{x} - \int_{\Omega} \mathbf{u} \cdot \nabla_{\mathbf{x}} p d\mathbf{x} + \nu \int_{\Omega} \mathbf{u} \cdot \Delta \mathbf{u} d\mathbf{x}, \end{split}$$

where

$$\int_{\Omega} \mathbf{u} \cdot [(\mathbf{u} \cdot \nabla_{\mathbf{x}}) \, \mathbf{u}] \, d\mathbf{x} = \int_{\Omega} u_i \, u_j \partial_j u_i \, d\mathbf{x}$$
 (Einstein's summation convention)
$$= -\int_{\Omega} u_i \partial_j (u_i \, u_j) \, d\mathbf{x}$$
 (integration by parts)
$$= -\int_{\Omega} u_i \, u_j \partial_j u_i \, d\mathbf{x} - \int_{\Omega} u_i^2 \partial_j u_j \, d\mathbf{x}$$
 (product rule)
$$= -\int_{\Omega} u_i \, u_j \partial_j u_i \, d\mathbf{x} - \int_{\Omega} u_i^2 \, \nabla_{\mathbf{x}} \cdot \mathbf{u} \, d\mathbf{x}$$

$$= -\int_{\Omega} u_i \, u_j \partial_j u_i \, d\mathbf{x}$$
 (divergence-free vector field)
$$= -\int_{\Omega} \mathbf{u} \cdot [(\mathbf{u} \cdot \nabla_{\mathbf{x}}) \, \mathbf{u}] \, d\mathbf{x},$$

so then

$$\int_{\Omega} \mathbf{u} \cdot [(\mathbf{u} \cdot \nabla_{\mathbf{x}}) \, \mathbf{u}] \, d\mathbf{x} = 0,$$

and

$$\int_{\Omega} \mathbf{u} \cdot \nabla_{\mathbf{x}} p = \int_{\Omega} (\nabla_{\mathbf{x}} \cdot \mathbf{u}) p \, d\mathbf{x} \qquad \text{(integration by parts)}$$
$$=0,$$

and

$$\nu \int_{\Omega} \mathbf{u} \cdot \Delta \mathbf{u} \, d\mathbf{x} = -\nu \int_{\Omega} |\nabla_{\mathbf{x}} \mathbf{u}| \, d\mathbf{x} \qquad \text{(integration by parts)}$$
$$= -2\nu \mathcal{E},$$

where all the boundary terms that appear after integrating by parts vanish due to the periodic boundary conditions on  $\mathbf{u}(\mathbf{x},t)$ . Therefore, we finally have

$$\frac{d\mathcal{K}}{dt} = -2\nu\mathcal{E}.\tag{2.21}$$

By integrating both sides with respect to time we obtain

$$\int_0^t \mathcal{E}(s) \, ds = \frac{1}{2\nu} \left[ \mathcal{K}_0 - \mathcal{K}(\mathbf{u}(t)) \right] \le \frac{1}{2\nu} \mathcal{K}_0. \tag{2.22}$$

For  $1 < \alpha \le 2$ , we can bound expression (2.18) as

$$\frac{d\mathcal{E}}{dt} \le C\mathcal{E}^{\alpha} \le C\mathcal{E}^{2}. \tag{2.23}$$

Applying Grönwall's Lemma 2.1 to (2.23), we provide a bound for the enstrophy valid for all times when  $1 < \alpha \le 2$ ,

$$\mathcal{E}(t) \le \mathcal{E}_0 \exp\left[\frac{\mathcal{K}_0}{2\nu}\right].$$
 (2.24)

Relations (2.18), (2.19) and (2.24) suggest that for a blow-up to occur the rate of change of the enstrophy must be sustained at a level proportional to  $\mathcal{E}^{\alpha}$  with  $2 < \alpha \leq 3$  for a sufficiently long period of time.

Additionally, global existence of smooth solutions of (1.1) is known for "small" initial data  $\mathbf{u}_0$  [34, 8]. Observe that we can manipulate expression (2.19) in the following way,

$$\frac{d\mathcal{E}}{dt} \leq \frac{27}{8\pi^4 \nu^3} \mathcal{E}^3,$$

$$\frac{1}{\mathcal{E}^2} \frac{d\mathcal{E}}{dt} \leq \frac{27}{8\pi^4 \nu^3} \mathcal{E},$$

$$\int_{\mathcal{E}_0}^{\mathcal{E}(t)} \frac{1}{\mathcal{E}^2} d\mathcal{E} \leq \frac{27}{8\pi^4 \nu^3} \int_0^t \mathcal{E}(s) \, ds.$$

Now, using (2.22), we get

$$\frac{1}{\mathcal{E}_0} - \frac{1}{\mathcal{E}(t)} \le \frac{27}{(2\pi)^4 \nu^3} \mathcal{K}_0.$$

So then, we can bound  $\max_{t\geq 0} \mathcal{E}(t)$  as

$$\max_{t \ge 0} \mathcal{E}(t) \le \frac{(2\pi)^4 \nu^3 \mathcal{E}_0}{(2\pi)^4 \nu^3 - 27 \mathcal{E}_0 \mathcal{K}_0}.$$
 (2.25)

Inequality (2.25) implies that a uniform bound for the enstrophy is obtained if the initial data satisfy the inequality

$$\mathcal{E}_0 \mathcal{K}_0 \le \frac{(2\pi)^4 \nu^3}{27}.\tag{2.26}$$

Therefore, by the enstrophy condition (2.16), if inequality (2.26) holds, we have global classical solutions.

#### 2.3.2 Ladyzhenskaya-Prodi-Serrin Conditions

Another well-known conditional regularity result is given by the family of the Ladyzhenskaya-Prodi-Serrin (LPS) conditions [31, 45, 52].

**Theorem 2.5.** Let  $\mathbf{u}(t)$  be a weak solution of the Navier-Stokes equations (1.1). Then

$$\mathbf{u} \in L^p([0,T]; L^q(\Omega)), \quad 2/p + 3/q = 1, \quad q > 3.$$
 (2.27)

i.e.

$$\left(\int_0^T \|\mathbf{u}(t)\|_{L^q(\Omega)}^p dt\right)^{\frac{1}{p}} < \infty, \tag{2.28}$$

if and only if  $\mathbf{u}(t)$  is a smooth classical solution of (1.1).

It is worth mentioning that this condition also holds for  $2/p + 3/q \le 1$ , but here we will be focusing only on the borderline case corresponding to the equality. As regards the limiting case with q = 3, the corresponding condition was established in [16] as

$$\mathbf{u} \in L^{\infty}([0,T]; L^{3}(\Omega)) \tag{2.29}$$

and a related blow-up criterion was recently obtained in [54]. Condition (2.27) implies that if a singularity is formed in a classical solution  $\mathbf{u}(t)$  of the Navier-Stokes system (1.1) at a time  $T^* \in (0, \infty)$ , then necessarily

$$\lim_{t \to T^*} \int_0^t \|\mathbf{u}(\tau)\|_{L^q(\Omega)}^p d\tau = \infty, \quad 2/p + 3/q = 1, \quad q > 3.$$
 (2.30)

In a recent study, Kang & Protas examined the LPS condition for q = 4 and p = 8 [28]. They proposed an optimization formulation to search for initial data that could potentially lead to the behavior given in (2.30). However, they did not find any evidence for blowup.

## 2.4 A Priori Bounds for $\frac{d}{dt} \|\mathbf{u}(t)\|_{L^q(\Omega)}$

A well-known upper bound for the rate of growth of the  $L^q$  norm is given by Robinson & Sadowski in [50]

$$\frac{d}{dt} \|\mathbf{u}(t)\|_{L^{q}(\Omega)} \le C \|\mathbf{u}(t)\|_{L^{q}(\Omega)}^{\frac{3(q-1)}{q-3}} = C \|\mathbf{u}(t)\|_{L^{q}(\Omega)}^{p+1}, \quad q > 3,$$
(2.31)

where C is a positive constant that might depend on q and 2/p+3/q=1. Its derivation can be found in Appendix A.

By simply integrating in time inequality (2.31), we get

$$\|\mathbf{u}(t)\|_{L^{q}(\Omega)} \le \frac{1}{\left(\|\mathbf{u}_{0}\|_{L^{q}(\Omega)}^{-p} - p C t\right)^{1/p}}.$$
 (2.32)

Hence, we cannot guarantee boundedness of the  $L^q(\Omega)$  norm beyond the time

$$\bar{t} := \frac{1}{p \, C \, \|\mathbf{u}_0\|_{L^q(\Omega)}^p}.\tag{2.33}$$

As regards the limiting case q = 3, it is known that [51].

$$\frac{1}{3}\frac{d}{dt}\|\mathbf{u}(t)\|_{L^{3}(\Omega)}^{3} \le C\|\mathbf{u}(t)\|_{L^{3}(\Omega)}^{2}\|\mathbf{u}(t)\|_{L^{9}(\Omega)}^{3},$$

which implies that

$$\frac{d}{dt} \|\mathbf{u}(t)\|_{L^{3}(\Omega)} \leq C \|\mathbf{u}(t)\|_{L^{9}(\Omega)}^{3} 
\leq C \|\mathbf{u}(t)\|_{L^{3}(\Omega)} \|\mathbf{u}(t)\|_{L^{\infty}(\Omega)}^{2} \quad \text{(by H\"older's inequality (2.14))}.$$

However, this inequality is not in the form of  $\frac{d}{dt}Y \leq CY^{\alpha}$ , which is the type of relation we are interested in. It is also known that the integral of the solution norm  $||\mathbf{u}(t)||_{L^{q}(\Omega)}$  raised to a certain power smaller than in (2.28) on the time interval [0,T] is a bounded quantity for Leray-Hopf weak solutions [50]. In this context, Kang & Protas [28] stated the bounds explicitly,

$$\int_{0}^{T} \|\mathbf{u}(t)\|_{L^{q}(\Omega)}^{\frac{4q}{3(q-2)}} dt \le C \mathcal{K}_{0}^{\frac{2q}{3(q-2)}}, \quad 2 \le q \le 6, \tag{2.35}$$

and

$$\int_{0}^{T} \|\mathbf{u}(t)\|_{L^{q}(\Omega)}^{\frac{q}{q-3}} dt \le C\mathcal{K}_{0}^{3}, \quad q > 6.$$
 (2.36)

These bounds allow us to determine a growth rate of the solution norm in the space  $L^q(\Omega)$  ensuring that there is no blow-up in finite time:

$$\frac{d}{dt} \|\mathbf{u}(t)\|_{L^{q}(\Omega)} \leq \begin{cases}
C \|\mathbf{u}(t)\|_{L^{q}(\Omega)}^{\frac{7q-6}{3(q-2)}} & 2 \leq q \leq 6, \\
C \|\mathbf{u}(t)\|_{L^{q}(\Omega)}^{\frac{2q-3}{q-3}} & q > 6.
\end{cases}$$
(2.37)

To show this, let us first consider the case with  $2 \le q \le 6$ . So then

$$\frac{d}{dt}\|\mathbf{u}(t)\|_{L^q(\Omega)} \leq C\|\mathbf{u}(t)\|_{L^q(\Omega)}^{\frac{7q-6}{3(q-2)}} = C\|\mathbf{u}(t)\|_{L^q(\Omega)}\|\mathbf{u}(t)\|_{L^q(\Omega)}^{\frac{4q}{3(q-2)}}.$$

By Grönwall's lemma 2.1 and estimate (2.35), we can bound the  $L^q(\Omega)$  norm of the solution on any interval [0, T], T > 0, by

$$\|\mathbf{u}(t)\|_{L^{q}(\Omega)} \leq \|\mathbf{u}_{0}\|_{L^{q}(\Omega)} \exp\left(C \int_{0}^{T} \|\mathbf{u}(t)\|_{L^{q}(\Omega)}^{\frac{4q}{3(q-2)}} dt\right)$$
$$\leq \|\mathbf{u}_{0}\|_{L^{q}(\Omega)} \exp\left(C \mathcal{K}_{0}^{\frac{2q}{3(q-2)}}\right) < \infty.$$

Similarly, for q > 6, we have

$$\frac{d}{dt} \|\mathbf{u}(t)\|_{L^{q}(\Omega)} \le C \|\mathbf{u}(t)\|_{L^{q}(\Omega)}^{\frac{2q-3}{q-3}} = C \|\mathbf{u}(t)\|_{L^{q}(\Omega)} \|\mathbf{u}(t)\|_{L^{q}(\Omega)}^{\frac{q}{q-3}}.$$

Again, by Grönwall's lemma 2.1, we can obtain a bound on the  $L^q(\Omega)$  norm of the solution on any interval [0,T]

$$\|\mathbf{u}(t)\|_{L^{q}(\Omega)} \leq \|\mathbf{u}_{0}\|_{L^{q}(\Omega)} \exp\left(C \int_{0}^{T} \|\mathbf{u}(t)\|_{L^{q}(\Omega)}^{\frac{q}{q-3}} dt\right)$$
$$\leq \|\mathbf{u}_{0}\|_{L^{q}(\Omega)} \exp\left(C \mathcal{K}_{0}^{3}\right) < \infty.$$

Additionally, assuming that there is a finite-time blow-up of the solution to the Navier-Stokes system (1.1) at  $t = T^*$ , it is commonly supposed that  $\|\mathbf{u}(t)\|_{L^q(\Omega)} = \frac{C}{(T^*-t)^{\alpha}}$ ,

 $\alpha > 0$ . Plugging this ansatz in expression (2.30), we then have that  $\alpha p \geq 1$ , and

$$\frac{d}{dt} \|\mathbf{u}(t)\|_{L^{q}(\Omega)} = \frac{C}{(T^* - t)^{1+\alpha}}$$
$$= C \left[ \frac{1}{(T^* - t)^{\alpha}} \right]^{\frac{1+\alpha}{\alpha}}$$
$$= C \|\mathbf{u}(t)\|_{L^{q}(\Omega)}^{\beta},$$

where

$$\beta = \frac{1}{\alpha} + 1 \le p + 1 = \frac{3(q-1)}{q-3}.$$

We therefore conclude that, somewhat counter-intuitively, for a blow-up to occur in Navier-Stokes flows,  $\frac{d}{dt} \|\mathbf{u}(t)\|_{L^q(\Omega)}$  cannot be arbitrarily large. In fact, it must be at most proportional to  $\|\mathbf{u}(t)\|_{L^q(\Omega)}^{3(q-1)/(q-3)}$  as otherwise the integrand expression in (2.30) would blow-up before the integral becomes unbounded. These results are summarized and illustrated in Figure 2.1. Due to inequality (2.31), the rate of growth of the  $L^q(\Omega)$ norm of Navier-Stokes flows cannot be sustained over a long time at a level proportional to the norm itself raised to a power given by the solid line in the figure. Additionally, if the sustained rate of growth of the norm of Navier-Stokes flows is not larger than the values given by dashed lines, which correspond to inequalities (2.37), the  $L^q(\Omega)$  norm will remain bounded for arbitrary times T and blow-up cannot occur. Therefore, to trigger a singularity, the rate of change of the  $L^q(\Omega)$  norm of the Navier-Stokes flows must fall between the values given by the solid and dashed lines. Additionally those rates must be sustained over a sufficient long time which tends to infinity as the growth rate is reduced to the rates given in (2.37). The constant prefactors in inequalities (2.31) and (2.37) are irrelevant in this analysis since we are interested in understanding how fast the  $L^q(\Omega)$  norm of extremal Navier-Stokes flows may grow over time windows [0,T]. These results will be used to inspect how "close" the extreme flows obtained by solving the optimization problems in Section 5 come to producing a singularity.

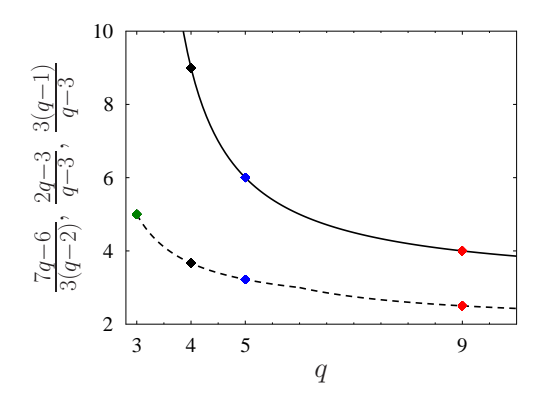


Figure 2.1: Dependence of the exponents in the upper bounds in inequalities (2.31) (solid line) and (2.37) (dashed line) on q.

#### 2.4.1 Gibbon's Conditions

A more comprehensive family of conditional regularity results which generalizes both the enstrophy (2.16) and LPS conditions (2.28) was introduced in [22].

**Theorem 2.6** (Gibbon (2018)). For  $1 \le m \le \infty$  when  $n \ge 1$  and  $3/2 \le m \le \infty$  when n = 0, if a Leray-Hopf weak solution  $\mathbf{u}(\mathbf{x}, t)$  of the 3D Navier-Stokes system (1.1) obeys the following condition, for arbitrary large values of T > 0,

$$\frac{1}{T} \int_0^T \|\mathbf{\nabla}_{\mathbf{x}}^n \mathbf{u}\|_{L^{2m}}^{2\alpha_{n,m}} dt < \infty, \tag{2.38}$$

where

$$\alpha_{n,m} := \frac{2m}{2m(n+1)-3},$$

then  $\mathbf{u}$  is a strong (classical) solution of the 3D Navier-Stokes system on [0,T].

We can regard Theorem 2.6 as a generalization of the LPS conditions (2.27)-(2.28), in the sense that we can recover the latter as a special case by taking 2m = q and n = 0.

## 2.5 Properties of Weak Solutions

In this section we present a series of well-known results concerning properties of the Leray-Hopf weak solutions related to the possible blow-up and eventual regularity of the associated classical solution(s). Under the assumption that singularities exist, Lemma 2.2 asserts the compactness of the set of all possible singularity times  $T^*$  of a Leray-Hopf weak solution  $\mathbf{u}(\mathbf{x},t)$ , i.e., those times at which a Leray-Hopf weak solution is not a classical solution [51].

**Lemma 2.2.** The set  $\Upsilon$  of singular times  $T^*$  of a Leray-Hopf weak solution  $\mathbf{u}(\mathbf{x},t)$  is compact.

Additionally, Theorem 2.7 reveals a remarkable result. We now know that any Leray-Hopf weak solution eventually becomes smooth.

**Theorem 2.7.** Any global-in-time Leray-Hopf weak solution  $\mathbf{u}(\mathbf{x},t)$  of (1.1) is eventually a strong solution.

The proofs of Lemma 2.2 and Theorem 2.7 can be found in [51]. Furthermore, expression (2.25) shows that a singularity cannot form too early, and it is also known that if a singularity has not formed before certain time, the solution will not blow up [42]. This creates a time window where the smoothness of solutions of the Navier-Stokes (1.1) is uncertain. Figure 2.2 schematically summarizes the results mentioned in this section.

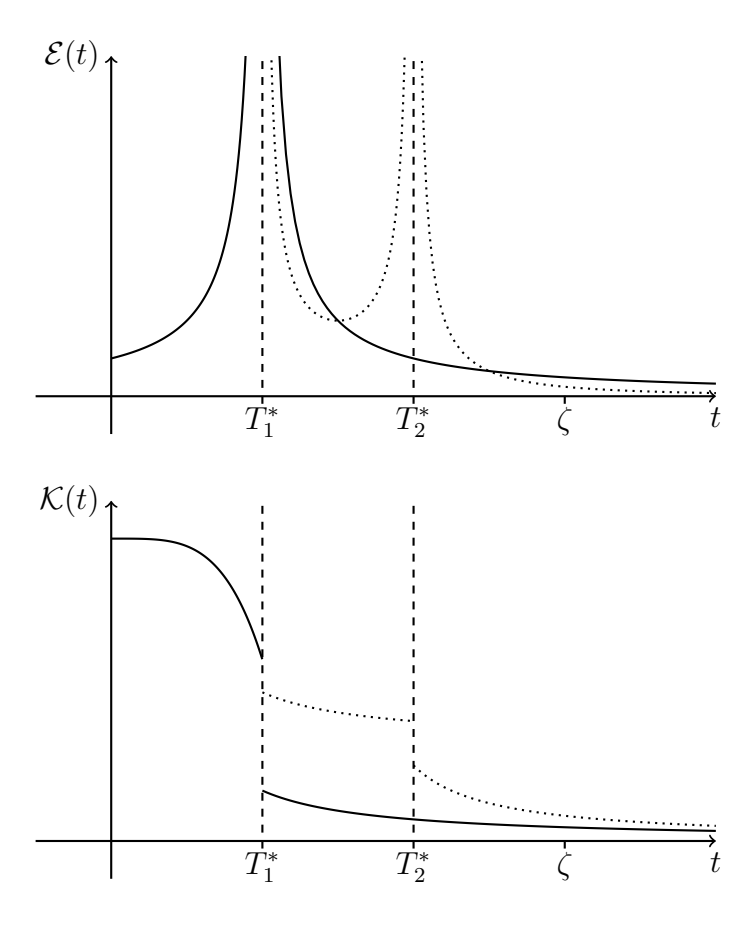


Figure 2.2: (Top) Hypothetical time evolution of the enstrophy, where a singularity occurs at  $t = T_1^*$ . After that, uniqueness can no longer be guaranteed and several solutions may emerge. Some of the new solutions might remain smooth while other might blow up again at  $t = T_2^*$ . However, there exits a time  $\zeta$  after which every Leray-Hopf weak solution becomes a strong solution. (Bottom) The corresponding evolution of the kinematic energy of the solutions presented in the top figure.

# Chapter 3

# **Optimization Formulations**

In this chapter we will formulate a number of optimization problems we will consider in this study. These problems are motivated by the conditional regularity results studied in Chapter 2 and aim at finding optimal initial conditions  $\mathbf{u}_0$  that will produce "extreme" flows, in the sense of maximizing the different regularity indicators involved in the conditional regularity results. The goal is to see whether a singularity might occur in such flows. With the domain  $\Omega$  and the viscosity  $\nu$  fixed, each problem is defined by three parameters, namely, the function space where the initial data is sought, the size of the optimal initial data and the length of the time window.

## 3.1 Motivation

This work is motivated by the study conducted by Kang & Protas in [28]. They investigated the following objective functional with q = 4,

$$\Phi_T^q(\mathbf{u}_0) := \frac{1}{T} \int_0^T \|\mathbf{u}(\tau)\|_{L^q(\Omega)}^{\frac{2q}{q-3}} d\tau, \tag{3.1}$$

and numerically found local maximizers of Problem 0 defined below for a range of parameter values. Note that expression (3.1) coincides with the integral expression (2.28) from the family of the LPS conditions in Theorem 2.5, except for the prefactor

 $T^{-1}$  which ensures expression (3.1) remains bounded even if the integral grows without bound when T tends to infinity.

**Problem 0.** Given  $B, T \in \mathbb{R}_+ := (0, \infty)$ , and the objective functional  $\Phi_T^4(\mathbf{u}_0)$  from equation (3.1), find

$$\widetilde{\mathbf{u}}_{0;B,T} = \underset{\mathbf{u}_0 \in \mathcal{M}_B}{\arg\max} \ \Phi_T^4(\mathbf{u}_0), \quad where$$
(3.2)

$$\mathcal{M}_B := \left\{ \mathbf{u}_0 \in H^{3/4}(\Omega) : \ \nabla_{\mathbf{x}} \cdot \mathbf{u}_0 = 0, \ \int_{\Omega} \mathbf{u}_0 \, d\mathbf{x} = 0, \ \|\mathbf{u}_0\|_{L^4(\Omega)} = B \right\}. \tag{3.3}$$

The space  $H^{3/4}(\Omega)$  is the largest Hilbert-Sobolev space embedded in the Lebesgue space  $L^4(\Omega)$ . In this thesis, we will extend this optimization formulation to other Lebesgue spaces  $L^q(\Omega)$  with  $q \geq 3$ . An explanation of how to obtain the corresponding Hilbert-Sobolev space  $H^s(\Omega)$  from a given Lebesgue space  $L^q(\Omega)$  is provided in the next section.

## 3.2 Choice of the Lebesgue and Sobolev Spaces

It will be necessary to correctly define the largest Sobolev space embedded in a given Lebesgue space  $L^q(\Omega)$ , so that we can deduce the gradient of the objective functional using standard techniques relying on Theorem 2.3 (Riesz representation). From Theorem 2.1 (Sobolev embedding), we know that

$$H^s(\Omega) \hookrightarrow L^q(\Omega), \quad \text{if} \quad s \ge \frac{3}{2} - \frac{3}{q}.$$
 (3.4)

Therefore, the largest Sobolev space  $H^s(\Omega)$  embedded in the Lebesgue space  $L^q(\Omega)$  is obtained when s = 3/2 - 3/q. Figure 3.1 shows the values of the parameter s corresponding to different values of q. The solid symbols in Figure 3.1(a) represent the values of q that we will consider in this study in addition to the limiting case q = 3. The reason behind these choices is that those are the only cases where p and q are simultaneously integers, which will facilitate interpretation of the results. The symbols in Figure 3.1(b) represent the corresponding values of s that make the space  $H^s(\Omega)$  the largest Sobolev space embedded in the Lebesgue space  $L^q(\Omega)$ .

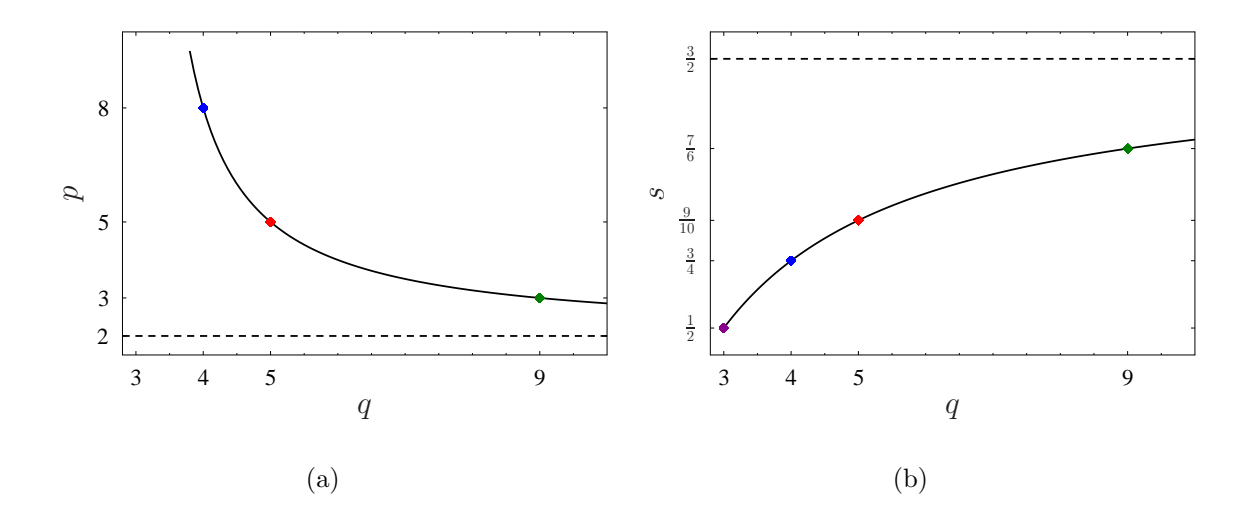


Figure 3.1: (a) The black solid line represents all the possible choices of p and q for which the LPS condition (2.27) holds. The solid symbols represent the situations where p and q are both integer numbers. Additionally, the limiting case q=3 will also be considered. The dashed line is the horizontal asymptote given by expression (2.27). (b) The black solid line represents the index of the largest Sobolev space  $H^s(\Omega)$  embedded in the Lebesgue space  $L^q(\Omega)$  for a given value of q. The solid symbols represent the cases that are analyzed in detail in this study. The dashed line represents the limiting value of expression (3.4) when q tends to infinity.

## 3.3 Optimization Problems

A natural extension of Problem 0 to any Lebesgue space  $L^q(\Omega)$  with q>3 is

**Problem 1.** Given  $B, T \in \mathbb{R}_+$ , q > 3, s = 3/2 - 3/q and the objective functional  $\Phi_T^q(\mathbf{u}_0)$  from equation (3.1), find

$$\widetilde{\mathbf{u}}_{0;B,T} = \underset{\mathbf{u}_0 \in \mathcal{M}_B}{\arg\max} \ \Phi_T^q(\mathbf{u}_0), \quad where$$
(3.5)

$$\mathcal{M}_B := \left\{ \mathbf{u}_0 \in H^s(\Omega) : \; \mathbf{\nabla}_{\mathbf{x}} \cdot \mathbf{u}_0 = 0, \; \int_{\Omega} \mathbf{u}_0 \, d\mathbf{x} = 0, \; \|\mathbf{u}_0\|_{L^q(\Omega)} = B \right\}. \tag{3.6}$$

The space  $H^s(\Omega)$  with s = 3/2 - 3/q is the largest Hilbert-Sobolev space embedded in

the space  $L^q(\Omega)$  (see Section 3.2). We intentionally denoted the manifold  $\mathcal{M}_B$  with the same symbol as in Problem 0 since they coincide for q=4.

Notice that Problem 1 is defined on the Sobolev space  $H^s(\Omega)$ , which is endowed with an inner product structure, that one can use when constructing a solution to the optimization problem.

To generalize the work of Kang & Protas [28], we will solve a further extension of Problem 1 where the optimal initial condition  $\mathbf{u}_0$  is sought in the Lebesgue space  $L^q(\Omega)$ , rather than in  $H^s(\Omega)$  with  $1/2 \leq s < 3/2$ , and we will do so for different values of q shown in Figure 3.1(a). We will therefore solve the following problem

**Problem 2.** Given  $B, T \in \mathbb{R}_+$ , q > 3 and the objective functional  $\Phi_T^q(\mathbf{u}_0)$  from equation (3.1), find

$$\widetilde{\mathbf{u}}_{0;B,T} = \underset{\mathbf{u}_0 \in \mathcal{L}_B}{\arg\max} \ \Phi_T^q(\mathbf{u}_0), \quad where$$
(3.7)

$$\mathcal{L}_B := \left\{ \mathbf{u}_0 \in L^q(\Omega) : \, \mathbf{\nabla}_{\mathbf{x}} \cdot \mathbf{u}_0 = 0, \, \int_{\Omega} \mathbf{u}_0 \, d\mathbf{x} = 0, \, \|\mathbf{u}_0\|_{L^q(\Omega)} = B \right\}. \tag{3.8}$$

Notice that this modification of the functional setting makes Problem 2 considerably harder than Problem 1 from a numerical point of view due to the lack of the Hilbert structure in the Lebesgue spaces  $L^q(\Omega)$ , q > 3. In this thesis, we will first consider Problems 1 and 2 for integer values of q equal to 4, 5 and 9 since they also produce integer values in p (see Figure 3.1(a)). Another formulation that we are interested in is the limiting case q = 3. In this case, as was mentioned in Section 2.3.2, in order for the solution to remain smooth, we need to ensure the solution belongs to  $L^{\infty}([0,T];L^3(\Omega))$ , i.e.,

$$\sup_{0 \le t \le T} \|\mathbf{u}(t)\|_{L^3(\Omega)} < \infty.$$

Due to the nondifferentiability of the supremum function involved in the definition of the  $L^{\infty}(\Omega)$  norm, the formulations we consider here are different from Problems 1 and 2. Now, we consider the following objective functional

$$\Psi_T(\mathbf{u}_0) := \|\mathbf{u}(T)\|_{L^3(\Omega)}^3 = \int_{\Omega} |\mathbf{u}(\mathbf{x}, T)|^3 d\mathbf{x}, \quad \text{for some } T > 0,$$
(3.9)

and pose the following two problems.

**Problem 3.** Given  $B, T \in \mathbb{R}_+$  and the objective functional  $\Psi_T(\mathbf{u}_0)$  from equation (3.9), find

$$\widetilde{\mathbf{u}}_{0;B,T} = \underset{\mathbf{u}_0 \in \mathcal{N}_B}{\operatorname{arg\,max}} \ \Psi_T(\mathbf{u}_0), \quad where$$
(3.10)

$$\mathcal{N}_B := \left\{ \mathbf{u}_0 \in H^{1/2}(\Omega) : \, \mathbf{\nabla}_{\mathbf{x}} \cdot \mathbf{u}_0 = 0, \, \int_{\Omega} \mathbf{u}_0 \, d\mathbf{x} = 0, \, \|\mathbf{u}_0\|_{L^3(\Omega)} = B \right\}.$$
 (3.11)

**Problem 4.** Given  $B, T \in \mathbb{R}_+$  and the objective functional  $\Psi_T(\mathbf{u}_0)$  from equation (3.9), find

$$\widetilde{\mathbf{u}}_{0;B,T} = \underset{\mathbf{u}_0 \in \mathcal{S}_B}{\arg \max} \ \Psi_T(\mathbf{u}_0), \quad where$$
(3.12)

$$\mathcal{S}_B := \left\{ \mathbf{u}_0 \in L^3(\Omega) : \, \mathbf{\nabla}_{\mathbf{x}} \cdot \mathbf{u}_0 = 0, \, \int_{\Omega} \mathbf{u}_0 \, d\mathbf{x} = 0, \, \|\mathbf{u}_0\|_{L^3(\Omega)} = B \right\}. \tag{3.13}$$

Problems 3 and 4 are analogous to Problems 1 and 2, but, this time, Problems 3 and 4 are associated with the objective functional (3.9) in the Sobolev and Lebesgue spaces, respectively. An even more general formulation is possible motivated by the regularity condition (2.38) and based on the objective functional

$$\boldsymbol{\varphi}_T^{n,q}(\mathbf{u}_0) := \frac{1}{T} \int_0^T \|\boldsymbol{\nabla}_{\mathbf{x}}^n \mathbf{u}(\tau)\|_{L^q(\Omega)}^{\frac{2q}{q(n+1)-3}} d\tau, \tag{3.14}$$

where  $n, q \ge 1$ . We thus pose our last optimization problem.

**Problem 5.** Given  $B, T \in \mathbb{R}_+$ , and n, q > 1 and the objective functional  $\varphi_T^q(\mathbf{u}_0)$  from equation (3.14), find

$$\widetilde{\mathbf{u}}_{0;B,T} = \underset{\mathbf{u}_0 \in \mathcal{I}_B}{\operatorname{arg \, max}} \, \boldsymbol{\varphi}_T^q(\mathbf{u}_0), \quad \text{where} \\
\mathcal{I}_B := \left\{ \mathbf{u}_0 \in W^{n,q}(\Omega) : \, \boldsymbol{\nabla}_{\mathbf{x}} \cdot \mathbf{u}_0 = 0, \, \int_{\Omega} \mathbf{u}_0 \, d\mathbf{x} = \mathbf{0}, \, \|\boldsymbol{\nabla}_{\mathbf{x}}^n \, \mathbf{u}_0\|_{L^q(\Omega)} = B \right\}.$$

However, no computations are performed based on this problem.

# Chapter 4

# Solution Approach

In this chapter, we will briefly discuss the numerical approach to solve Problems 1, 2, 3, and 4. First, we will explain in detail how to discretize the gradient flow used to solve these problems, followed by an innovative way to compute the gradient in the Sobolev space  $H^s(\Omega)$  and the Lebesgue  $L^q(\Omega)$  space. Finally, we will explain how to solve the adjoint systems that naturally arise in the solution of this type of optimization problem. We will close this chapter by discussing the conjugate Lebesgue gradient method in Hilbert and Banach spaces.

## 4.1 The Steepest Ascent Method

Assume we want to solve the following unconstrained optimization problem

$$\widetilde{u} = \underset{u \in X}{\operatorname{arg\,max}} J(u),$$
(4.1)

where X is a Banach space and  $J: X \to \mathbb{R}$  is an objective functional. The steepest ascent method [41] approximates the optimal state  $\tilde{u}$  as

$$\widetilde{u} = \lim_{n \to \infty} u_n,$$

where the sequence of  $\{u_n\}_{n\in\mathbb{N}}$  is computed as

$$u_{n+1} = u_n + \alpha_n \nabla J(u_n), \quad n = 0, 1, 2, \dots$$
 (4.2)

with  $u_0$  being an initial guess,  $\nabla J(u_n)$  is the gradient of the objective functional J evaluated at the current state  $u_n$ , and  $\alpha_n > 0$  is the length of the step along the direction of the negative gradient. The parameter  $\alpha_n$  is determined as the solution of a line-search problem

$$\alpha_n = \arg\min_{\beta>0} J\left(u_n + \beta \nabla J(u_n)\right), \tag{4.3}$$

which can be solved using standard techniques, such as Brent's method [41]. The idea behind of this approach is that locally optimal solutions of (4.1) are sought along the direction in which J increases, namely  $\nabla J$ .

# 4.2 Riemannian Optimization

We now describe how to solve Problems 1–4 for given values of B and T. We adapted the algorithm used by Kang & Protas in [28] with ideas taken from [46] in regard to how to compute gradients in Lebesgue spaces. This algorithm is an adaptation of the "optimize-then-discretize" approach [24] in which a gradient method is first formulated in the infinite-dimensional (continuous) setting and only then the resulting equations and expressions are discretized for the purpose of numerical solution. A similar approach was used to solve the problem of determining the maximum growth of enstrophy in [29]. This time the motivation came from the enstrophy condition given in Theorem 2.4, and the corresponding 1D problem studied earlier in [5].

Problem 1 is Riemannian in the sense that local maximizers  $\tilde{\mathbf{u}}_{0;B,T}$  belong to a constraint manifold  $\mathcal{M}_B$  [1]. To locally characterize this manifold, we define the tangent space  $\mathcal{T}_{\mathbf{z}}\mathcal{M}_B$  at a point  $\mathbf{z} \in \mathcal{M}_B$ . To do so, the fixed-norm constraint, i.e.,  $\|\mathbf{u}_0\|_{L^q(\Omega)} = B$ , can be expressed in terms of the function  $G_q: H^s(\Omega) \to \mathbb{R}_+$ , where  $G_q:=\|\mathbf{z}\|_{L^q(\Omega)}^q$ 

and  $H^s(\Omega)$  is the largest Hilbert space embedded in  $L^q(\Omega)$ , as discussed in Section 3.2 with the value of s given by Theorem 2.1. Then, the subspace tangent to the manifold  $\mathcal{M}_B$  at  $\mathbf{z}$  and defined in the space  $H^s(\Omega)$  by the relation  $G_q(\mathbf{z}) = B$  is given by

$$\mathcal{T}_{\mathbf{z}}\mathcal{M}_{B} := \left\{ \mathbf{v} \in H^{s}(\Omega) : \nabla_{\mathbf{x}} \cdot \mathbf{v} = 0, \int_{\Omega} \mathbf{v} \, d\mathbf{x} = \mathbf{0}, \left\langle \nabla G_{q}(\mathbf{z}), \mathbf{v} \right\rangle_{H^{s}(\Omega)} = 0 \right\},$$
 (4.4)

where  $\langle \mathbf{f}, \mathbf{g} \rangle_{H^s} := \int_{\Omega} \mathbf{f} \cdot \mathbf{g} \, d\mathbf{x} + \ell^{2s} \int_{\Omega} \Delta^{s/2} \mathbf{f} \cdot \Delta^{s/2} \mathbf{g} \, d\mathbf{x}$  is the inner product in  $H^s(\Omega)$ , with  $\ell > 0$  being an adjustable parameter, and  $\nabla G_q(\mathbf{z})$  being the gradient of the function  $G_q$  at  $\mathbf{z}$ . A local maximizer  $\tilde{\mathbf{u}}_{0;B,T}$  will then be found by constructing a sequence of divergence-free and zero-mean vector fields with a fixed  $L^q(\Omega)$  norm,  $\{\mathbf{u}_{0;B,T}^{(n)}\}_{n\in\mathbb{N}}$ , such that

$$\widetilde{\mathbf{u}}_{0;B,T} = \lim_{n \to \infty} \mathbf{u}_{0;B,T}^{(n)}.$$

This sequence is defined using the following iterative procedure representing a discretization of a gradient flow projected on the manifold  $\mathcal{M}_B$ 

$$\mathbf{u}_{0;B,T}^{(n+1)} = \mathcal{R}_{\mathcal{M}_B} \left( \mathbf{u}_{0;B,T}^{(n)} + \tau_n \, \mathcal{P}_{\mathcal{T}_n \mathcal{M}_B} \mathbf{\nabla}^{H^s} \Phi_T^q \left( \mathbf{u}_{0;B,T}^{(n)} \right) \right),$$

$$\mathbf{u}_{0;B,T}^{(1)} = \mathbf{u}^0.$$

$$(4.5)$$

Here  $\mathbf{u}_{0;B,T}^{(n)}$  is an approximation of the maximizer obtained at the n-th iteration,  $\mathbf{u}^0$  is an initial guess,  $\mathcal{P}_{\mathcal{T}_n \mathcal{M}_B}$ :  $L^q(\Omega) \to \mathcal{T}_n \mathcal{M}_B := \mathcal{T}_{\mathbf{u}_{0;B,T}^{(n)}} \mathcal{M}_B$  is an operator representing projection onto the tangent subspace (4.4) at the nth iteration,  $\tau_n$  is the step size,  $\nabla^{H^s} \Phi_T^q$  is the gradient of the functional  $\Phi_T^q$  in the Sobolev space  $H^s(\Omega)$ , whereas  $\mathcal{R}_{\mathcal{M}_B}$ :  $\mathcal{T}_n \mathcal{M}_B \to \mathcal{M}_B$  is a retraction from the tangent space to the constraint manifold [1]. Precise definitions of  $\mathcal{P}_{\mathcal{T}_n \mathcal{M}_B}$ ,  $\tau_n$  and  $\mathcal{R}_{\mathcal{M}_B}$  will be given in Section 4.5, while the definition of  $\nabla^{H^s} \Phi_T^q$  will be stated in Section 4.3. The approach to solution of Problem 3 is analogous, the only difference being that now one needs to consider the objective functional (3.9), so these steps are omitted.

As regards the discretization of the gradient flow in Problem 2, the setting is quite similar to Problem 1, with the difference that now we will solve the optimization problem in the Banach space  $L^q(\Omega)$ , which lacks Hilbert structure. This time the maximizer  $\tilde{\mathbf{u}}_{0;B,T}$  belongs to a constraint manifold  $\mathcal{L}_B$ . To locally characterize this manifold, we define the tangent space  $\mathcal{T}_{\mathbf{z}}\mathcal{L}_B$  at a point  $\mathbf{z} \in \mathcal{L}_B$ . In a similar way as before, the fixed-norm constraint is expressed in terms of the function  $F_q: L^q(\Omega) \to \mathbb{R}_+, F_q:= \|\mathbf{z}\|_{L^q(\Omega)}^q$  which is now defined on the Lebesgue space  $L^q(\Omega)$ . Then, the subspace tangent to the manifold  $\mathcal{L}_B$  at  $\mathbf{z} \in L^q(\Omega)$  defined by the relation  $F_q(\mathbf{z}) = B$  is given by

$$\mathcal{T}_{\mathbf{z}}\mathcal{L}_{B} := \left\{ \mathbf{v} \in L^{q}(\Omega) : \mathbf{\nabla}_{\mathbf{x}} \cdot \mathbf{v} = 0, \int_{\Omega} \mathbf{v} \, d\mathbf{x} = \mathbf{0}, \langle \mathbf{\nabla} F_{q}(\mathbf{z}), \mathbf{v} \rangle_{(L^{q}(\Omega))^{*} \times L^{q}(\Omega)} = 0 \right\}, (4.6)$$

where  $(L^q(\Omega))^*$  is the dual space of  $L^q(\Omega)$ , which is identified with  $L^p(\Omega)$  with  $\frac{1}{p} + \frac{1}{q} = 1$  [2]. This definition of the tangent space at a point  $\mathbf{z} \in \mathcal{L}_B$  is a natural extension of this concept from a Hilbert space to a general Banach space with the inner product replaced by a duality pairing (2.10). So then, the maximizer  $\tilde{\mathbf{u}}_{0;B,T}$  is found by constructing a sequence of divergence free and zero-mean vector fields with a fixed  $L^q(\Omega)$ -norm,  $\{\mathbf{u}_{0;B,T}^{(n)}\}_{n\in\mathbb{N}}$ , such that

$$\widetilde{\mathbf{u}}_{0;B,T} = \lim_{n \to \infty} \mathbf{u}_{0;B,T}^{(n)},$$

and the iterative procedure representing the discretization of the gradient flow projected on the manifold  $\mathcal{L}_B$  is

$$\mathbf{u}_{0;B,T}^{(n+1)} = \mathcal{R}_{\mathcal{L}_B} \left( \mathbf{u}_{0;B,T}^{(n)} + \tau_n \, \mathcal{P}_{\mathcal{T}_n \mathcal{L}_B} \boldsymbol{\nabla}^{L^q} \Phi_T^q \left( \mathbf{u}_{0;B,T}^{(n)} \right) \right),$$

$$\mathbf{u}_{0;B,T}^{(1)} = \mathbf{u}^0,$$

$$(4.7)$$

where  $\mathbf{u}_{0;B,T}^{(n)}$  is an approximation of the maximizer obtained at the n-th iteration,  $\mathbf{u}^0$  is a initial guess,  $\mathcal{P}_{\mathcal{T}_n\mathcal{L}_B}$ :  $L^q(\Omega) \to \mathcal{T}_n\mathcal{L}_B := \mathcal{T}_{\mathbf{u}_{0;B,T}^{(n)}}\mathcal{L}_B$  is the operator representing projection onto the tangent subspace (4.4) at the nth iteration,  $\tau_n$  is the step size,  $\nabla^{L^q}\Phi_T^q$  is the gradient of the functional  $\Phi_T^q$  in the Lebesgue space  $L^q(\Omega)$  whereas  $\mathcal{R}_{\mathcal{L}_B}$ :  $\mathcal{T}_n\mathcal{L}_B \to \mathcal{L}_B$  is a retraction from the tangent space to the constraint manifold [1]. The approach to solution of Problem 4 is analogous, the only difference being that now one needs to consider the objective functional (3.9), so these steps are also omitted.

### 4.3 Evaluation of the Gradient

A key element of the iterative procedures (4.5) and (4.7) is the evaluation of the gradients  $\nabla^{H^s}\Phi_T^q$  and  $\nabla^{L^q}\Phi_T^q$  of the objective functional  $\Phi_T^q$ , cf. (3.1) with q > 3. The first step in determining these gradients is to find the gradient of (3.1) with respect to the  $L^2$  topology. Then, it will be possible to find the gradient in Hilbert-Sobolev spaces  $H^s$  and other Lebesgue spaces  $L^q$ .

### 4.3.1 Gradient in $L^2$

Let us consider the Gâteaux (directional) differential  $(\Phi_T^q)'(\mathbf{u}_0;\cdot):L^2(\Omega)\to\mathbb{R}$  of the objective functional  $\Phi_T^q$  defined as

$$(\Phi_T^q)'(\mathbf{u}_0; \mathbf{u}_0') := \lim_{\epsilon \to 0} \frac{\Phi_T^q(\mathbf{u}_0 + \epsilon \mathbf{u}_0') - \Phi_T^q}{\epsilon}$$
(4.8)

for some arbitrary perturbation  $\mathbf{u}'_0 \in L^2(\Omega)$ . The gradient,  $\nabla^{L^2}\Phi^q_T$ , can then be extracted from the Gâteaux differential  $(\Phi^q_T)'(\mathbf{u}_0; \mathbf{u}'_0)$  as follows. Note that for a fixed  $\mathbf{u}_0$ ,  $(\Phi^q_T)'(\mathbf{u}_0; \mathbf{u}'_0)$  is a bounded linear functional of the second argument  $\mathbf{u}'_0$ . Then, by Theorem 2.3 (Riesz representation), we can write it as

$$(\Phi_T^q)'(\mathbf{u}_0; \mathbf{u}_0') = \left\langle \mathbf{\nabla}^{L^2} \Phi_T^q, \mathbf{u}_0' \right\rangle_{L^2(\Omega)}.$$
 (4.9)

Given the definition of the objective functional in (3.1), its Gâteaux differential can be expressed as

$$(\Phi_T^q)'(\mathbf{u}_0; \mathbf{u}_0') = \frac{2q}{(q-3)T} \int_0^T \left( \|\mathbf{u}(t)\|_{L^q(\Omega)}^{\frac{q(5-q)}{q-3}} \int_{\Omega} |\mathbf{u}(\mathbf{x}, t)|^{q-2} \mathbf{u}(\mathbf{x}, t) \cdot \mathbf{u}'(\mathbf{x}, t) d\mathbf{x} \right) dt, \tag{4.10}$$

where the perturbation field  $\mathbf{u}' = \mathbf{u}'(\mathbf{x},t)$  is a solution of the Navier-Stokes system

linearized around the trajectory corresponding to the initial data  $\mathbf{u}_0$  [24], i.e.,

$$\mathcal{L}\begin{bmatrix} \mathbf{u}' \\ p' \end{bmatrix} := \begin{bmatrix} \partial_t \mathbf{u}' + \mathbf{u}' \cdot \nabla_{\mathbf{x}} \mathbf{u} + \mathbf{u} \cdot \nabla_{\mathbf{x}} \mathbf{u}' + \nabla_{\mathbf{x}} p' - \nu \Delta \mathbf{u}' \\ \nabla_{\mathbf{x}} \cdot \mathbf{u}' \end{bmatrix} = \begin{bmatrix} \mathbf{0} \\ 0 \end{bmatrix}, \tag{4.11a}$$

$$\mathbf{u}'(0) = \mathbf{u}'_0, \tag{4.11b}$$

which is subject to periodic boundary conditions and where p' is the perturbation to the pressure.

Observe that expression (4.10) for the Gâteaux differential is not in the Riesz form (4.9), because the perturbation  $\mathbf{u}_0'$  of the initial data does not appear in it explicitly as a factor; instead, it appears in the initial condition (4.11b) of the perturbation system. In order to transform the Gâteaux differential to the required Riesz form (4.9), we introduce the *adjoint states*  $\mathbf{u}^*: \Omega \times [0,T] \to \mathbb{R}^3$  and  $p^*: \Omega \times [0,T] \to \mathbb{R}$ , and the following duality-pairing relation

$$\left(\mathcal{L}\begin{bmatrix}\mathbf{u}'\\p'\end{bmatrix},\begin{bmatrix}\mathbf{u}^*\\p^*\end{bmatrix}\right) := \int_0^T \int_{\Omega} \mathcal{L}\begin{bmatrix}\mathbf{u}'\\p'\end{bmatrix} \cdot \begin{bmatrix}\mathbf{u}^*\\p^*\end{bmatrix} d\mathbf{x} dt = \underbrace{\left(\begin{bmatrix}\mathbf{u}'\\p'\end{bmatrix}, \mathcal{L}^*\begin{bmatrix}\mathbf{u}^*\\p^*\end{bmatrix}\right)}_{(4.12)} + \underbrace{\left(\begin{bmatrix}\mathbf{u}'\\p'\end{bmatrix}, \mathbf{u}'(\mathbf{x}, T) \cdot \mathbf{u}^*(\mathbf{x}, T) d\mathbf{x} - \int_{\Omega} \mathbf{u}'(\mathbf{x}, 0) \cdot \mathbf{u}^*(\mathbf{x}, 0) d\mathbf{x} = 0,}_{(4.12)}$$

where "·" in the first integrand expression denotes the Euclidean dot product evaluated at  $(\mathbf{x},t)$ . Performing integration by parts with respect to both space and time allows us to define the following *adjoint system* 

$$\mathcal{L}^* \begin{bmatrix} \mathbf{u}^* \\ p^* \end{bmatrix} := \begin{bmatrix} -\partial_t \mathbf{u}^* - \begin{bmatrix} \nabla_{\mathbf{x}} \mathbf{u}^* + (\nabla_{\mathbf{x}} \mathbf{u}^*)^T \end{bmatrix} \mathbf{u} - \nabla_{\mathbf{x}} p^* - \nu \Delta \mathbf{u}^* \\ -\nabla_{\mathbf{x}} \cdot \mathbf{u}^* \end{bmatrix} = \begin{bmatrix} \mathbf{f} \\ 0 \end{bmatrix}, \quad (4.13a)$$

$$\mathbf{f}(\mathbf{x},t) := \frac{2q}{(q-3)T} \|\mathbf{u}(t)\|_{L^{q}(\Omega)}^{\frac{q(5-q)}{q-3}} |\mathbf{u}(\mathbf{x},t)|^{q-2} \mathbf{u}(\mathbf{x},t), \ \mathbf{x} \in \Omega, \ t \in [0,T],$$
 (4.13b)

$$\mathbf{u}^*(T) = \mathbf{0} \tag{4.13c}$$

which is also subject to periodic boundary conditions. In identity (4.12) all boundary terms that appear as a result of integrating by parts with respect to the space variable

vanish due to the periodic boundary conditions. The term  $\int_{\Omega} \mathbf{u}'(\mathbf{x}, T) \cdot \mathbf{u}^*(\mathbf{x}, T) d\mathbf{x}$  resulting from integration by parts with respect to time vanishes because of the choice of the terminal condition (4.13c), and with the choice of the source term (4.13b), identity (4.12) implies

$$(\Phi_T^q)'(\mathbf{u}_0; \mathbf{u}_0') = \int_{\Omega} \mathbf{u}_0'(\mathbf{x}) \cdot \mathbf{u}^*(\mathbf{x}, 0) \, d\mathbf{x} = \left\langle \mathbf{u}_0', \mathbf{u}^*(0) \right\rangle_{L^2(\Omega)}. \tag{4.14}$$

Therefore, we obtain the  $L^2(\Omega)$  gradient from (4.9) and (4.14) as

$$\mathbf{\nabla}^{L^2} \Phi_T^q = \mathbf{u}^*(0). \tag{4.15}$$

### 4.3.2 Gradient in the Sobolev Space $H^s$

Once the gradient over the Hilbert space  $L^2(\Omega)$  is computed, we can then calculate the gradient over more regular Hilbert spaces, namely, the Sobolev spaces  $H^s(\Omega)$ , s > 0. First, we proceed to identify the Gâteaux differential with the inner product in  $H^s(\Omega)$  in light of Theorem 2.3 (Riesz representation),

$$(\Phi_T^q)'(\mathbf{u}_0; \mathbf{u}_0') = \left\langle \mathbf{\nabla}^{H^s} \Phi_T^q, \mathbf{u}_0' \right\rangle_{H^s(\Omega)}, \tag{4.16}$$

where  $\nabla^{H^s}\Phi_T^q$  is the Riesz representer of the gradient in  $H^s(\Omega)$ . Then, recalling that that perturbations  $\mathbf{u}_0'$  are arbitrary and expressions (4.9) and (4.16) are equivalent, integrating by parts over the periodic domain  $\Omega$  leads us to the following fractional elliptic boundary-value problem [48]

$$\left[\operatorname{Id} - \ell^{2s} \Delta^{s}\right] \boldsymbol{\nabla}^{H^{s}} \Phi_{T}^{q} = \boldsymbol{\nabla}^{L^{2}} \Phi_{T}^{q} \quad \text{in } \Omega, \tag{4.17}$$

subject to periodic boundary conditions. The solution of equation (4.17) is the gradient in  $H^s(\Omega)$  and it can be easily found in Fourier space. More precisely, after taking the Fourier transform, we obtain

$$\left[1 + \ell^{2s} |\boldsymbol{k}|^{s}\right] \left[\widehat{\boldsymbol{\nabla}^{H^{s}} \Phi_{T}^{q}}\right]_{\boldsymbol{k}} = \left[\boldsymbol{\nabla}^{L^{2}} \Phi_{T}^{q}\right]_{\boldsymbol{k}}, \quad \boldsymbol{k} \in \mathbb{Z}^{3} \setminus \boldsymbol{0}, \tag{4.18a}$$

$$\left[\widehat{\boldsymbol{\nabla}^{H^s}\Phi^q_T}\right]_{\mathbf{0}} = \mathbf{0},\tag{4.18b}$$

where  $\left[\hat{\mathbf{f}}\right]_{k} \in \mathbb{C}^{3}$  represents the Fourier coefficients of the vector field  $\mathbf{f}$  with wavenumber k. As discussed by Protas et al. [48, 28], there are important observations to take into account at this stage. First, the gradients in  $H^{s}$  can be understood as a result of a low-pass filtering applied to the  $L^{2}$  gradients where the parameter  $\ell$  acts as the cutoff length scale. Second, the Sobolev gradients obtained with different  $0 < \ell < \infty$  are equivalent in the sense of norm equivalence [9], however, the value of  $\ell$  tends to have a significant effect on the rate of convergence of gradient iterations in the numerical solution of Problems 1 and 2. Finally, note that equation (4.18a)–(4.18b) preserves the divergence-free property, i.e., if the  $\nabla^{L^{2}}\Phi_{T}^{q}$  is divergence-free, then so is the  $\nabla^{H^{s}}\Phi_{T}^{q}$  and the  $L^{2}$  gradient is divergence-free by construction cf. (4.13a) and (4.15).

### 4.3.3 Gradient in the Lebesgue Space $L^q$

To compute the gradient in a  $L^q(\Omega)$  space for  $q \geq 3$  (in fact, the approach discussed below also works for q > 1, though the values q < 3 will not be considered here), we follow the method proposed in [35, 46, 40]. This gradient is, in fact, a metric gradient [23], which is a generalization of the notion of the gradient to normed spaces. It uses the fact that the gradient is the element that maximizes the directional derivative of the objective functional under certain constraints. In the absence of the Hilbert-space structure represented by an inner product and Theorem 2.3 (Riesz representation), we can then define the gradient of the objective functional (3.1) as a solution of the following optimization problem subject to the constraints inherited from Problems 1 and 2, which are the divergence-free and a fixed  $L^q$  norm properties,

$$\nabla^{L_q} \Phi_T^q = \underset{\|\boldsymbol{\Theta}\|_{L^q(\Omega)} = 1, \, \boldsymbol{\nabla}_{\mathbf{x}} \cdot \boldsymbol{\Theta} = 0}{\arg \max} \left\langle \boldsymbol{\nabla}^{L^2} \Phi_T^q, \boldsymbol{\Theta} \right\rangle_{(L^q(\Omega))^* \times L^q(\Omega)}. \tag{4.19}$$

Optimization problem (4.19) can be converted to an unconstrained form by introducing the Lagrange multipliers  $\mu \in \mathbb{R}$  and  $\eta \in L^q(\Omega)$  associated with each of these two constraints. We thus get

$$\nabla^{L^{q}} \Phi_{T}^{q} = \underset{\mu \in \mathbb{R}, \, \eta \in L^{q}(\Omega)}{\operatorname{arg \, max}} \left[ \left\langle \nabla^{L^{2}} \Phi_{T}^{q}, \Theta \right\rangle_{(L^{q}(\Omega))^{*} \times L^{q}(\Omega)} + \frac{\mu}{q} \left( \|\Theta\|_{L^{q}(\Omega)}^{q} - 1 \right) + \int_{\Omega} \eta \left( \nabla_{\mathbf{x}} \cdot \Theta \right) d\mathbf{x} \right], \quad (4.20)$$

where the expression in the bracket can be interpreted as the Lagrangian corresponding to the right-hand side of (4.19). After performing integration by parts, it becomes

$$\nabla^{L^q} \Phi_T^q = \underset{\mu \in \mathbb{R}, \, \eta \in L^q(\Omega)}{\arg \max} \int_{\Omega} \left( \mathbf{u}^*(0) \cdot \mathbf{\Theta} + \frac{\mu}{q} |\mathbf{\Theta}|^q - \frac{\mu}{q|\Omega|} - \mathbf{\Theta} \cdot \nabla_{\mathbf{x}} \, \eta \right) \, d\mathbf{x}. \quad (4.21)$$

Now, using the optimality condition requiring the Gâteaux differential of (4.21) with respect to  $\Theta$ ,  $\mu$  and  $\eta$  to vanish, we obtain the following expressions

$$\int_{\Omega} \left( \mathbf{u}^*(0) + \mu \boldsymbol{\nabla}^{L^q} \boldsymbol{\Phi}_T^q |\boldsymbol{\nabla}^{L^q} \boldsymbol{\Phi}_T^q|^{q-2} - \boldsymbol{\nabla}_{\mathbf{x}} \eta \right) \cdot \boldsymbol{\Theta}' \, d\mathbf{x} = 0, \qquad \forall \; \boldsymbol{\Theta}' \in L^q(\Omega), \quad (4.22a)$$

$$\int_{\Omega} |\mathbf{\Theta}|^q d\mathbf{x} = 1, \qquad \forall \; \mathbf{\Theta} \in L^q(\Omega), \qquad (4.22b)$$

$$\int_{\Omega} (\mathbf{\nabla}_{\mathbf{x}} \cdot \mathbf{\Theta}) \, \eta \, d\mathbf{x} = 0, \qquad \forall \, \eta \in L^{q}(\Omega). \tag{4.22c}$$

Conditions (4.22b) and (4.22c) trivially say that solutions of the optimization problem (4.19) have a fixed unit  $L^q(\Omega)$  norm and are divergence free. Since  $\Theta'$  is arbitrary, condition (4.22a) is equivalent to the following relation

$$\nabla^{L^q} \Phi_T^q |\nabla^{L^q} \Phi_T^q|^{q-2} = \frac{1}{\mu} \left( -\mathbf{u}^*(0) + \nabla_{\mathbf{x}} \eta \right), \quad \mathbf{x} \in \Omega.$$
 (4.23)

As mentioned by Protas in [46], expression (4.23) is similar to the Helmholtz-Weyl decomposition of vector fields in  $L^q(\Omega)$  [51], where a vector field in  $L^q(\Omega)$  can be written as the sum of a divergence-free vector field and the gradient of a certain potential. So then, noticing that both  $\mathbf{u}^*(0)$  and  $\nabla^{L^q}\Phi^q_T$  are divergence-free vector fields, applying the divergence operator to (4.23), we obtain an elliptic boundary-value problem which can be used to determine  $\eta$ 

$$\Delta \eta = \mu \left( \nabla_{\mathbf{x}} \left| \nabla^{L^q} \Phi_T^q \right|^{q-2} \right) \cdot \nabla^{L^q} \Phi_T^q, \quad \mathbf{x} \in \Omega$$
 (4.24)

which is subject to periodic boundary conditions. Therefore, to extract the gradient in the space  $L^q(\Omega)$ , it is necessary to solve the coupled non-linear system (4.23)-(4.24) subject to the normalization condition  $\|\nabla^{L^q}\Phi_T^q\|_{L^q(\Omega)} = 1$ . In other words, we need to solve the following non-linear system

$$\boldsymbol{\nabla}^{L^q} \boldsymbol{\Phi}_T^q | \boldsymbol{\nabla}^{L^q} \boldsymbol{\Phi}_T^q |^{q-2} = \frac{1}{\mu} \left( -\mathbf{u}^*(0) + \boldsymbol{\nabla}_{\mathbf{x}} \eta \right), \quad \mathbf{x} \in \Omega, \tag{4.25a}$$

$$\Delta \eta = \mu \left( \nabla_{\mathbf{x}} \left| \nabla^{L^q} \Phi_T^q \right|^{q-2} \right) \cdot \nabla^{L^q} \Phi_T^q, \quad \mathbf{x} \in \Omega, \tag{4.25b}$$

$$\|\boldsymbol{\nabla}^{L^q}\boldsymbol{\Phi}_T^q\|_{L^q(\Omega)} = 1. \tag{4.25c}$$

To find a solution of system (4.25), we proceed with an iterative splitting method as in [48], where at each iteration we first apply Newton's method with globalization to equation (4.25a) while keeping  $\eta$  fixed and then we apply a standard Poisson solver to equation (4.25b). Note that when q = 2, system (4.25) becomes

$$\nabla^{L^2} \Phi_T^q = \frac{1}{\mu} \left( -\mathbf{u}^*(0) + \nabla_{\mathbf{x}} \eta \right), \quad \mathbf{x} \in \Omega$$
 (4.26a)

$$\Delta \eta = 0, \quad \mathbf{x} \in \Omega. \tag{4.26b}$$

Since in this case  $\eta$  is a harmonic and periodic function defined on  $\Omega$ , then  $\eta$  is bounded. Hence  $\eta$  must be a constant function by Liouville's theorem. Therefore, equation (4.26a) becomes

$$\mathbf{\nabla}^{L^2} \Phi_T^q = -\frac{1}{\mu} \mathbf{u}^*(0),$$

which, up to normalization, is the same expression as in (4.15).

## 4.4 Limiting Case q = 3

For the limiting case q = 3, let us recall that the objective functional is, cf. (3.9),

$$\Psi_T(\mathbf{u}_0) := \|\mathbf{u}(T)\|_{L^3(\Omega)}^3 = \int_{\Omega} |\mathbf{u}(\mathbf{x}, T)|^3 d\mathbf{x}.$$

It is therefore necessary to reformulate the adjoint problem, although most of the the steps are quite similar to the case q > 3. The Gâteaux differential of (3.9) is

$$(\Psi_T)'(\mathbf{u}_0; \mathbf{u}_0') = 3 \int_{\Omega} |\mathbf{u}(\mathbf{x}, T)| \,\mathbf{u}(\mathbf{x}, T) \cdot \mathbf{u}' d\mathbf{x}, \tag{4.27}$$

where the perturbation field  $\mathbf{u}' = \mathbf{u}'(\mathbf{x}, t)$  is also a solution of the linearized Navier-Stokes system around the trajectory corresponding to the initial data  $\mathbf{u}_0$  (4.11). Since the expression in (4.27) for the Gâteaux differential is not in the Riesz form (4.9), we again need to introduce the *adjoint states*  $\mathbf{u}^*$  and  $p^*$  as in (4.12) and define the new adjoint system as

$$\mathcal{L}^* \begin{bmatrix} \mathbf{u}^* \\ p^* \end{bmatrix} := \begin{bmatrix} -\partial_t \mathbf{u}^* - \begin{bmatrix} \nabla_{\mathbf{x}} \mathbf{u}^* + (\nabla_{\mathbf{x}} \mathbf{u}^*)^T \end{bmatrix} \mathbf{u} - \nabla_{\mathbf{x}} p^* - \nu \Delta \mathbf{u}^* \\ -\nabla_{\mathbf{x}} \cdot \mathbf{u}^* \end{bmatrix} = \begin{bmatrix} \mathbf{0} \\ 0 \end{bmatrix}, \quad (4.28a)$$

$$\mathbf{u}^*(\mathbf{x}, T) = 3|\mathbf{u}(\mathbf{x}, T)|\mathbf{u}(\mathbf{x}, T), \quad \mathbf{x} \in \Omega, \ t \in [0, T]. \tag{4.28b}$$

This allows us to compute the  $L^2$  gradient of the objective functional (3.9) in the same way as in (4.15). Once the gradient in  $L^2$  is computed, we can now solve system (4.25) to obtain  $\nabla^{L^3}\Psi_T$ .

## 4.5 Projection, Retraction and Arc-Maximization

We use equation (4.5) to approximate a solution of Problems 1 and 3, where the projection operator  $\mathcal{P}_{\mathcal{T}_n\mathcal{M}_B}: H^s(\Omega) \to \mathcal{T}_n\mathcal{M}_B$  and the retraction operator  $\mathcal{R}_{\mathcal{M}_B}: \mathcal{T}_n\mathcal{M}_B \to \mathcal{M}_B$  are defined as in [28],

$$\mathcal{P}_{\mathcal{T}_{n}\mathcal{M}_{B}}\mathbf{z} := \overline{\mathbf{z}} - \frac{\left\langle \mathbf{z}, \nabla G_{q}\left(\mathbf{u}_{0;B,T}^{(n)}\right)\right\rangle_{H^{s}(\Omega)}}{\left\langle \overline{\nabla F_{q}\left(\mathbf{u}_{0;B,T}^{(n)}\right)}, \nabla G_{q}\left(\mathbf{u}_{0;B,T}^{(n)}\right)\right\rangle_{H^{s}(\Omega)}} \overline{\nabla G_{q}\left(\mathbf{u}_{0;B,T}^{(n)}\right)}, \tag{4.29}$$

and

$$\mathcal{R}_{\mathcal{M}_B}(\mathbf{z}) := \frac{B}{\|\mathbf{z}\|_{L^q(\Omega)}} \, \mathbf{z}, \text{ for all } \mathbf{z} \in \mathcal{T}_n \mathcal{M}_B, \tag{4.30}$$

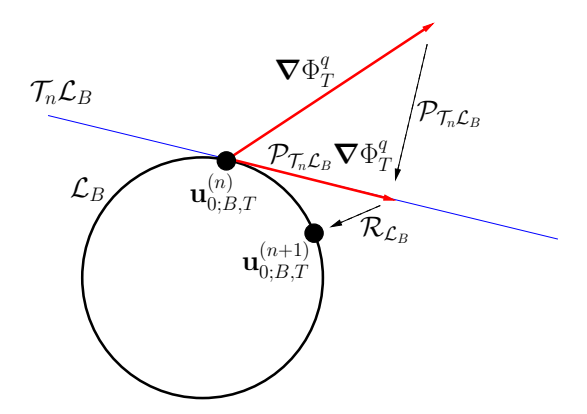


Figure 4.1: Schematic representation of how the projection operator (4.32) and the retraction operator (4.33) are used at each step in the iterations (4.7). The figure was taken from [28].

where  $\langle \nabla G_q(\mathbf{z}), \mathbf{z}' \rangle_{H^s(\Omega)} = \langle q | \mathbf{z} |^{q-2} \mathbf{z}, \mathbf{z}' \rangle_{\dot{H}^s(\Omega)}$ , for all  $\mathbf{z}' \in H^s(\Omega)$ . As regards Problems 2 and 4, the tangent space to the constraint manifold  $\mathcal{L}_B$  is defined using the function  $F_q(\mathbf{z}) := \|\mathbf{z}\|_{L^q(\Omega)}^q$ . Since  $F_q(\mathbf{z}) = B$  for all  $\mathbf{z} \in \mathcal{L}_B$ , we then have that

$$\langle \nabla F_q(\mathbf{z}), \mathbf{z}' \rangle_{(L^q(\Omega))^* \times L^q(\Omega)} = \langle q | \mathbf{z} |^{q-2} \mathbf{z}, \mathbf{z}' \rangle_{(L^q(\Omega))^* \times L^q(\Omega)} = 0, \tag{4.31}$$

for all  $\mathbf{z}' \in L^q(\Omega)$ . Note that given the nonlinearity of the term  $|\mathbf{z}|^{q-2}\mathbf{z}$ , the element  $\nabla F_{L^q}(\mathbf{z})$  does not, in general, satisfy the divergence-free and zero-mean conditions, even if they are satisfied by  $\mathbf{z}$ . Thus, the projection  $\mathcal{P}_{\mathcal{T}_n\mathcal{L}_B}: L^q(\Omega) \to \mathcal{T}_n\mathcal{L}_B$ , is defined in a similar way to what was done in [28], namely,

$$\mathcal{P}_{\mathcal{T}_{n}\mathcal{L}_{B}}\mathbf{z} := \overline{\mathbf{z}} - \frac{\left\langle \nabla F_{q} \left( \mathbf{u}_{0;B,T}^{(n)} \right), \overline{\mathbf{z}} \right\rangle_{(L^{q}(\Omega))^{*} \times L^{q}(\Omega)}}{\int_{\Omega} \nabla F_{q} \left( \mathbf{u}_{0;B,T}^{(n)} \right) \cdot \overline{\nabla F_{q} \left( \mathbf{u}_{0;B,T}^{(n)} \right)} d\mathbf{x}} \overline{\nabla F_{q} \left( \mathbf{u}_{0;B,T}^{(n)} \right)}, \tag{4.32}$$

for all  $\mathbf{z} \in L^q(\Omega)$ , which preserves the divergence-free and zero-mean properties of the argument. Observe that in this case, inner products have been replaced by duality

parings (2.10) due to the lack of Hilbert structure in Lebesgue spaces. The retraction operator  $\mathcal{R}_{\mathcal{L}_B}: \mathcal{T}_n\mathcal{L}_B \to \mathcal{L}_B$  is defined as the normalization [1]

$$\mathcal{R}_{\mathcal{L}_B}(\mathbf{z}) := \frac{B}{\|\mathbf{z}\|_{L^q(\Omega)}} \mathbf{z}, \quad \text{for all } \mathbf{z} \in \mathcal{T}_n \mathcal{L}_B.$$
 (4.33)

The step size  $\tau_n$  in the iterations (4.5) and (4.7) is computed by solving the problems

$$\tau_{n} = \arg\max_{\tau > 0} \Phi_{T}^{q} \left[ \mathcal{R}_{\mathcal{M}_{B}} \left( \mathbf{u}_{0;S,T}^{(n)} + \tau \mathcal{P}_{\mathcal{T}_{n}\mathcal{M}_{B}} \mathbf{\nabla}^{H^{s}} \Phi_{T}^{q} \left( \mathbf{u}_{0;B,T}^{(n)} \right) \right) \right]. \tag{4.34}$$

and

$$\tau_{n} = \arg\max_{\tau > 0} \Phi_{T}^{q} \left[ \mathcal{R}_{\mathcal{L}_{B}} \left( \mathbf{u}_{0;S,T}^{(n)} + \tau \mathcal{P}_{\mathcal{T}_{n}\mathcal{L}_{B}} \mathbf{\nabla}^{L^{q}} \Phi_{T}^{q} \left( \mathbf{u}_{0;B,T}^{(n)} \right) \right) \right], \tag{4.35}$$

respectively. They are solved using a variant of Brent's derivative-free algorithm [41, 44]. Equations (4.34) and (4.35) can be interpreted as a modification of the standard line-search problem with maximization performed following an arc (a geodesic in the limit of infinitesimal step sizes) lying on the constraint manifold  $\mathcal{L}_B$ , rather than along a straight line.

Computations involved in the discrete gradient flow (4.7) applied to solve Problem 2 are summarized as Algorithm 1.

**Algorithm 1** Solution of Problem 2 for fixed T and B.

#### Input:

B - size of the initial data.

T - time window.

 $\mathbf{u}_0$  - initial guess.

 $\epsilon$  - tolerance in the solution of optimization problem 2 via iterations (4.7).

 $N_{\text{max}}$  - maximum number of iterations allowed in (4.7).

#### **Output:**

Optimal initial data  $\tilde{\mathbf{u}}_{0:B,T} \in \mathcal{L}_B$ .

$$\mathbf{u}_{0:B,T}^{(0)} = \mathbf{u}_0$$

Compute  $\Phi_T^q(\mathbf{u}_0)$ 

n = 0

#### repeat

Solve the Navier-Stokes system with initial condition  $\mathbf{u}_{0:B,T}^{(n)}$ , see equation (1.1)

Solve the adjoint system to obtain  $\mathbf{u}^*$  and  $p^*$ , see equation (4.13)

Compute the 
$$L^2$$
 gradient  $\nabla^{L_2}\Phi_T^q\left(\mathbf{u}_{0;B,T}^{(n)}\right)$ , see equation (4.15)

Compute the Lebesgue gradient  $\nabla^{L^q} \Phi_T^q \left( \mathbf{u}_{0;B,T}^{(n)} \right)$ , see system (4.25)

Compute the optimal step size  $\tau_n$ , see equation (4.35)

Set 
$$\mathbf{u}_{0;B,T}^{(n+1)} = \mathcal{R}_{\mathcal{L}_B} \left( \mathbf{u}_{0;B,T}^{(n)} + \tau_n \mathcal{P}_{\mathcal{T}_n \mathcal{L}_B} \mathbf{\nabla}^{L^q} \Phi_T^q \left( \mathbf{u}_{0;B,T}^{(n)} \right) \right)$$

Evaluate the termination condition relative\_change  $=\frac{\Phi_T^q\left(\mathbf{u}_{0;B,T}^{(n+1)}\right)-\Phi_T^q\left(\mathbf{u}_{0;B,T}^{(n)}\right)}{\Phi_T^q\left(\mathbf{u}_{0;B,T}^{(n)}\right)}$ 

Set 
$$n = n + 1$$

 $\mathbf{until} \quad \mathtt{relative\_change} < \epsilon \text{ or } n > N_{\max}$ 

$$\widetilde{\mathbf{u}}_{0;B,T} = \mathbf{u}_{0;B,T}^{(n+1)}$$

## 4.6 Conjugate Gradient Method

In this section, we will describe the conjugate gradient method which is an accelerated version of the steepest descent method introduced in Section 4.1. First, we will show how it works in Hilbert spaces [41]. Then, we will present an adaptation of the method to solve constrained optimization problems on Lebesgue spaces  $L^q(\Omega)$ , leveraging ideas from Stein in [53], and Protas et al. in [14, 59].

### 4.6.1 Hilbert Space Formulation

The conjugate gradient method [41] is a powerful iterative algorithm to solve unconstrained optimization problems, especially involving quadratic objective functions and defined on a finite dimensional space because it can rapidly converge to the optimal state in a finite number of iterations. However, it is still a useful method when it is applied to non-convex problems on Hilbert spaces. Here, we will briefly describe the method in a standard setting. Assume we want to solve the following optimization problem,

$$\underset{u \in H}{\operatorname{arg\,max}} \ J(u), \tag{4.36}$$

where H is a Hilbert space with inner product  $\langle \cdot, \cdot \rangle_H$  and  $J: H \to \mathbb{R}$  is an objective functional. The conjugate gradient method approximates the optimal state  $\tilde{u}$  as

$$\widetilde{u} = \lim_{n \to \infty} u_n,$$

where the sequence of  $\{u_n\}_{n\in\mathbb{N}}$  is computed as

$$u_{n+1} = u_n + \alpha_n d_n, \quad n = 0, 1, 2, \dots$$
 (4.37)

with  $u_0$  being an initial guess and the conjugate directions  $d_n$  calculated as

$$d_0 = \nabla J(u_0),$$

$$d_n = \nabla J(u_n) + \beta_n d_{n-1}, \quad n = 1, 2, 3, \dots$$
(4.38)

where  $\beta_n$  is a "momentum" term that depends on the conjugate directions only. It can be chosen in different ways, however, in this thesis, we work with the Polak-Ribière momentum term  $\beta_n^{PR}$  defined as

$$\beta_n^{PR} := \frac{\langle \nabla J(u_n), \nabla J(u_n) - \nabla J(u_{n-1}) \rangle_H}{\langle \nabla J(u_{n-1}), \nabla J(u_{n-1}) \rangle_H}, \tag{4.39}$$

The parameter  $\alpha_n$  in (4.37) is chosen to be the value that maximizes the functional J along the direction  $d_n$  via line maximization, i.e.,

$$\alpha_n = \operatorname*{arg\,max}_{\alpha \in \mathbb{R}} J(u_n + \alpha d_n). \tag{4.40}$$

### 4.6.2 Riemannian Optimization

To solve a constrained optimization problem, we must address a key detail after characterizing a constraint manifold  $\mathcal{M}$  and its tangent bundle  $\mathcal{T}\mathcal{M}$  defined as [1]

$$\mathcal{TM} := \bigcup_{u \in \mathcal{M}} \mathcal{T}_u \mathcal{M}. \tag{4.41}$$

The terms on the right-hand side of expression (4.38) belong to different tangent spaces, the gradient  $\nabla J(u_n)$  is in the tangent space  $\mathcal{T}_{u_n}\mathcal{M}$  since it is evaluated at  $u_n$ , whereas the conjugate direction  $d_{n-1}$  lies in  $\mathcal{T}_{u_{n-1}}\mathcal{M}$ , as it is derived at the state  $u_{n-1}$ . Therefore, a proper setting needs to be defined for this addition. Also observe that the expression for the momentum (4.39) is subject to a similar issue when subtracting two gradients that belong to different tangent spaces. The formulation described below is taken from [14, 28, 59]. Let us consider the following constrained optimization problem

$$\underset{u \in \mathcal{M}}{\arg\max} J(u), \tag{4.42}$$

where J is an objective functional as in (4.36) and  $\mathcal{M}$  is a smooth manifold. We want to approximate a local maximizer  $\tilde{u}$  on  $\mathcal{M}$  with a sequence of elements  $\{u_n\}_{n\in\mathbb{N}}$  in  $\mathcal{M}$ such that

$$\widetilde{u} = \lim_{n \to \infty} u_n.$$

This sequence is defined as

$$u_{n+1} = \mathcal{R}_{\mathcal{M}} (u_n + \tau_n d_n), \quad n = 0, 1, ...,$$
 (4.43)

where  $u_0$  is an initial guess,  $d_n$  is a conjugate direction at  $u_n$ ,  $\mathcal{R}_{\mathcal{M}} : \mathcal{TM} \to \mathcal{M}$  is the retraction onto the manifold  $\mathcal{M}$  and  $\tau_n$  maximizes the functional J along the arc tangent to the direction  $d_n$  at  $u_n$ , i.e.,

$$\tau_n = \underset{\tau \in \mathbb{R}}{\operatorname{arg\,max}} \ J\left(\mathcal{R}_{\mathcal{M}}\left(u_n + \tau d_n\right)\right), \tag{4.44}$$

and the conjugate directions are computed as

$$d_0 = \mathcal{P}_{\mathcal{T}_0 \mathcal{M}} \nabla^{L^q} J(u_0), \quad d_{n+1} = \mathcal{P}_{\mathcal{T}_{n+1} \mathcal{M}} \nabla^{L^q} J(u_{n+1}) + \beta_{n+1}^{PR} \mathscr{T}_{\tau_n d_n} d_n, \tag{4.45}$$

for n = 0, 1, ..., where  $\mathcal{P}_{\mathcal{T}_n \mathcal{M}} : H \to \mathcal{T}_n \mathcal{M}$  is the projection onto the tangent space  $\mathcal{T}_n \mathcal{M}$ ,  $\mathcal{T}_n \mathcal{M} \times \mathcal{T}_n \mathcal{M} \to \mathcal{T}_{n+1} \mathcal{M}$  is the parallel vector transport. Given  $u, v \in \mathcal{T}_n \mathcal{M}$ , the parallel vector transport  $\mathcal{T}_u v \in \mathcal{T}_{n+1} \mathcal{M}$  of v along the direction u is defined as

$$\mathscr{T}_u(v) = \frac{d}{dt} \mathcal{R}(u+t \, v) \Big|_{t=0},$$

and  $\beta_n^{PR}$  is the Polak-Ribière momentum defined as in [14],

$$\beta_{n+1}^{PR} = \frac{\langle \mathcal{P}_{\mathcal{T}_{n+1}\mathcal{M}} \nabla^H J(u_{n+1}), \left( \mathcal{P}_{\mathcal{T}_{n+1}\mathcal{M}} \nabla^H J(u_{n+1}) - \mathcal{T}_{\tau_n d_n} \mathcal{P}_{\mathcal{T}_n \mathcal{M}} \nabla^H J(u_n) \right) \rangle_H}{\langle \mathcal{P}_{\mathcal{T}_n \mathcal{M}} \nabla^H J(u_n), \mathcal{P}_{\mathcal{T}_n \mathcal{M}} \nabla^H J(u_n) \rangle_H}. \tag{4.46}$$

The introduction of parallel vector transport is necessary because of the way the conjugate directions are updated. This process involves a linear combination of the gradient at the current iteration and the conjugate direction from the previous iteration. Since these two objects lie in different tangent spaces, the vectors must be mapped to the same space, so that their linear combination is well defined. This latter operation is realized by the parallel vector transport.

Explicit forms of the projection  $\mathcal{P}_{\mathcal{M}}$  and the retraction  $\mathcal{R}_{\mathcal{M}}$  depend on the structure of the manifold  $\mathcal{M}$ . However, if  $\mathcal{M}$  is given by with  $\mathcal{M}_B$  defined in (3.6), then the projection and the retractions are as in (4.29) and (4.30), respectively.

### 4.6.3 Riemannian Formulation in a Lebesgue Space

The following approach is an adaptation of the conjugate gradient method to solve a constrained optimization problem over a Banach space, where the main difficulty consists in the absence of an inner product structure. The main ideas were borrowed from Stein [53], who presents the conjugate gradient method in Banach spaces for unconstrained optimization problems, and Protas et al. [14, 59], where they implemented the conjugate gradient method in the context of Riemannian optimization problems on Hilbert spaces. A major obstacle here is the lack of Hilbert structure in the function spaces in which Problem 2 is formulated. However, we present a natural extension of the method to Lebesgue spaces where we generalize the notion of the gradient as the metric gradient [23], which is an element locally maximizing the Gâteaux differential of the objective functional with respect to the Lebesgue topology.

Assume we want to solve the following optimization problem

$$\underset{u \in \mathcal{L}}{\arg\max} J(u), \tag{4.47}$$

given a functional  $J: L^q(\Omega) \to \mathbb{R}, q > 1$ , with local maximizers constrained to a smooth manifold  $\mathcal{L}$ . We approximate a local maximizer  $\tilde{u}$  with a sequence of elements  $\{u_n\}_{n\in\mathbb{N}}$  in  $\mathcal{L}$  such that

$$\widetilde{u} = \lim_{n \to \infty} u_n.$$

This sequence is defined as

$$u_{n+1} = \mathcal{R}_{\mathcal{L}} (u_n + \tau_n d_n), \quad n = 0, 1, ....$$
 (4.48)

where  $u_0$  is an initial guess,  $d_n$  is a conjugate direction at  $u_n$ ,  $\mathcal{R}_{\mathcal{L}}$  is the retraction onto the manifold  $\mathcal{L}$  and  $\tau_n$  maximizes the functional J along the arc tangent to the direction  $d_n$  at  $u_n$ , i.e.,

$$\tau_n = \underset{\tau \in \mathbb{R}}{\operatorname{arg \, max}} \ J\left(\mathcal{R}_{\mathcal{L}}\left(u_n + \tau \, d_n\right)\right),\tag{4.49}$$

and the conjugate directions are computed as

$$d_0 = \mathcal{P}_{\mathcal{T}_0 \mathcal{L}} \nabla^{L^q} J(u_0), \quad d_{n+1} = \mathcal{P}_{\mathcal{T}_{n+1} \mathcal{L}} \nabla^{L^q} J(u_{n+1}) + \beta_{n+1}^{PR} \mathcal{T}_{\tau_n d_n} d_n, \tag{4.50}$$

for n = 0, 1, ..., where  $\mathcal{P}_{\mathcal{T}_n \mathcal{L}} v$  is the projection of v onto the tangent space  $\mathcal{T}_n \mathcal{L}$ ,  $\mathcal{T}_u v$  is the parallel vector transport of v along the direction u which is defined as

$$\mathscr{T}_u(v) = \frac{d}{dt} \mathcal{R}_{\mathcal{L}}(u+t \, v) \Big|_{t=0},$$

and  $\beta_n^{PR}$  is the Polak-Ribière momentum defined as

$$\beta_{n+1}^{PR} = \frac{J'\left(u_{n+1}; \mathcal{P}_{\mathcal{T}_{n+1}\mathcal{L}}\nabla^{L^q}J(u_{n+1})\right) - J'(u_n; \mathcal{T}_{-\tau_n d_n}\mathcal{P}_{\mathcal{T}_{n+1}\mathcal{L}}\nabla^{L^q}J(u_{n+1}))}{J'\left(u_n; \mathcal{P}_{\mathcal{T}_n\mathcal{L}}\nabla^{L^q}J(u_n)\right)}.$$
 (4.51)

As previously stated, the explicit expressions for the projection  $\mathcal{P}_{\mathcal{L}}$  and the retraction  $\mathcal{R}_{\mathcal{L}}$  depend on the manifold  $\mathcal{L}$ . However, if the manifold  $\mathcal{L}$  is defined as in (3.8), the projection and the retractions are defined as in (4.32) and (4.33), respectively. Expression (4.51) is defined by combining the results from [53] and expression (4.46).

# 4.7 Numerical Implementation

To solve the Navier-Stokes system (1.1) and the adjoint system (4.13) numerically, we use a standard approach [10]. For spatial discretization, we used a pseudospectral Galerkin method, and a semi-explicit Runge-Kutta method for time integration.

## 4.7.1 Discretization in Space

Suppose  $\mathbf{u}: \Omega \times [0,T] \to \mathbb{R}^3$  is a vector field with T > 0. Additionally, consider the set  $\mathcal{W}_N = \{ \mathbf{k} \in \mathbb{Z}^3 : k \leq N \}$  where  $k = |\mathbf{k}|$  and  $N \in \mathbb{N}^+$  is the spatial resolution. The Galerkin approximation of  $\mathbf{u}(\mathbf{x},t)$  is defined as

$$\mathbf{u}_{N}(\mathbf{x},t) := \sum_{\mathbf{k} \in \mathcal{W}_{N}} \widehat{\mathbf{u}}_{\mathbf{k}}(t) e^{2\pi i \mathbf{k} \cdot \mathbf{x}}, \tag{4.52}$$

where  $\hat{\mathbf{u}}_{k}(t) \in \mathbb{C}^{3}$  are the Fourier coefficients. If  $\mathbf{u}(\cdot,t) \in L^{1}(\Omega)$ , then its Fourier coefficients  $\hat{\mathbf{u}}_{k}(t)$  are computed as in (2.3). For  $\mathbf{u}_{N}$  to be an approximate solution of (1.1), its Fourier coefficients must satisfy the following finite-dimensional system of ordinary differential equations obtained by performing a Galerkin projection of system (1.1) onto the subspace spanned by the Fourier modes with wavenumbers lying within  $\mathcal{W}_{N}$ 

$$\frac{d\widehat{\mathbf{u}}_{k}(t)}{dt} + \mathbf{A}\,\widehat{\mathbf{u}}_{k}(t) + \mathbf{r}(\widehat{\mathbf{u}}_{k})(t) = \mathbf{0}, \quad \text{for all } \mathbf{k} \in \mathcal{W}_{N}, t \in (0, T),$$
(4.53a)

$$\hat{\mathbf{u}}_{k}(t) \cdot \mathbf{k} = 0, \quad \text{for all } \mathbf{k} \in \mathcal{W}_{N}, t \in (0, T),$$
 (4.53b)

$$\widehat{\mathbf{u}}_{k}(0) = [\widehat{\mathbf{u}_{0}}]_{k}, \quad \text{for all } k \in \mathcal{W}_{N}.$$
 (4.53c)

The linear and the nonlinear operators A and r are defined as:

$$\mathbf{A}\,\widehat{\mathbf{u}}_{\mathbf{k}}(t) := (2\pi)^2 \,k^2 \,\widehat{\mathbf{u}}_{\mathbf{k}}(t),\tag{4.54}$$

$$r(\widehat{\mathbf{u}}_{k})(t) := \left[\widehat{(\mathbf{u} \cdot \nabla_{\mathbf{x}}) \, \mathbf{u}}\right]_{k} - 2\pi \, i \, k \, \widehat{p}_{k},$$
 (4.55)

respectively. The Fourier coefficients of the nonlinear term,  $\left[\widehat{(\mathbf{u}\cdot\nabla_{\mathbf{x}})}\,\mathbf{u}\right]_{k}$ , are evaluated by first computing the product  $(\mathbf{u}\cdot\nabla_{\mathbf{x}})\,\mathbf{u}$  in the physical space and then calculating its Fourier transform, while the Fourier coefficients of the pressure term,  $\widehat{p}_{k}$ , are computed via the solution of the Poisson equation  $\Delta p = -\nabla_{\mathbf{x}} \cdot ((\mathbf{u}\cdot\nabla_{\mathbf{x}})\,\mathbf{u})$  subject to periodic boundary conditions, which is also performed in the Fourier space as

$$\widehat{p}_{k} = \frac{k}{k^{2}} \cdot \left[ \widehat{(\mathbf{u} \cdot \nabla_{\mathbf{x}}) \mathbf{u}} \right]_{k}. \tag{4.56}$$

Additionally, partial dealiasing is performed using the Gaussian filter [26]

$$g(\mathbf{k}) := e^{-36\left(\frac{3\,k}{2\,K}\right)^{36}}.\tag{4.57}$$

Tests performed using the standard dealiasing following the 3/2 rule [55] were also performed; however, in the results we did not observe any appreciable difference compared

to the use of the Gaussian filter (4.57). For the discretization of the solution of the adjoint system (4.13), the Fourier coefficients of the solution satisfy the following system of ordinary differential equations

$$\frac{d\widehat{\mathbf{u}}_{k}^{*}(t)}{dt} + \boldsymbol{S}\,\widehat{\mathbf{u}}_{k}^{*}(t) + \boldsymbol{R}\,\widehat{\mathbf{u}}_{k}^{*}(t) = \boldsymbol{0}, \qquad \text{for all } \boldsymbol{k} \in \mathcal{W}_{N}, \, t \in (0, T),$$
(4.58a)

$$\hat{\mathbf{u}}_{\mathbf{k}}^*(t) \cdot \mathbf{k} = 0,$$
 for all  $\mathbf{k} \in \mathcal{W}_N$ ,  $t \in (0, T)$ , (4.58b)

$$\widehat{\mathbf{u}}_{\mathbf{k}}^*(T) = \mathbf{0},$$
 for all  $\mathbf{k} \in \mathcal{W}_N$ . (4.58c)

where the linear operators  $\boldsymbol{S}$  and  $\boldsymbol{R}$  are defined as

$$\mathbf{S}\,\hat{\mathbf{u}}_{\mathbf{k}}^*(t) := (2\pi)^2 \,k\,\hat{\mathbf{u}}_{\mathbf{k}}^*(t),\tag{4.59}$$

$$\boldsymbol{R}\,\widehat{\mathbf{u}}_{\boldsymbol{k}}(t) := \left[\widehat{(\boldsymbol{\nabla}_{\mathbf{x}}\,\mathbf{u}^*)\,\mathbf{u}}\right]_{\boldsymbol{k}}(t) + \left[\widehat{(\boldsymbol{\nabla}_{\mathbf{x}}\,\mathbf{u}^*)^T\,\mathbf{u}}\right]_{\boldsymbol{k}}(t) - \widehat{\mathbf{f}}_{\boldsymbol{k}}(t)$$
(4.60)

and  $\hat{\mathbf{f}}_{k}(t)$  are the Fourier coefficients of the function  $\mathbf{f}(\mathbf{x},t)$  in (4.13b). The terms  $\widehat{(\nabla_{\mathbf{x}}\mathbf{u}^{*})\mathbf{u}}$  and  $\widehat{(\nabla_{\mathbf{x}}\mathbf{u}^{*})^{T}\mathbf{u}}$  are first evaluated in physical space as in (4.55), and then transformed to the Fourier space. Unlike system (4.53), system (4.58) has a terminal condition, meaning it needs to be integrated backwards in time.

#### 4.7.2 Discretization in Time

The integration in time is performed employing a hybrid approach combining the Crank-Nicolson method with a three-step Runge-Kutta method [10]. The scheme is given by

$$\left(I - \frac{h_{rk}}{2}\boldsymbol{A}\right)\widehat{\mathbf{u}}^{rk+1} = \widehat{\mathbf{u}}^{rk} + \frac{h_{rk}}{2}\boldsymbol{A}\widehat{\mathbf{u}}^{rk} + h_{rk}\beta_{rk}\boldsymbol{r}(\widehat{\mathbf{u}}^{rk}) + h_{rk}\zeta_{rk}\boldsymbol{r}(\widehat{\mathbf{u}}^{rk-1}), \tag{4.61}$$

where rk = 1, 2, 3 and

$$h_1 = \frac{8}{15}\Delta t$$
,  $h_2 = \frac{2}{15}\Delta t$ ,  $h_3 = \frac{1}{3}\Delta t$ ,

$$\beta_1 = 1, \qquad \beta_2 = \frac{25}{8}, \qquad \beta_3 = \frac{9}{4},$$

$$\zeta_1 = 0, \qquad \zeta_2 = -\frac{17}{8}, \qquad \zeta_3 = -\frac{5}{4}.$$

In this scheme,  $\hat{\mathbf{u}}^1$  and  $\hat{\mathbf{u}}^4$  represent the solutions of systems (4.53) and (4.58) at the current and future time, respectively. Important features to highlight concerning the numerical method (4.61) are an explicit and an implicit treatment of the nonlinear and linear part of equation (4.53), respectively. Treating the linear terms implicitly takes advantage of good stability properties that implicit methods offer, while the explicit treatment of the nonlinear term effectively linearizes it with respect to the time-dependent variable at the new time level such that this term is evaluated more readily. It is worth mentioning that, since the linear part of the Navier-Stokes system (1.1) is given by the Laplacian operator, inverting it in Fourier space is fairly simple given that it is diagonal in that space. Hybrid methods also allow for the use of coarser time steps in comparison with fully explicit numerical methods. A systematic validation of the numerical method (4.61) was carried out by Ayala in [4], whereas a validation of the gradients of the different objective functionals considered in this study is presented in Appendix C. As regards the computational time, solving Problems 1, 2, 3 and 4 took between  $\mathcal{O}(10)$  and  $\mathcal{O}(100)$  hours using  $\mathcal{O}(100)$  CPUs on Compute Canada systems.

# Chapter 5

# **Numerical Results**

In this chapter, we solve Problems 1, 2, 3 and 4 for different values of q, B, T, as well as different initial guesses  $\mathbf{u}^0$ , cf. (4.7). The problems were solved using different variants of the gradient descent method described in Chapter 4. Our analysis will focus on several integer values of p and q that satisfy relation (2.27) and the choice of the parameter s in (2.11) which will depend on the value of q. The dependence of the values of p and s on q is shown in Figures 3.1(a) and 3.1(b), respectively. In addition to q=4, 5, 9, we will also consider the limiting case q=3. Unless is stated otherwise, the numerical resolution is  $N=256^3$ . As regards the choice of the initial guess  $\mathbf{u}^0$ , we used the optimal initial conditions found by Kang et al. [29] to solve the the optimization problems with q=4. For the cases q=3, 5, and 9, we considered rescaled optimal initial conditions obtained for q=4 as initial guesses, in order to keep the Reynolds number Re [21] approximately equal at t=0 across all values of q. The reason for fixing the Reynolds number is to ensure that our computations are comparable across all the values of q. The number Re is computed using the so-called Taylor-scale Reynolds number defined in [21] as

$$Re := \sqrt{\frac{10}{3|\Omega|}} \frac{\mathcal{K}_0}{\nu \sqrt{\mathcal{E}_0}}.$$
 (5.1)

Additionally, we also examined random initial guesses.

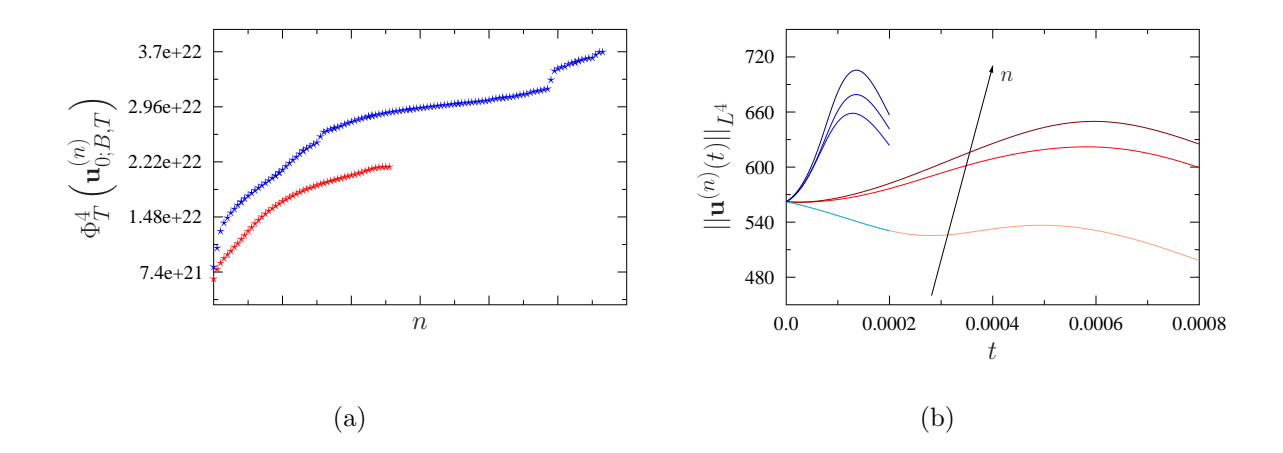


Figure 5.1: [q=4, B=562.34] (a) Dependence of the objective functional on iterations n while solving Problem 1 (blue) and Problem 2 (red). (b) Time evolution of the  $L^4(\Omega)$  norm of the velocity field at certain iterations n. Curves with darker colors correspond to later iterations closer to the local optimum of Problem 1 (blue) and Problem 2 (red). In both panels, blue and red curves correspond to optimization problems with  $T=2\times 10^{-4}$  and  $T=8\times 10^{-4}$ , respectively.

# 5.1 Extremal Flows in $L^4(\Omega)$

In this section, we fix q = 4 and vary the parameters B and T while solving Problems 1 and 2. Because of expression (2.33), we know that there is an explicit dependence between the minimum time  $\bar{t}$  for which a classical solution exists and the parameter B. Then, the minimum existence time of the solution of the Navier-Stokes equations (1.1) is of order  $\mathcal{O}(B^{-p})$ . Therefore, the choice of T should be adjusted according to expression (2.33) as the parameter B increases. Although a significant transient growth of the norm  $\|\mathbf{u}(t)\|_{L^4}$  was found, there was no evidence for it to become unbounded which would signal singularity formation according to (2.30). In Figure 5.1(a), we observe the convergence of the objective functional (3.1) with iterations n when the Lebesgue gradients and Sobolev gradients are used. The time window T is chosen such that it

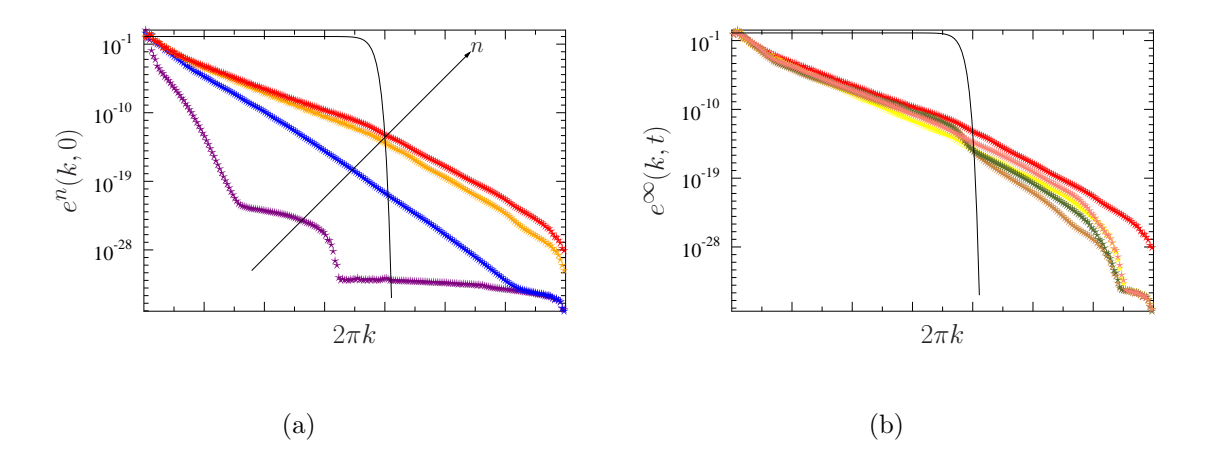


Figure 5.2: [q=4], Problem 1, B=562.34,  $T=2\times 10^{-4}]$  (a) Energy spectra of the approximations of the optimal initial condition obtained at different iterations n in the solution of Problem 1. (b) Energy spectra  $e^{\infty}(k,t)$  during the time evolution of the solution of the Navier-Stokes system (1.1) corresponding to the optimal initial condition  $\tilde{\mathbf{u}}_0$  (represented by red symbols). Black solid lines represent the Gaussian filter (4.57). Red symbols illustrate the optimal initial condition. The time instances in panel 5.2(b) are (red) t=0, (yellow)  $t=0.2\times 10^{-4}$ , (brown)  $t=1.2\times 10^{-4}$ , (green)  $t=1.6\times 10^{-4}$ , and (coral)  $t=2\times 10^{-4}$ .

corresponds to the largest value of the objective functional obtained with each type of gradient. The constraint parameter is fixed at B = 562.34. In Figure 5.1(b), we see how the time evolution of the  $L^4(\Omega)$  norm of the velocity field changes with iterations as we approach the local maxima.

Next, we analyze the evolution of the energy spectra defined as

$$e(k,t) := \frac{1}{2} \sum_{\substack{m \le |\boldsymbol{m}| < m+1 \\ \boldsymbol{m} \in \mathbb{Z}^3}} |\widehat{\mathbf{u}}_{\boldsymbol{m}}(t)|^2, \quad k = 2\pi \, m.$$
 (5.2)

We denote  $e^n(k,t)$  and  $e^{\infty}(k,t)$  as the energy spectra at iteration n and at the optimal state, respectively. Figures 5.2(a) and 5.3(a) show the energy spectra  $e^n(k,t)$  for different iterations n when solving Problems 1 and 2, respectively. The values of

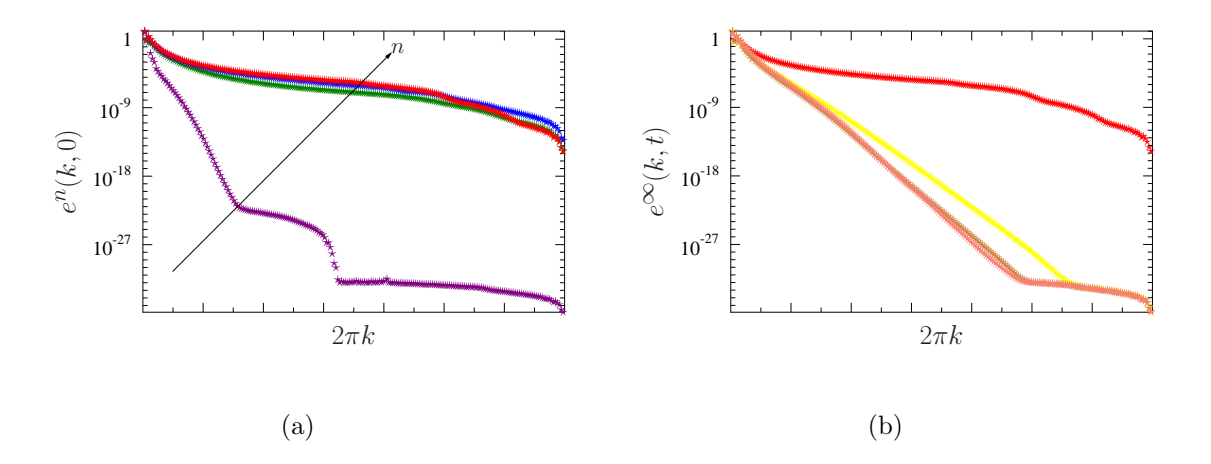


Figure 5.3:  $[q = 4, \text{ Problem 2}, B = 562.34, T = 8 \times 10^{-4}]$  (a) Energy spectra of the approximations of the optimal initial condition obtained at different iterations n in the solution of Problem 2. (b) Energy spectra  $e^{\infty}(k,t)$  during the time evolution of the solution of the Navier-Stokes system (1.1) corresponding to the optimal initial condition  $\tilde{\mathbf{u}}_0$  (represented by red symbols). The time instances indicated in panel 5.3(b) are (red) t = 0, (yellow)  $t = 1.6 \times 10^{-4}$ , (brown)  $t = 4 \times 10^{-4}$  and (coral)  $t = 8 \times 10^{-4}$ .

the parameters B and T are as in Figure 5.1. These figures show that, as expected, approximations of the optimal initial conditions  $\mathbf{u}_0^{(n)}$  tend to become less regular with iterations since the spectra decay less rapidly at later iterations. In fact, when using the Lebesgue gradients, we observe a drastic lost of regularity of the approximation of the optimal initial condition which occurs right after the first iteration. This is because these initial conditions are defined in the Lebesgue space  $L^4(\Omega)$  and therefore need not possess any regularity properties (only integrability).

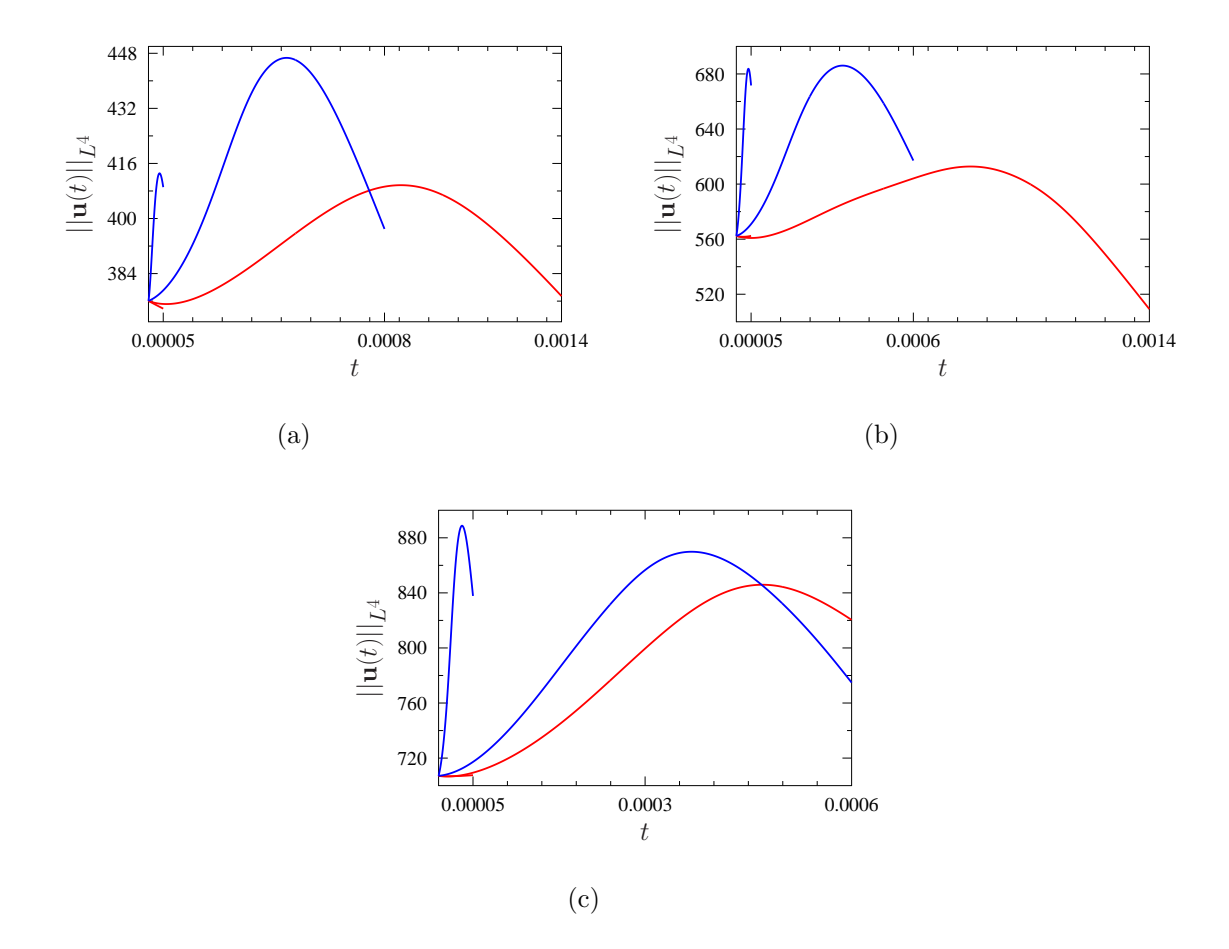


Figure 5.4: [q = 4] Time evolution of  $||\mathbf{u}(t)||_{L^4}$  for Navier-Stokes flows with the optimal initial conditions obtained by solving Problem 1 (blue) and Problem 2 (red). The values of the constraint parameter are (a) B = 376.06, (b) B = 562.34 and (c) B = 707.1. Solutions are computed over the time window [0,T] where T was chosen to be the shortest and longest considered time window for the given value of B.

Figures 5.3(b) and 5.2(b) show the time evolution of the energy spectra (5.2) in the solutions of the Navier-Stokes system (1.1) corresponding to the optimal initial conditions found by solving Problems 2 and 1, respectively. We see that, as a result of the regularizing property of the Navier-Stokes system, due to the presence of the viscous term, the solutions immediately become smooth, i.e.,  $\mathbf{u}(t) \in C^{\infty}(\Omega)$  for all t > 0

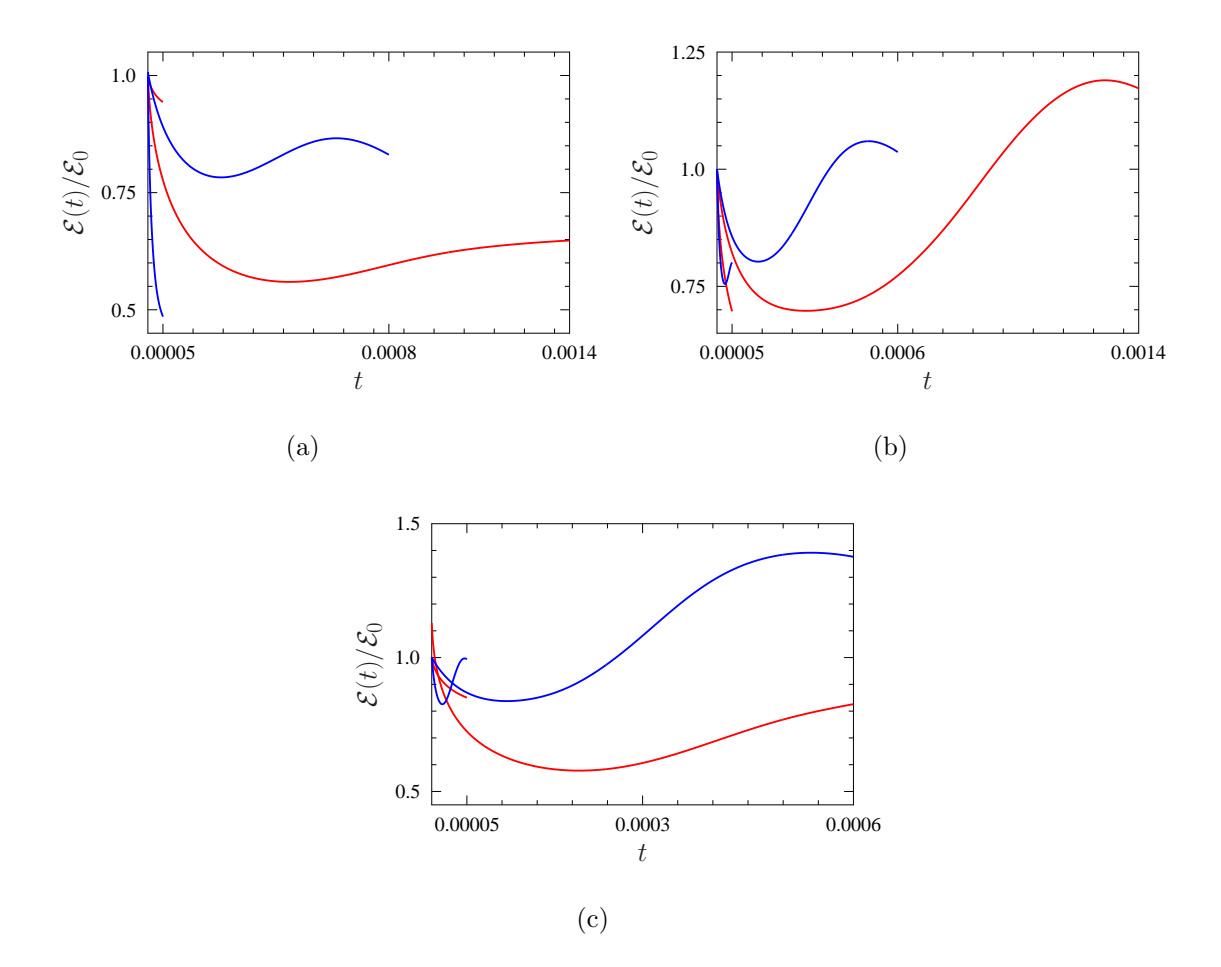


Figure 5.5: [q=4] Time evolution of the total enstrophy  $\mathcal{E}(\mathbf{u}(t))$  normalized with respect to the initial entrophy  $\mathcal{E}_0$  in the solutions of the Navier-Stokes system (1.1) corresponding to the optimal initial conditions obtained by solving Problem 1 (blue) and Problem 2 (red). The values of the constraint parameter are (a) B=376.06, (b) B=562.34 and (c) B=707.1. Solutions of (1.1) are computed over the time window [0,T] where T was chosen to be the shortest and longest considered for each value of B.

(Theorem 7.3 in [51]) when the initial condition is not smooth as is the case here. This is evident in the exponentially fast decay of the energy spectrum (5.2). Unlike Figure 5.3, Figure 5.2 exhibits the effect of the filter (4.57) on the spectra which is represented

by the black curve.

As a sign that our computations are well resolved, the filter acts only on Fourier coefficients with magnitudes not exceeding  $\mathcal{O}(10^{-10})$ . In Figures 5.4 (a)–(c), we show the time evolution of the  $L^4(\Omega)$  norm of the solution of the Navier-Stokes system (1.1), using the optimal initial conditions found by solving Problems 1 and 2 with B=376.06, B=562.34 and B=707.1, respectively. For each value of the constraint parameter B, the evolution of this norm is plotted for the shortest and longest time window considered T. We see that  $\|\mathbf{u}(t)\|_{L^4}$  attains its maximum earlier in time when we use the optimal initial conditions found by solving Problem 1. These maxima are also characterized by larger values of the objective functional than in the ones found by solving Problem 2. This is somewhat counterintuitive since solutions of Problem 2 are sought in a larger function space than the one considered in Problem 1.

The evolution of the enstrophy  $\mathcal{E}(t)$  normalized with respect to the initial enstrophy  $\mathcal{E}_0$  is displayed in Figure 5.5. Values of the parameters B, T, as well as the color coding is identical as in Figure 5.4. We observe that the enstrophy initially decays but then grows. The growth seems more prominent as the parameter B increases.

We also notice that the enstrophy decays at early times before experiencing any growth. This behavior was already reported by Kang et al. [28, 29].

#### 5.1.1 Branches of Local Maximizers

We define a "branch" as a family of local maximizers parametrized by the length of the time window T and obtained by solving Problem 1 or 2 with the parameter Bfixed. Kang et al. [29] characterized the structure of extremal flow based on certain spatial symmetries of the vorticity field reflected in the behavior of the componentwise enstrophy  $\mathcal{E}_i(t)$ , i = 1, 2, 3, providing information about the contributions to the total enstrophy (2.7) from the vorticity components in the different Cartesian directions. It

Symmetric	$\mathcal{E}_1 \sim \mathcal{E}_2 \sim \mathcal{E}_3$
Partially Symmetric	$\mathcal{E}_1 \sim \mathcal{E}_2 \nsim \mathcal{E}_3$ or
	$\mathcal{E}_1 \sim \mathcal{E}_3 \nsim \mathcal{E}_2$ or
	$\mathcal{E}_2 \sim \mathcal{E}_3 \nsim \mathcal{E}_1$
Asymmetric	$\mathcal{E}_1 \nsim \mathcal{E}_2 \nsim \mathcal{E}_3 \nsim \mathcal{E}_1$

Table 5.1: Definition of the symmetries of the velocity field based on the behavior of its componentwise enstrophy. The symbol " $\sim$ " means "similar in both magnitude and monotonicity" and " $\sim$ " is the negation of " $\sim$ ".

is defined as

$$\mathcal{E}_i(t) := \int_{\Omega} |(\nabla_{\mathbf{x}} \times \mathbf{u}(\mathbf{x}, t) \cdot \mathbf{e}_i)|^2 d\mathbf{x}, \quad i = 1, 2, 3,$$
(5.3)

where  $\{e_1, e_2, e_3\}$  is the canonical basis of  $\mathbb{R}^3$ . Naturally, we have the identity

$$\mathcal{E}(t) = \sum_{i=1}^{3} \mathcal{E}_i(t).$$

Three types of symmetries were identified based on the relative values of the componentwise enstrophies at different times t, namely, symmetric, partially symmetric and asymmetric and they are summarized in Table 5.1. In this work, however, we are not going to distinguish between partially symmetric and asymmetric configurations and will refer to both of them as "nonsymmetric".

In Figure 5.6(a) we show the dependance of the objective functional (3.1) on the length of the optimization window T for different values of the constraint B. In solutions of Problems 1 and 2, flows on each branch exhibit similar behavior of the norm  $||\mathbf{u}(t)||_{L^4(\Omega)}^4$  in time as already shown in Figure 5.4. In general, maximum values of the objective functional obtained by solving Problem 1, with optimization performed over the Sobolev space  $H^{3/4}$ , are larger than in Problem 2, where optimization is performed over the Lebesgue space  $L^4(\Omega)$ . Additionally, the flows corresponding to the solutions of Problem 1 are always nonsymmetric. All the branches reveal the presence of a sin-

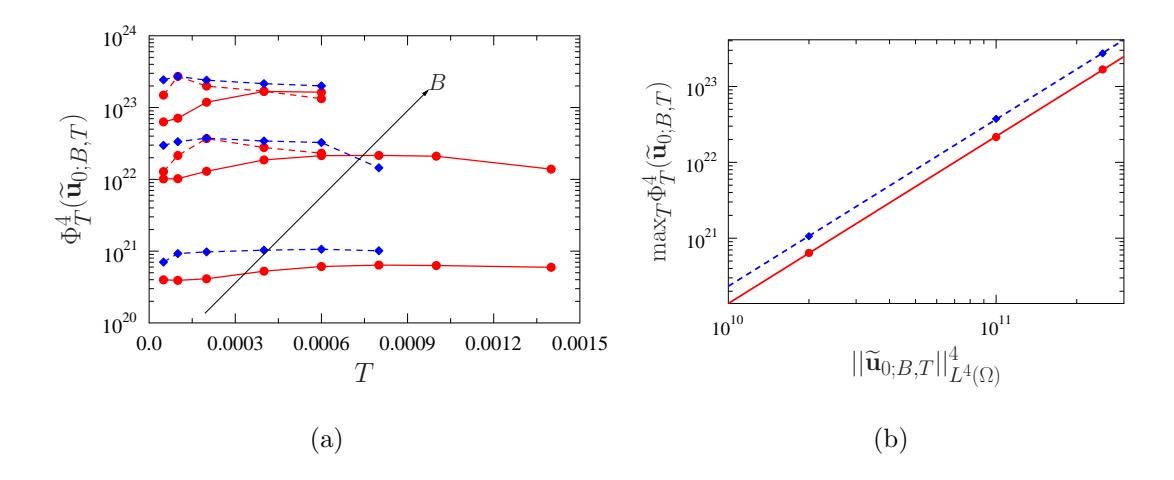


Figure 5.6: [q=4] (a) Dependence of the local maxima of the objective functional (3.1) on the length of the optimization window in Problems 1 (blue) and 2 (red) for different values of the constraint B=376.06, B=562.34 and B=707.1. Dashed and solid lines represent the nonsymmetric and symmetric branches, respectively, whereas the arrow indicates the trend with the increase of B. (b) Dependence of  $\max_T \Phi_T^4(\tilde{\mathbf{u}}_{0;B,T})$  on  $B^4=||\tilde{\mathbf{u}}_{0;B,T}||_{L^4(\Omega)}^4$ .

gle maximum which shifts towards smaller values of T as the value of the constraint parameter B increases. We also conclude that nonsymmetric branches produce larger values of the objective functional, consistent with the observations made by Kang et al. [28].

An interesting finding from Figure 5.6(a) is that local maximizers of Problem 1 are also local maximizers of Problem 2. To observe this, notice that the asymmetric branches obtained by solving Problem 2 and Problem 1 coincide for certain lengths of the time window ( $T = 10^{-4}$  and  $T = 2 \times 10^{-4}$  for the top and middle branches, respectively). Those points correspond to the maxima of branches obtained using Sobolev gradients. Such optimal initial conditions were then taken as initial guesses to construct asymmetric branches when solving Problem 2. However, no improvement in the objective functional was found compared to the solutions of Problem 1, suggesting the

above relation between the local maximizers of Problems 1 and 2.

We now aim to establish a relationship between the maximum value of the objective functional over each branch and the value of the constraint parameter  $B^q$  in the form

$$\max_{T} \Phi_{T}^{q} \left( \widetilde{\mathbf{u}}_{0;B,T} \right) \sim C \left( \left| \left| \widetilde{\mathbf{u}}_{0;B,T} \right| \right|_{L^{q}(\Omega)}^{q} \right)^{\gamma}, \quad \text{where } \gamma > 0.$$
 (5.4)

We quantify this dependence in Figure 5.6(b) by performing least-square fits,

$$\max_{T} \Phi_{T}^{4} \left( \widetilde{\mathbf{u}}_{0;B,T} \right) \sim 0.023 \left( ||\widetilde{\mathbf{u}}_{0;B,T}||_{L^{4}(\Omega)}^{4} \right)^{2.19}$$
(5.5)

for solutions of Problem 1 and

$$\max_{T} \Phi_{T}^{4} \left( \widetilde{\mathbf{u}}_{0;B,T} \right) \sim 0.012 \left( ||\widetilde{\mathbf{u}}_{0;B,T}||_{L^{4}(\Omega)}^{4} \right)^{2.20}$$
(5.6)

for solutions of Problem 2. The exponents in both of these relations are close to the exponent 2.26 that Kang & Protas found in [28]. In the absence of a rigorous a priori bound on the objective functional (2.28), relations (5.5)-(5.6) suggest how it might scale with the "size" of the the initial data in the worst case realized by solutions of Problems 1 and 2.

To understand whether or not the Navier-Stokes flows corresponding to the optimal initial conditions found by solving Problems 1 and 2 saturate a priori bounds on the rate of growth of the enstrophy and the  $L^4(\Omega)$  norm, cf. (2.19), (2.31) and (2.37), in Figure 5.7 we plot the corresponding time-dependent trajectories using the coordinates  $\{||\mathbf{u}(t)||_{L^4(\Omega)}, \frac{d}{dt}||\mathbf{u}(t)||_{L^4(\Omega)}\}$  and  $\{\mathcal{E}(t), d\mathcal{E}(t)/dt\}$ . Since these plots use a logarithmic scaling, parts of the trajectories where the quantity of interest is decreasing are not shown. The exponent  $\alpha$  in the relation  $dY(t)/dt \sim Y^{\alpha}$ , where Y is either  $||\mathbf{u}(t)||_{L^4(\Omega)}$  or  $\mathcal{E}(t)$ , is then represented by the slope of the tangent to the curve representing the trajectory at time t, which makes it possible to relate these results to the a priori bounds (2.19), (2.31) and (2.37). Unlike Figure 5.7(b), in Figure 5.7(a) the trajectories form clusters corresponding to different values of the parameter  $B^4$ .

In Section 2.3 we discussed the existence of a regime for potential blow-up in terms of the rate of change of the enstrophy and the  $L^q(\Omega)$  norm of velocity field in the Navier-Stokes flows. Figure 5.7 allows us to determine whether optimal solutions of Problems 1 and 2 fall into those regimes. In Figures 5.7(a) and 5.7(b), we show how the quantities of interest grow and how long their growth rates are sustained. For a finite-time blow-up to be possible, we would need to observe solutions where the rate of growth of the enstrophy and the  $L^4(\Omega)$  norm of the velocity field remain higher than the rate represented by the dashed lines, which indicate the minimum growth rate required for a flow to potentially develop a singularity. We identify some trajectories, such as the orange trajectory in Figure 5.7(a), which do show growth of the  $L^4(\Omega)$  norm of velocity field at a rate higher than the rate represented by the dashed line. However, this growth rate is not sustained sufficiently long for blow-up to occur and we eventually observe a depletion of the rate of change of the norm. A similar behavior is also found for the enstrophy in Figure 5.7(b), where we observe several trajectories exhibiting a growth rate higher than indicated by the slope of the dashed lines (see the green curve, for example). However, as was the case with the growth of the  $L^4(\Omega)$  norm, the rate of growth is not sustained long enough to give rise to a singularity. We then conclude that some solutions of the Navier-Stokes system (1.1) corresponding to optimal initial conditions obtained by solving Problems 1 and 2 do fall into the potential blow-up regime, although this behavior does not persist long enough to trigger a singularity.

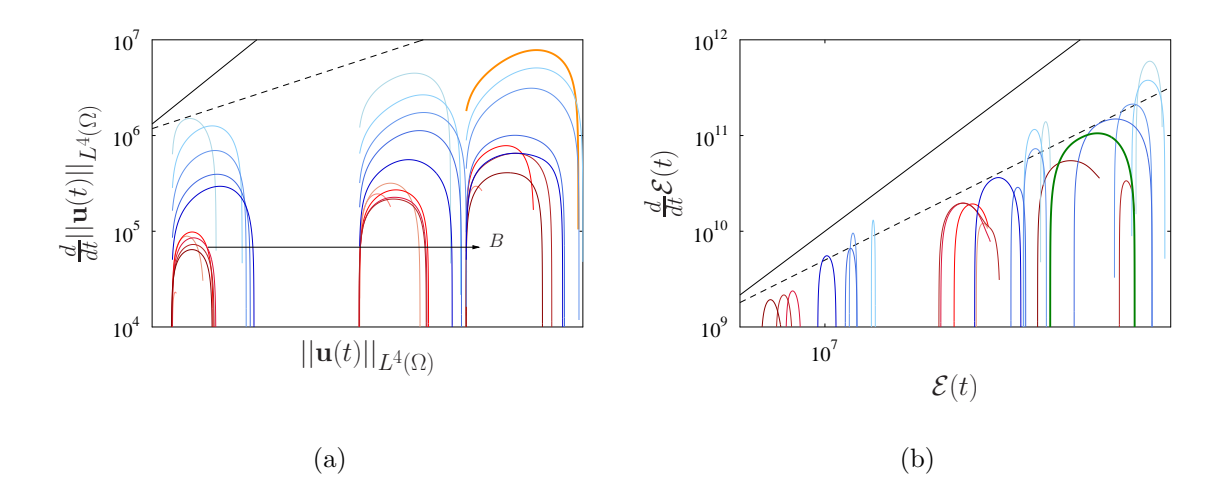


Figure 5.7: [q=4] Navier-Stokes flows corresponding to the optimal initial conditions found by solving Problem 1 and 2 for different B and T shown using the coordinates (a)  $\{||\mathbf{u}(t)||_{L^4(\Omega)}, \frac{d}{dt}||\mathbf{u}(t)||_{L^4(\Omega)}\}$  and (b)  $\{\mathcal{E}(t), d\mathcal{E}(t)/dt\}$ . Black solid lines show the upper bounds on the rate of change of the  $L^4(\Omega)$  norm of the solution and of the enstrophy given by the relations (a)  $\frac{d}{dt} ||\mathbf{u}(t)||_{L^4(\Omega)} \sim ||\mathbf{u}(t)||_{L^4(\Omega)}^9$  from (2.31) and (b)  $d\mathcal{E}/dt \sim \mathcal{E}^3$ , respectively. Dashed lines show the relations  $\frac{d}{dt} ||\mathbf{u}(t)||_{L^4(\Omega)} \sim ||\mathbf{u}(t)||_{L^4(\Omega)}^{11/3}$  from (2.37) and  $d\mathcal{E}/dt \sim \mathcal{E}^2$  in (a) and (b), respectively. Blue trajectories are optimal solutions of Problem 1 while red trajectories are solutions of Problem 2. The intensity of the color increases with the length of the time window T. The time evolution of the vorticity field in the trajectories marked orange and green is presented in Figures 5.12 and 5.14.

#### 5.1.2 Structure of the Extremal Flows

We will now discuss the structure of the extremal flows belonging to the different branches shown in Figure 5.6(a). Figures 5.8 and 5.9 show the time evolution of the componentwise enstrophies (5.3) for different values of the constraint parameter B in solutions of Problem 1 and 2, respectively. We were also able to capture nonsymmetric branches in Problem 2 with the two largest values of the constraint parameter B and the evolution of the componentwise enstrophy in these flows is shown in Figure 5.10.

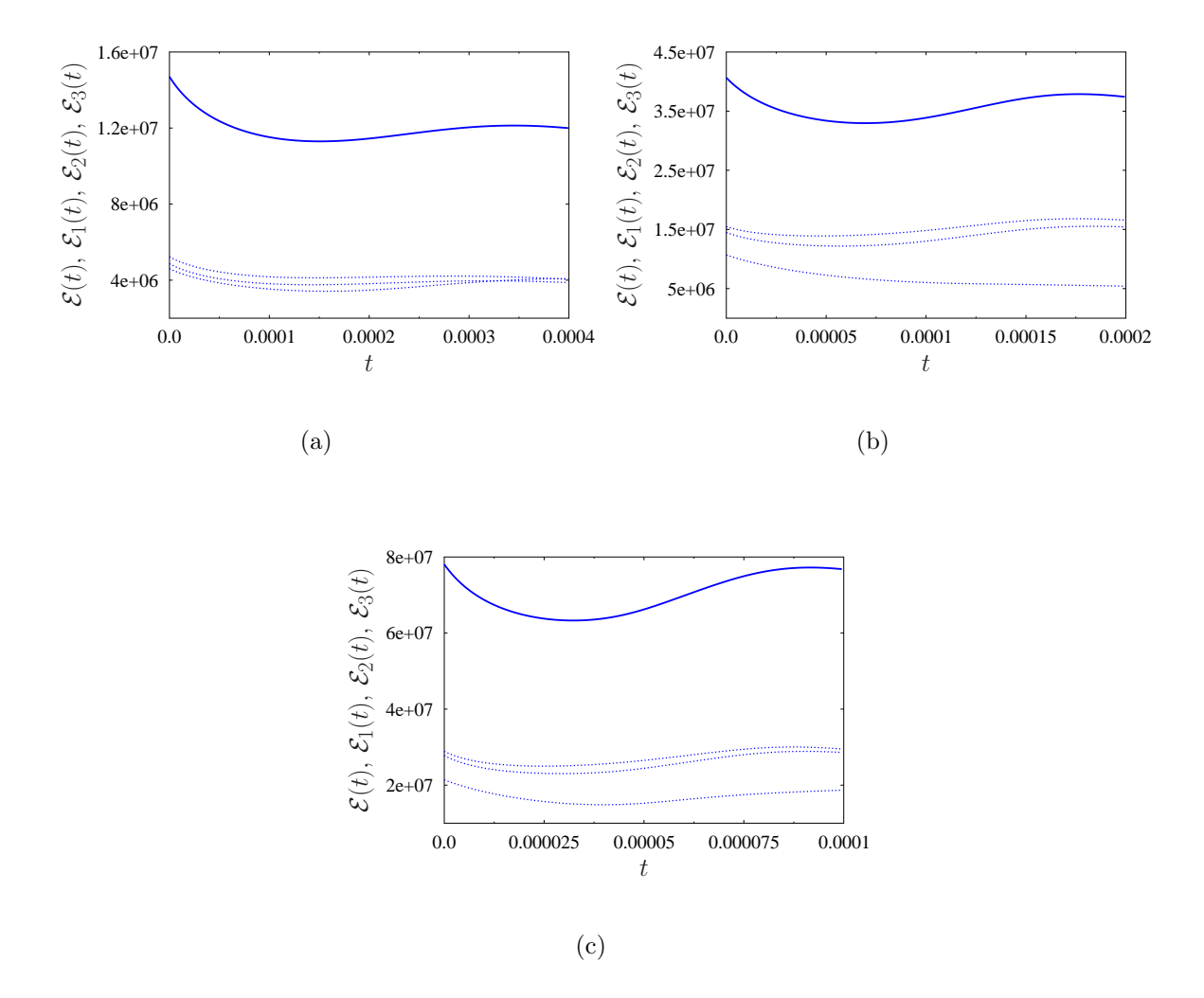


Figure 5.8: [q = 4, Problem 1, nonsymmetric flows] Evolution of (solid lines) the total enstrophy  $\mathcal{E}(t)$  and (dotted lines) the componentwise enstrophies  $\mathcal{E}_1(t)$ ,  $\mathcal{E}_2(t)$  and  $\mathcal{E}_3(t)$  for optimal solutions of Problem 1. The values of the parameters are (a) B = 376.06,  $T = 8 \times 10^{-4}$  (b) B = 562.34,  $T = 8 \times 10^{-4}$  and (c) B = 707.1,  $T = 4 \times 10^{-4}$ .

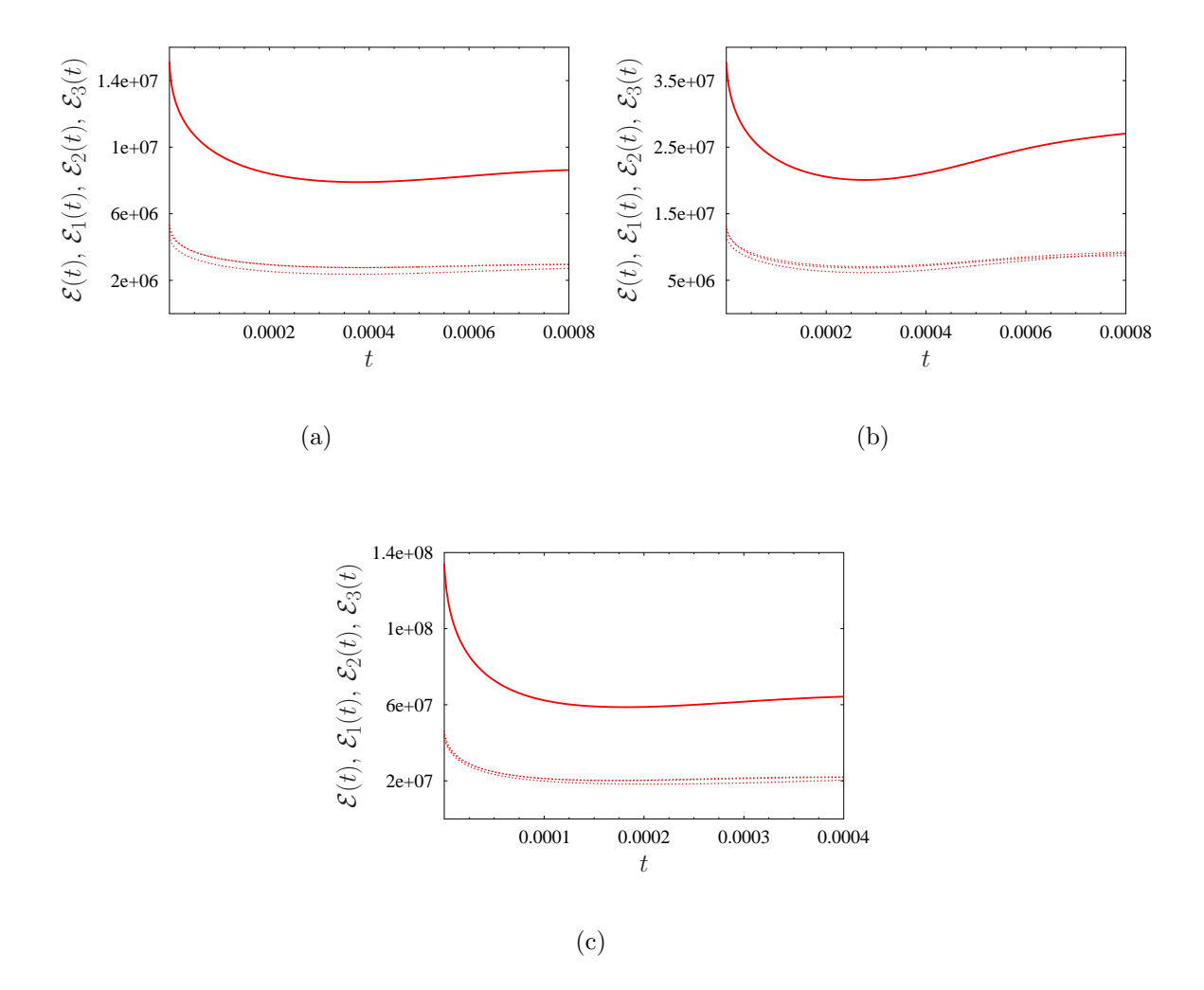


Figure 5.9: [q=4], Problem 2, symmetric flows] Evolution of (solid lines) the total enstrophy  $\mathcal{E}(t)$  and (dotted lines) the componentwise enstrophies  $\mathcal{E}_1(t)$ ,  $\mathcal{E}_2(t)$  and  $\mathcal{E}_3(t)$  for optimal solutions of Problem 2. The values of the parameters are (a) B=376.06,  $T=8\times 10^{-4}$  (b) B=562.34,  $T=8\times 10^{-4}$  and (c) B=707.1,  $T=4\times 10^{-4}$ .

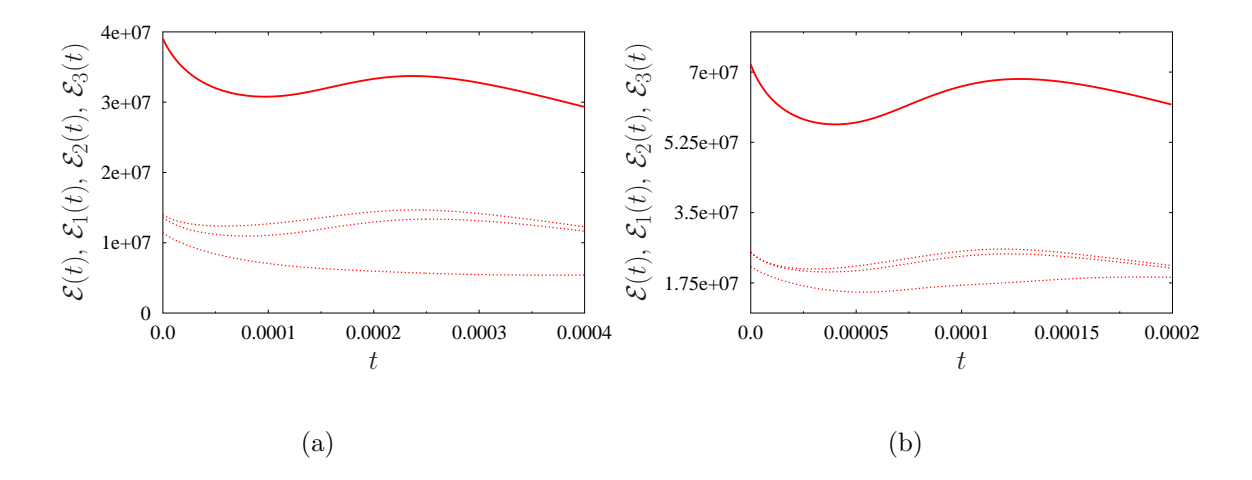


Figure 5.10: [q = 4, Problem 2, nonsymmetric flows] Evolution of (solid lines) the total enstrophy  $\mathcal{E}(t)$  and (dotted lines) the componentwise enstrophies  $\mathcal{E}_1(t)$ ,  $\mathcal{E}_2(t)$  and  $\mathcal{E}_3(t)$  for optimal solutions of Problem 2. The values of the parameters are (a) B = 562.34,  $T = 4 \times 10^{-4}$  and (b) B = 707.1,  $T = 2 \times 10^{-4}$ .

The time window in each panel corresponds to when the objective functional reaches its maximum on each branch.

Below we visualize flow fields focusing on their velocity  $\mathbf{u}(\mathbf{x}, t)$  and vorticity  $\boldsymbol{\omega}(\mathbf{x}, t)$ . More specifically, we will show  $|\boldsymbol{\omega}(\mathbf{x}, t_i)|$  and  $|\mathbf{u}(\mathbf{x}, t_i)|^4$  at different time instances  $t_i$  with i = 0, ..., 3, defined as follows.

**Definition 5.1.** The time instances  $t_i$ , i = 0, ..., 3, where we analyze the magnitude of the vorticity  $|\omega(\mathbf{x}, t)|$  and  $|\mathbf{u}(\mathbf{x}, t)|^q$  are

- $t_0$  is the initial time, i.e.,  $t_0 = 0$ ,
- $t_1 \approx \operatorname{argmax}_{t \in [0,T]} \frac{d}{dt} \|\mathbf{u}(t)\|_{L^q(\Omega)}$
- $t_2 \approx \operatorname{argmax}_{t \in [0,T]} \|\mathbf{u}(t)\|_{L^q(\Omega)}$ ,
- $t_3$  is the final time, i.e.,  $t_3 = T$ .

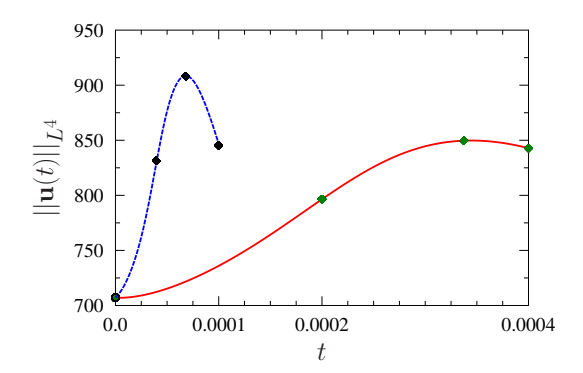


Figure 5.11: [q = 4, B = 707.1] Time evolution of the norm  $\|\mathbf{u}(t)\|_{L^4}$  in the flow with the optimal initial condition that produces the maximum value of the objective functional for the largest value of the constraint in Problem 1 (blue) and Problem 2 (red). Black and green symbols represent the time instances  $t_i$ , i = 0, ..., 3, in Definition 5.1, when the flow is visualized in Figures 5.12 and 5.13.

These times are indicated in Figures 5.11 and 5.24. The quantities  $|\boldsymbol{\omega}(\mathbf{x}, t_i)|$  and  $|\mathbf{u}(\mathbf{x}, t_i)|^q$  are shown in Figures 5.12 and 5.13 for the Navier-Stokes flows with the optimal initial conditions found by solving Problems 1 and 2.

The flow structures shown in Figure 5.12 are quite similar to what was found by Kang & Protas [28]. We observe a bent vortex ring that stretches as time evolves. We also note that the maxima of  $|\mathbf{u}(\mathbf{x},t)|^4$  occur within the gap formed by the vortex ring as it entangles and these are precisely the regions driving the growth of the objective functional (3.1). As regards the solutions of Problem 2, the time evolution of the vorticity is shown in Figure 5.13. While at the initial instant t=0 there is no clear pattern in the flow, as the time evolves we observe the formation of two tightly spaced vortex tubes which are stretched to fill the entire flow domain  $\Omega$ . Figure 5.14 shows the time evolution of the vorticity of the solution of the Navier-Stokes system (1.1) represented by the trajectory marked in green in Figure 5.7(b). Interestingly, it also features two vortex rings approaching each other while also expanding to fill the entire flow domain.

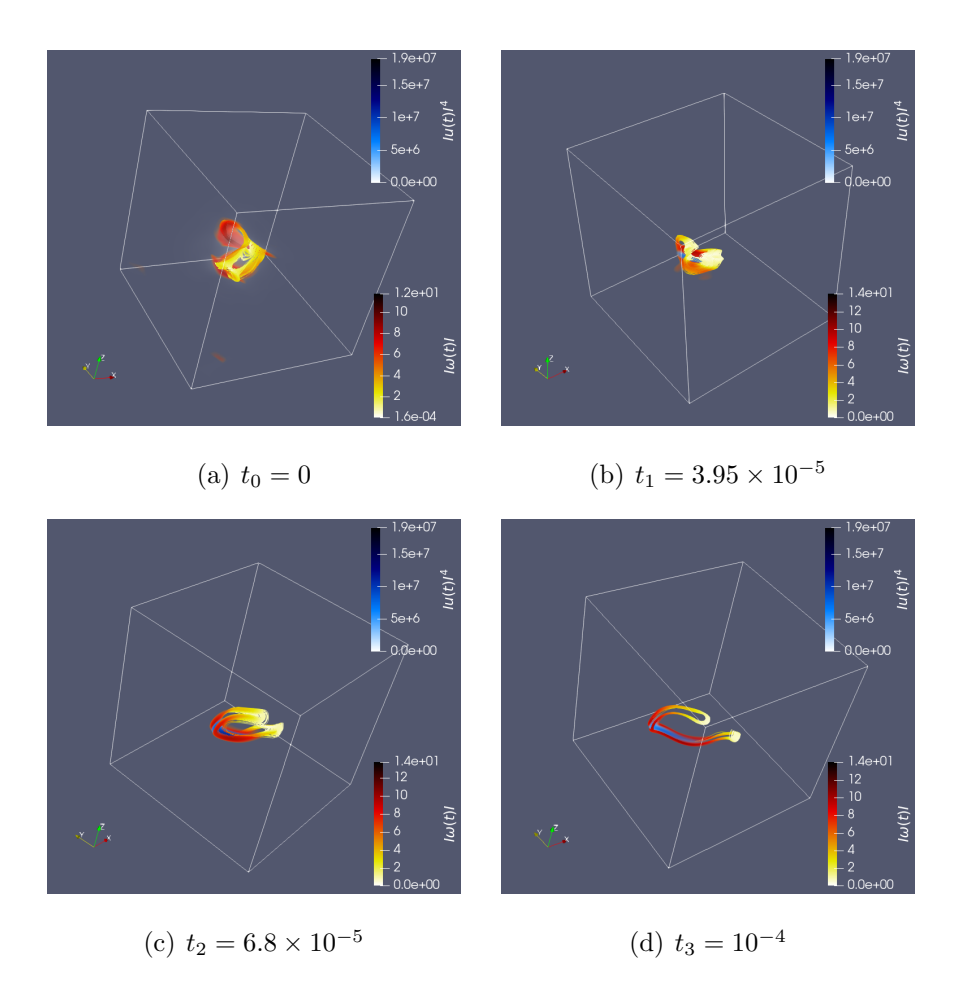


Figure 5.12:  $[q = 4, \text{Problem 1}, B = 707.1 \text{ and } T = 10^{-4}]$  Snapshots of the magnitude of the vorticity  $|\boldsymbol{\omega}(\mathbf{x}, t_i)|$  (red) in the solution of the Navier-Stokes system (1.1) along with vortex lines (red) and the quantity  $|\mathbf{u}(\mathbf{x}, t_i)|^4$  (blue) shown at the times  $t_0, ..., t_3$  defined in Definition 5.1. The values of the parameters B and T correspond to the maximum over the branch with the largest value of B in Figure 5.6(a). The trajectory representing this solution is marked in orange in Figure 5.7(a).

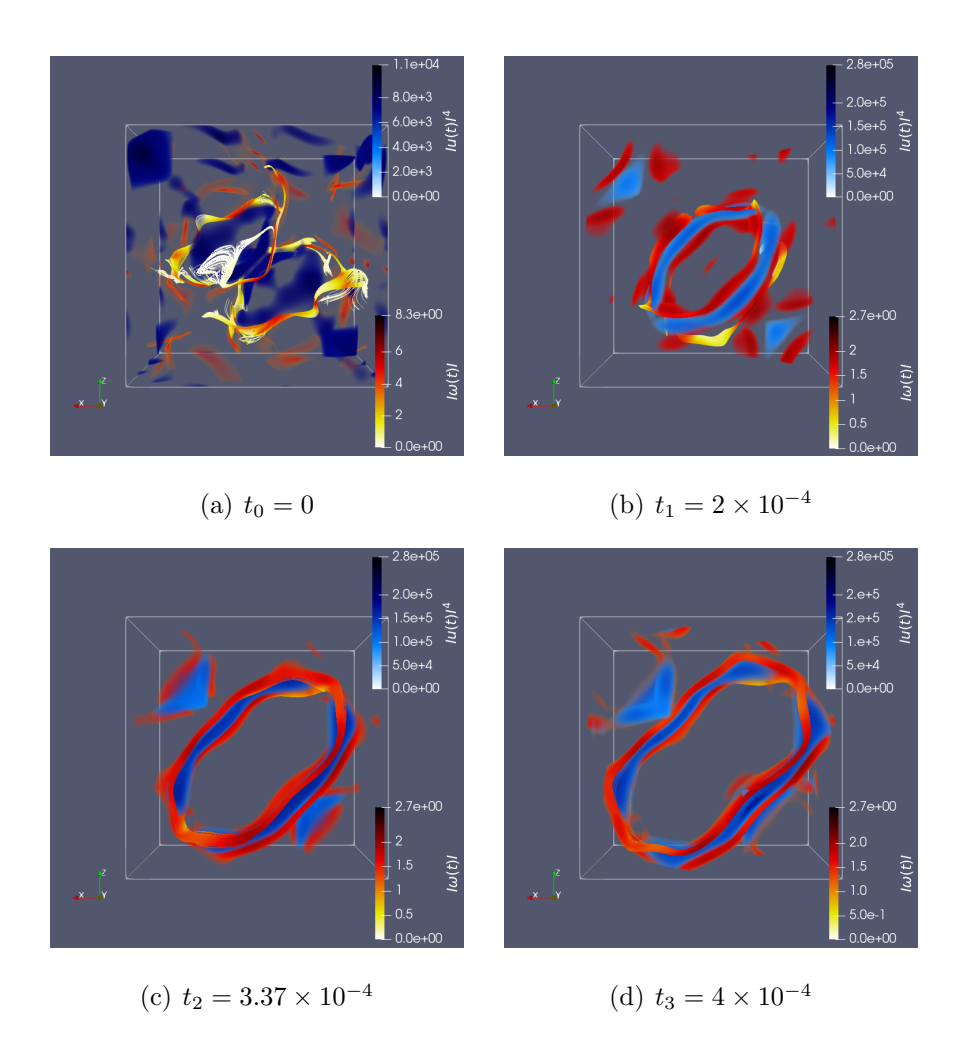


Figure 5.13:  $[q = 4, \text{ Problem 2}, B = 707.1 \text{ and } T = 4 \times 10^{-4}]$  Snapshots of the magnitude of the vorticity  $|\boldsymbol{\omega}(\mathbf{x}, t_i)|$  (red) in the solution of the Navier-Stokes system (1.1) along with vortex lines (red) and the quantity  $|\mathbf{u}(\mathbf{x}, t_i)|^4$  (blue) shown at the times  $t_0, ..., t_3$  defined in Definition 5.1. The values of the parameters B and T correspond to the maxima over the symmetric branch with the largest value of B in Figure 5.6(a).

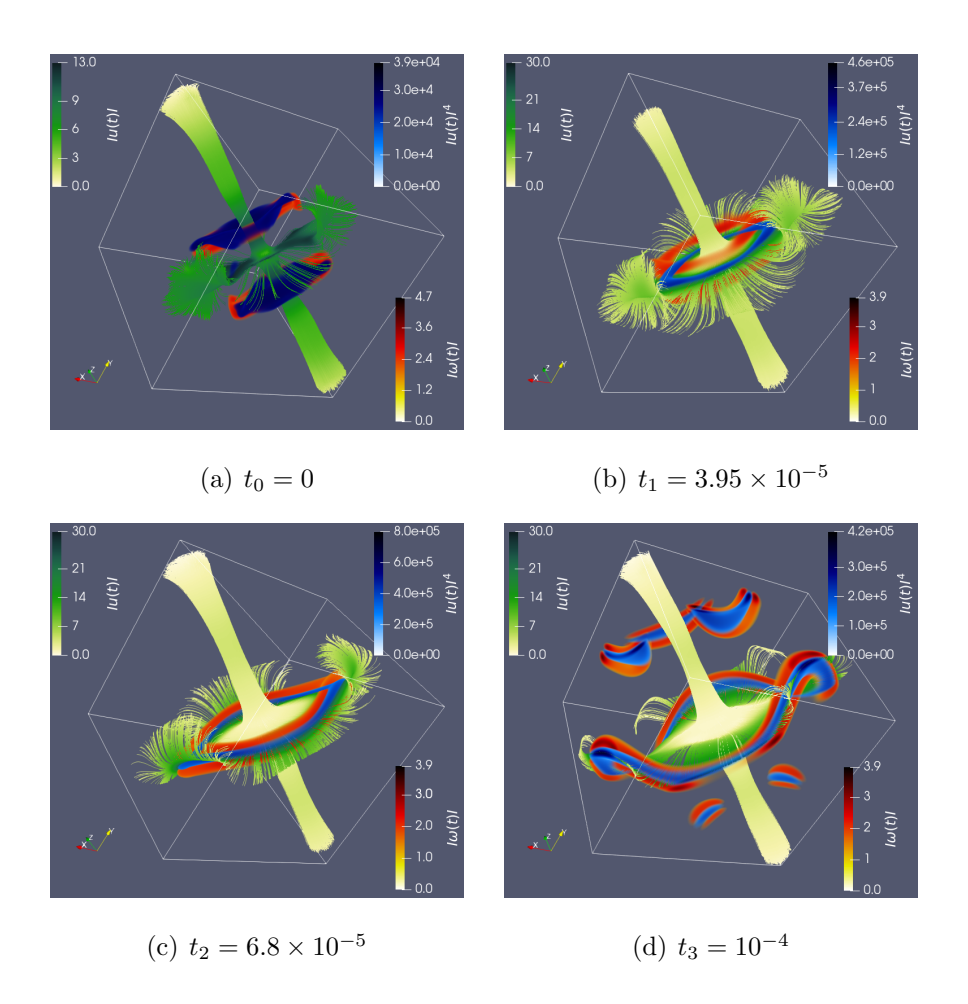


Figure 5.14:  $[q = 4, \text{ Problem 1}, B = 707.1 \text{ and } T = 4 \times 10^{-4}]$  Snapshots of the magnitude of the vorticity  $|\boldsymbol{\omega}(\mathbf{x}, t_i)|$  (red) in the solution of the Navier-Stokes system (1.1) along with vortex lines (red), the quantity  $|\mathbf{u}(\mathbf{x}, t_i)|^4$  (blue) and streamlines of the solution (green) shown at the times  $t_0, ..., t_3$  defined in Definition 5.1. The values of the parameters B and T correspond to the green trajectory in Figure 5.7(b).

# **5.2** Extremal Flows in $L^5(\Omega)$

In this section, we consider q = 5 while varying the parameters B and T in Problems 1 and 2. Similarly to the case with q = 4, although we did observe some growth of the

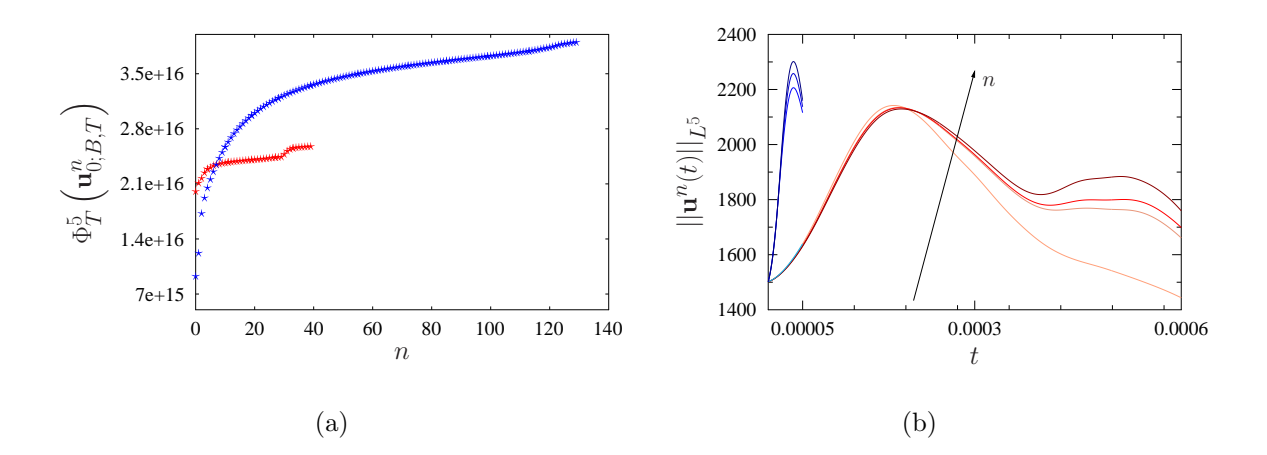


Figure 5.15:  $[q=5,\,B=1500.2]$  (a) Dependence of the objective functional on the iteration n when solving Problem 1 (blue) and Problem 2 (red). (b) Time evolution of the  $L^5(\Omega)$  norm of the velocity field at certain iterations n. Curves with darker colors correspond to later iterations closer to the local optimum of Problem 1 (blue) and Problem 2 (red). Blue and red curves correspond to optimization problems with  $T=5\times 10^{-5}$  and  $T=6\times 10^{-4}$ , respectively.

norm  $\|\mathbf{u}(t)\|_{L^5}$ , we did not find evidence for its unbounded growth that could signal singularity formation according to (2.30). In Figure 5.15(a), we observe the convergence of the objective functional (3.1) with iterations n when the Sobolev gradients and Lebesgue gradients are used to solve Problems 1 and 2, respectively. The time window T is chosen such that it corresponds to the largest value of the objective functional obtained when solving Problems 1 and 2 for the given value of the constraint B = 1500.2. In Figure 5.15(b), we see how the time evolution of the  $L^5(\Omega)$  norm of the velocity field changes with iterations as we approach the local maxima.

The evolution of the energy spectra (5.2) at different iterations in solutions of Problems (1) and (2) is presented in Figures 5.16(a) and 5.17(a), respectively. In the case q = 4, we observed a clear difference in the regularity of the initial conditions between the two problems (see Figures 5.2(b) and 5.3(b)); however, here we do not observe

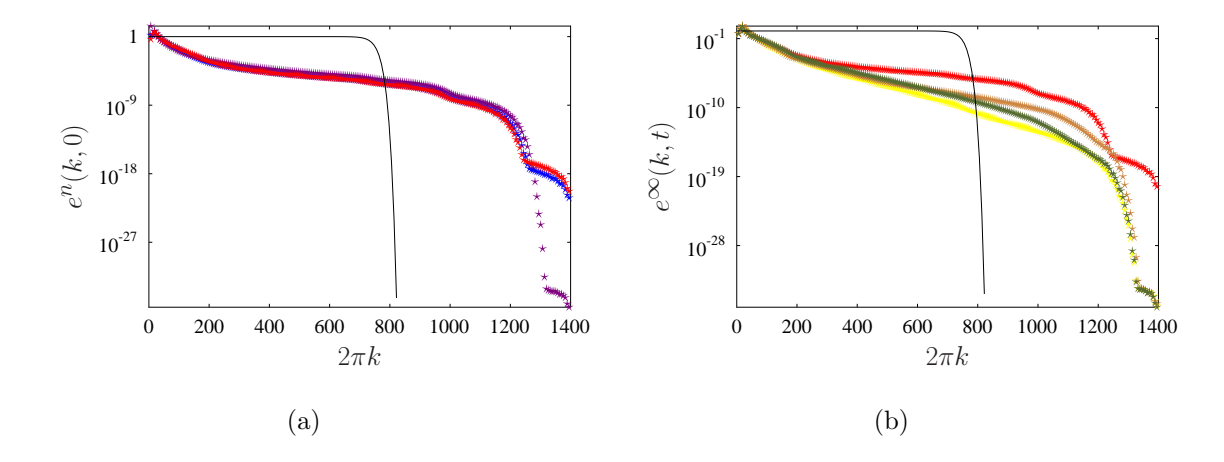


Figure 5.16: [q=5], Problem 1, B=867,  $T=10^{-4}]$  (a) Energy spectra of the approximations of the optimal initial condition obtained at different iterations n in the solution of Problem 1. (b) Energy spectra  $e^{\infty}(k,t)$  during the time evolution of the solution of the Navier-Stokes system (1.1) corresponding to the optimal initial condition  $\tilde{\mathbf{u}}_0$  (represented by red symbols). The time instances indicated in panel (b) are (red) t=0, (yellow)  $t=4\times10^{-5}$ , (brown)  $t=8\times10^{-5}$ , and (green)  $t=10^{-4}$ . Black solid lines represent the Gaussian filter (4.57).

such a distinction. This is explained by the choice of the initial guess, which will be discussed in a later section. Figures 5.16(b) and 5.17(b) show the time evolution of the energy spectra (5.2) in the solutions of the Navier-Stokes system (1.1) corresponding to the optimal initial conditions found by solving Problems 1 and 2, respectively. As was the case for q = 4, we observe that, as a result of the regularizing property of the Navier-Stokes system, solutions become smoother than the initial condition. Figures 5.16 and 5.17 exhibit the effect of the filter (4.57) on the spectra. A sign that our computations are well resolved is that the filter acts only on Fourier coefficients with magnitudes not exceeding  $\mathcal{O}(10^{-8})$ .

In Figures 5.18 (a)–(c), we show the time evolution of the  $L^5(\Omega)$  norm of the solution of the Navier-Stokes system (1.1), using the optimal initial conditions found by solving

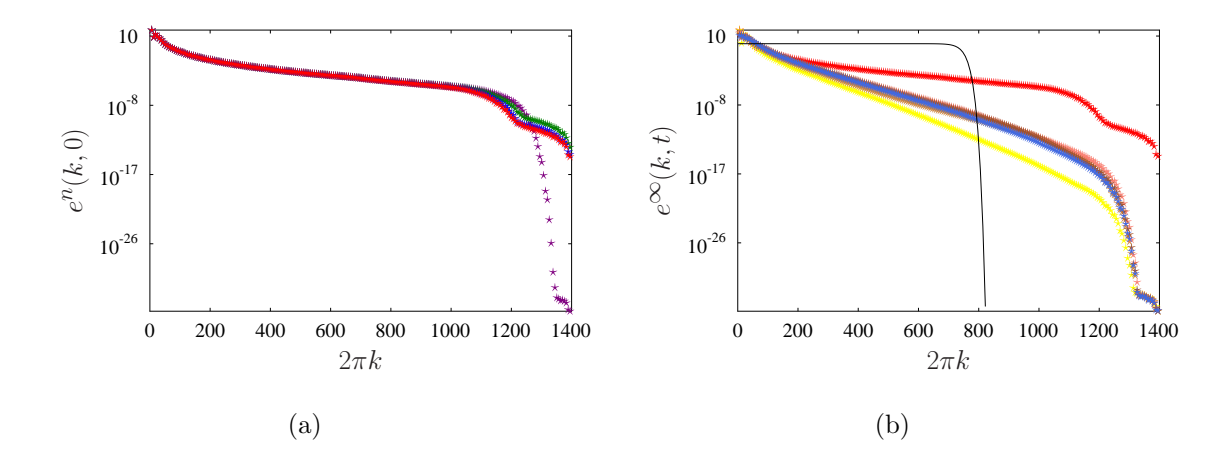


Figure 5.17:  $[q = 5, \text{ Problem 2}, B = 1500.2, T = 6 \times 10^{-4}]$  (a) Energy spectra of the approximations of the optimal initial condition obtained at different iterations n in the solution of Problem 2. (b) Energy spectra  $e^{\infty}(k,t)$  during the time evolution of the solution of the Navier-Stokes system (1.1) corresponding to the optimal initial condition  $\tilde{\mathbf{u}}_0$  (represented by red symbols). The time instances indicated in panel 5.17(b) are (red) t = 0, (yellow)  $t = 1.2 \times 10^{-4}$ , (brick)  $t = 2.4 \times 10^{-4}$ , (coral)  $t = 3.6 \times 10^{-4}$ , (brown)  $t = 4.8 \times 10^{-4}$ , and (blue)  $t = 6 \times 10^{-4}$ . Black line in panel 5.17(b) represents the filter (4.57).

Problems 1 and 2 with B=571, B=867 and B=1500.2, respectively. For each value of the constraint parameter B, the evolution of the norm of the solution of the Navier-Stokes system (1.1) is plotted for the shortest and longest time window T considered, except for B=1500.2 where the shortest considered time window was too small to plot. In this case, we decided to present the results for  $T=5\times 10^{-5}$ . We observe that  $\|\mathbf{u}(t)\|_{L^5}$  attains its maximum earlier in time when we use the optimal initial conditions found by solving Problem 1. These maxima are also characterized by larger values of the objective functional (3.1) than in the ones found by solving Problem 2. This mirrors the behavior of  $\|\mathbf{u}(t)\|_{L^4}$  which was discussed earlier, cf. Figure 5.4.

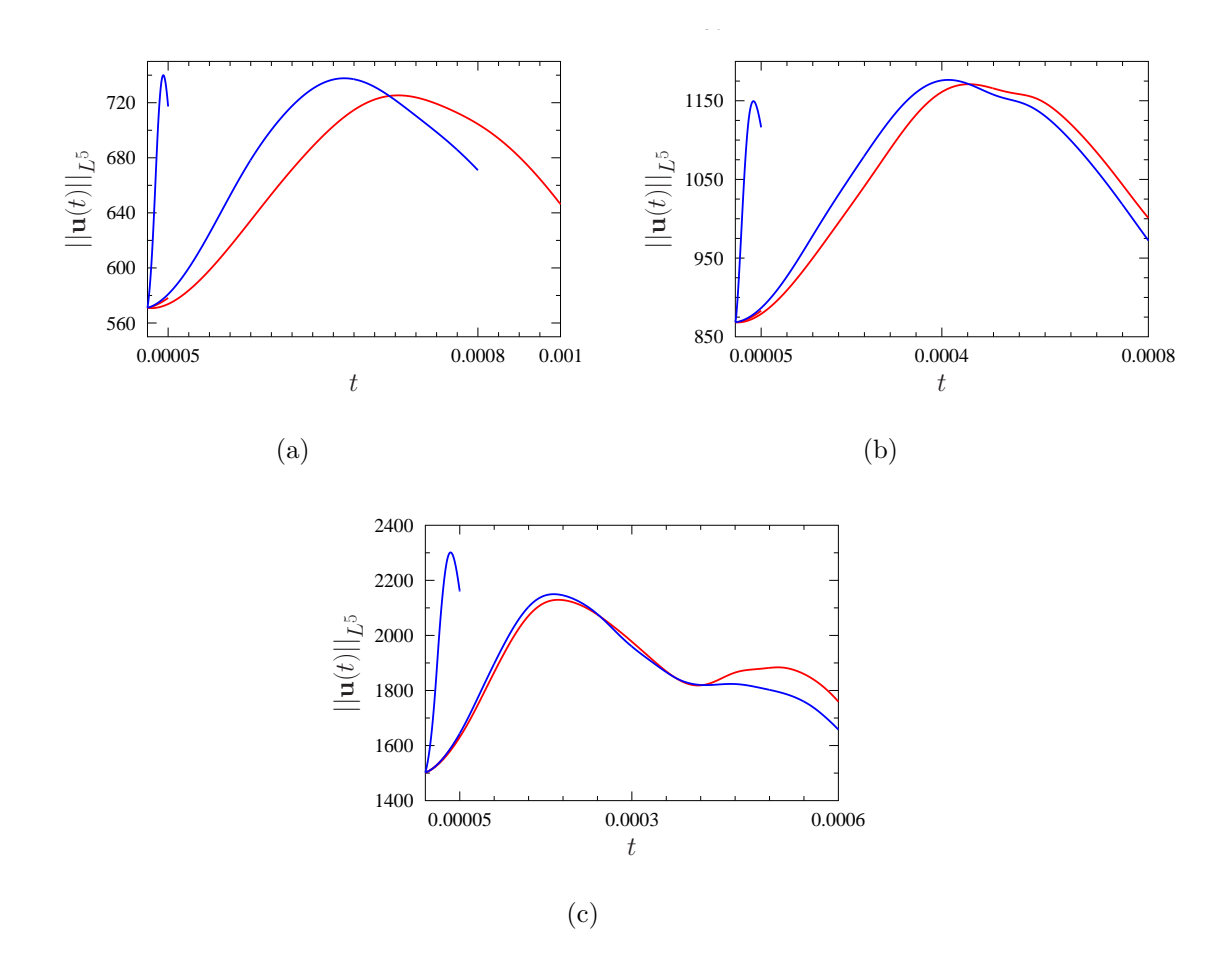


Figure 5.18: [q=5] Time evolution of  $||\mathbf{u}(t)||_{L^5}$  for Navier-Stokes flows with optimal initial conditions obtained by solving Problem 1 (blue) and Problem 2 (red). The values of the constraint parameter are (a) B=571, (b) B=867 and (c) B=1500.2. Solutions are computed over the time window [0,T] where T was chosen to be the shortest and longest considered time window, except for the last case where  $T=5\times 10^{-5}$  was chosen.

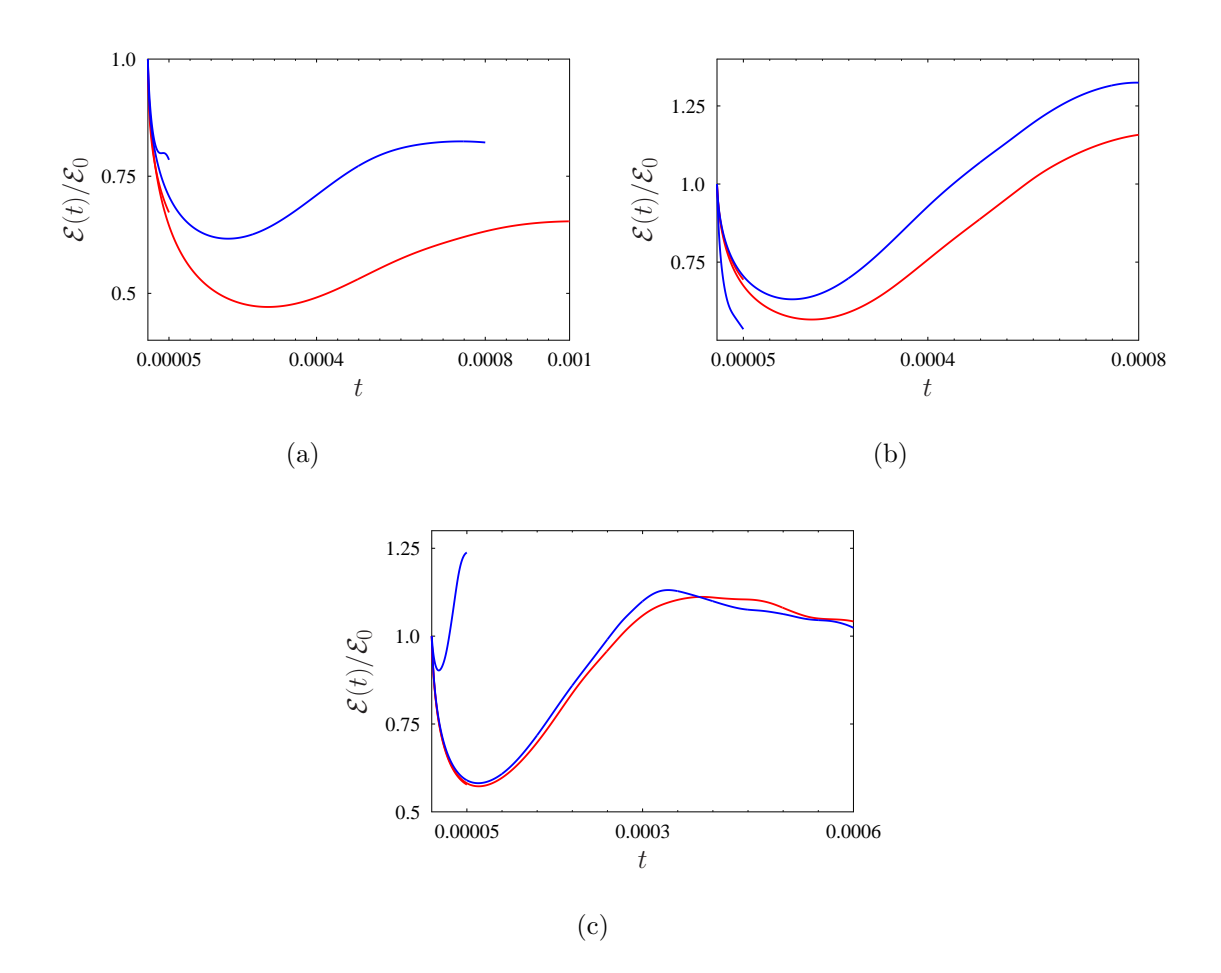


Figure 5.19: [q=5] Time evolution of the total enstrophy  $\mathcal{E}(\mathbf{u}(t))$  normalized with respect to the initial enstrophy  $\mathcal{E}_0$  in the solutions of the Navier-Stokes system (1.1) corresponding to the optimal initial conditions obtained by solving Problem 1 (blue) and Problem 2 (red). The values of the constraint parameter are (a) B=571, (b) B=867 and (c) B=1500.2. Solutions are computed over the time window [0,T] where T was chosen to be the shortest and longest considered time window, except for the last case where  $T=5\times 10^{-5}$  was chosen.

The evolution of the enstrophy  $\mathcal{E}(t)$  normalized with respect to the initial enstrophy  $\mathcal{E}_0$  is displayed in Figure 5.19. Values of the parameters B, T, as well as the color coding are the same as in Figure 5.18. We observe that the enstrophy initially decays but then

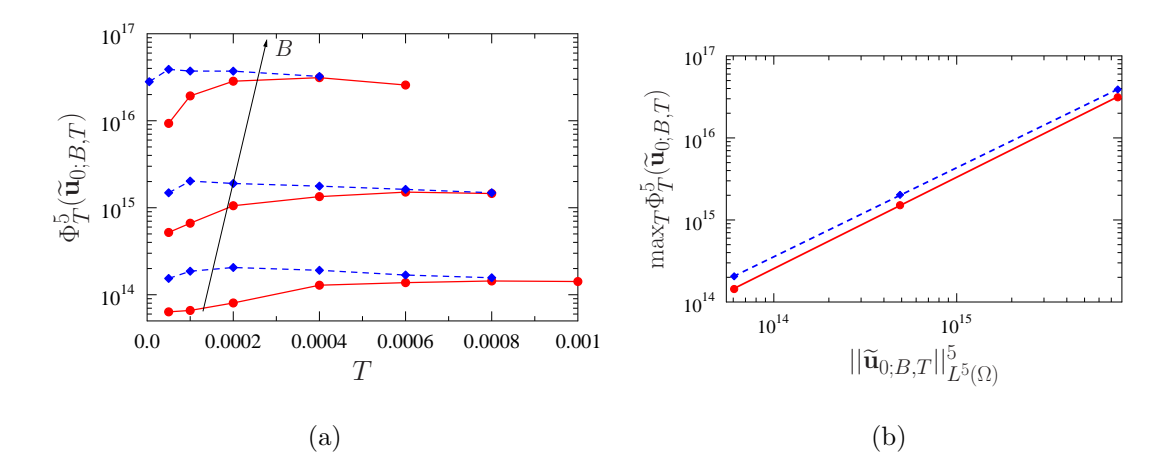


Figure 5.20: [q=5] (a) Dependence of the local maxima of the objective functional (3.1) with q=5 on the length of the optimization window in Problems 1 (blue) and 2 (red) for different values of the constraint B=571, B=867 and B=1500.2. Dashed and solid lines represent the nonsymmetric and symmetric branches, respectively, whereas the arrow indicates the trend with the increase of B. (b) Dependence of  $\max_T \Phi_T^5(\tilde{\mathbf{u}}_{0;B,T})$  on  $B^5=||\tilde{\mathbf{u}}_{0;B,T}||_{L^5(\Omega)}^5$ .

grows, and the growth seems more prominent as the parameter B increases.

### 5.2.1 Branches of Local Maximizers

In Figure 5.20(a) we show the dependance of the objective functional (3.1) on the length of the optimization window T for different values of the constraint B. In analogy with what was observed in the case with q = 4, we note that:

- i. Maximum values of the objective functional (3.1) obtained by solving Problem 1, with optimization performed over the Sobolev space  $H^{9/10}$ , are larger than in Problem 2, where optimization is performed over the Lebesgue space  $L^5(\Omega)$ .
- ii. The flows corresponding to the solutions of Problem 1 are again nonsymmetric.

- iii. The branches reveal the presence of a single maximum which shifts towards smaller values of T as the value of the constraint parameter B increases.
- iv. Nonsymmetric solutions produce larger values of the objective functional.

The relation between the maximum value of the objective functional over each branch and the value of the constraint parameter  $B^5$  is presented in the Figure 5.20(b). By performing least-square fits, we obtain the following power-law relations describing this dependence

$$\max_{T} \Phi_{T}^{5} \left( \widetilde{\mathbf{u}}_{0;B,T} \right) \sim 0.224 \left( ||\widetilde{\mathbf{u}}_{0;B,T}||_{L^{5}(\Omega)}^{5} \right)^{1.085}$$
(5.7)

for solutions of Problem 1 and

$$\max_{T} \Phi_{T}^{5} \left( \widetilde{\mathbf{u}}_{0;B,T} \right) \sim 0.064 \left( ||\widetilde{\mathbf{u}}_{0;B,T}||_{L^{5}(\Omega)}^{5} \right)^{1.113}$$
(5.8)

for solutions of Problem 2. Since the exponents are so close to one, we conclude that the maximum values of the objective functional scale almost proportionately to  $B^5$ . This means that the growth of the maximum value of the objective functional decreases by half of the growth of the same quantity when q = 4.

Figures 5.21(a) and 5.21(b) show the quantity  $\frac{d}{dt} ||\mathbf{u}(t)||_{L^5(\Omega)}$  as a function of  $||\mathbf{u}(t)||_{L^5(\Omega)}$  and  $d\mathcal{E}(t)/dt$  as a function of  $\mathcal{E}(t)$ , respectively. For a singularity formation to be possible, we would need to observe trajectories in which the rate of growth of the enstrophy and of the  $L^5(\Omega)$  norm of the velocity field remains higher than the rate represented by the dashed lines, which correspond to the minimum sustained growth rate necessary for a flow to potentially develop a singularity. In this case, several such trajectories are indeed observed, especially in Figure 5.21(a). However, this growth rate does not persist long enough for a blow-up to occur and we eventually observe a decline in the rate of change of the norm. We then arrive at a similar conclusion as in the case with q=4: although some solutions of the Navier-Stokes system (1.1) corresponding to optimal initial conditions obtained by solving Problems 1 and 2 do fall into the potential

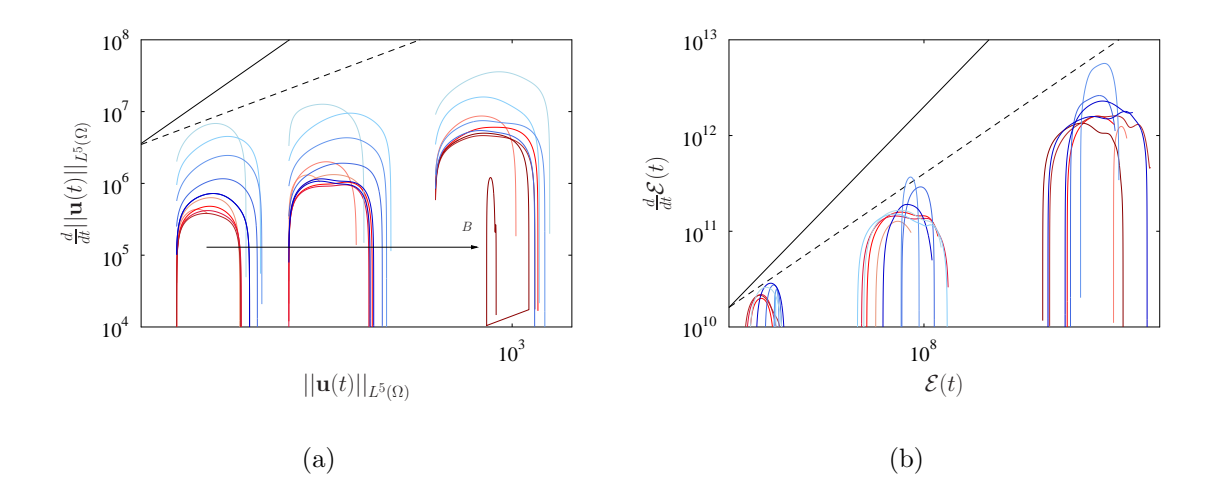


Figure 5.21: [q = 5] Navier-Stokes flows corresponding to the optimal initial conditions found by solving Problem 1 and 2 for different B and T shown using the coordinates (a)  $\{||\mathbf{u}(t)||_{L^5(\Omega)}, \frac{d}{dt}||\mathbf{u}(t)||_{L^5(\Omega)}\}$  and (b)  $\{\mathcal{E}(t), d\mathcal{E}(t)/dt\}$ . Black solid lines show the upper bounds in the rate of change of the  $L^5(\Omega)$  norm of the solution and the enstrophy given by the relations (a)  $\frac{d}{dt}||\mathbf{u}(t)||_{L^5(\Omega)} \sim ||\mathbf{u}(t)||_{L^5(\Omega)}^6$  from (2.31) and (b)  $d\mathcal{E}/dt \sim \mathcal{E}^3$ , respectively. Dashed lines show the relations (a)  $\frac{d}{dt}||\mathbf{u}(t)||_{L^5(\Omega)} \sim ||\mathbf{u}(t)||_{L^5(\Omega)}^{29/9}$  from (2.37) and (b)  $d\mathcal{E}/dt \sim \mathcal{E}^2$ . Blue trajectories are solutions of Problem 1 while red trajectories are solutions of Problem 2. The intensity of the color is related to the length of the time window with darker colors correspond to solutions with longer time windows T.

blow-up regime, the growth rate of the  $L^5(\Omega)$  norm is not sustained long enough to induce a singularity.

#### 5.2.2 Structure of the Extremal Flows

We will now discuss the structure of the extremal flows belonging to the different branches shown in Figure 5.20(a). Figures 5.22 and 5.23 show the time evolution of the componentwise enstrophies (5.3) for different values of the constraint parameter B in

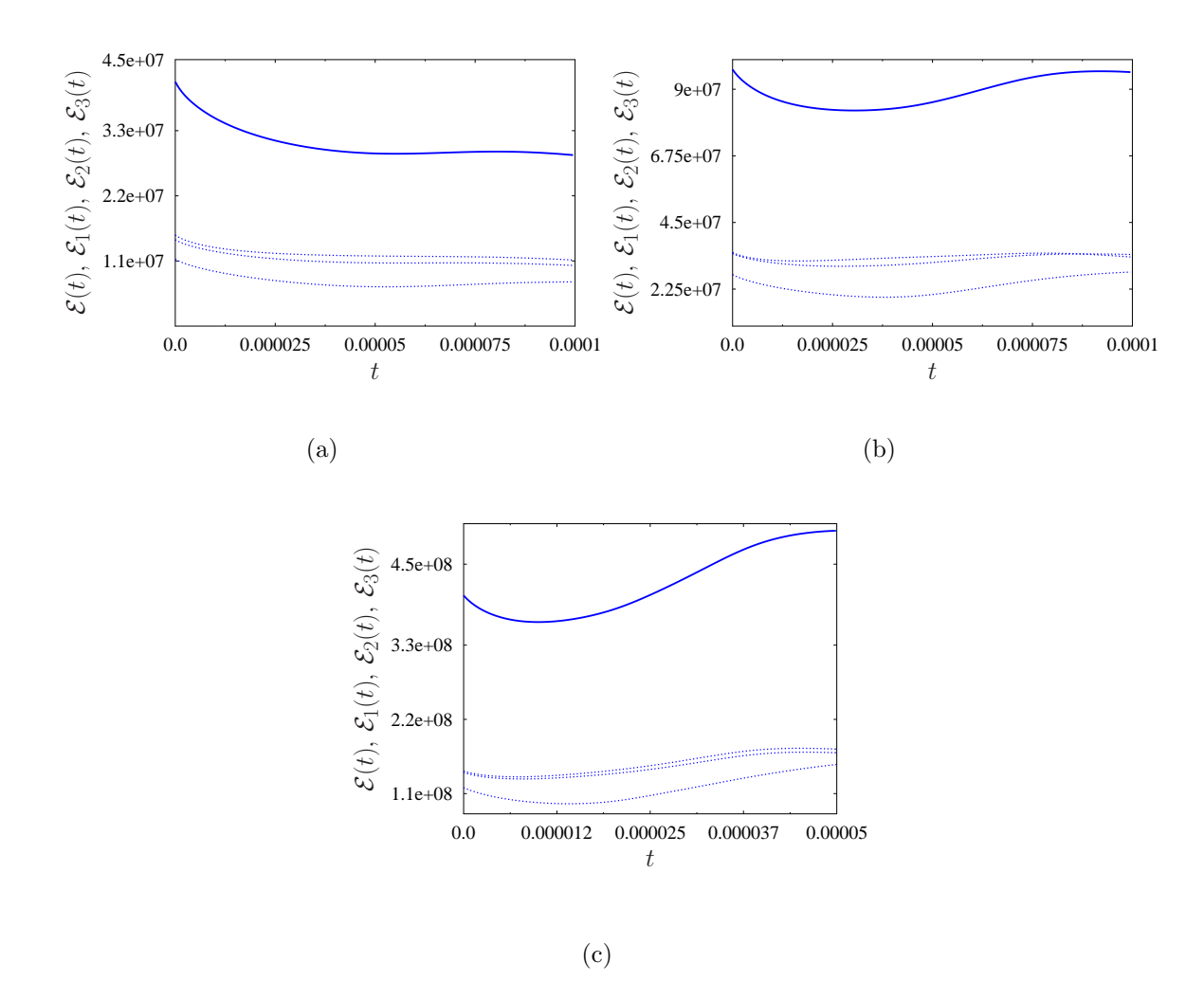


Figure 5.22: [q = 5, Problem 1, nonsymmetric flows] Evolution of (solid lines) the total enstrophy  $\mathcal{E}(t)$  and (dotted lines) the componentwise enstrophies  $\mathcal{E}_1(t)$ ,  $\mathcal{E}_2(t)$  and  $\mathcal{E}_3(t)$  for optimal solutions of Problem 2. The values of the parameters are (a) B = 571,  $T = 10^{-4}$  (b) B = 867,  $T = 10^{-4}$  and (c) B = 1500.2,  $T = 5 \times 10^{-5}$ .

solutions of Problem 1 and 2, respectively. The time window in each panel corresponds to the value of T for which the objective functional reaches its maximum on each branch. Here, we observe a similar behavior to what we saw in the case with q=4. Solutions of Problem 1 produce nonsymmetric flow evolutions, while solutions to Problem 2 yield

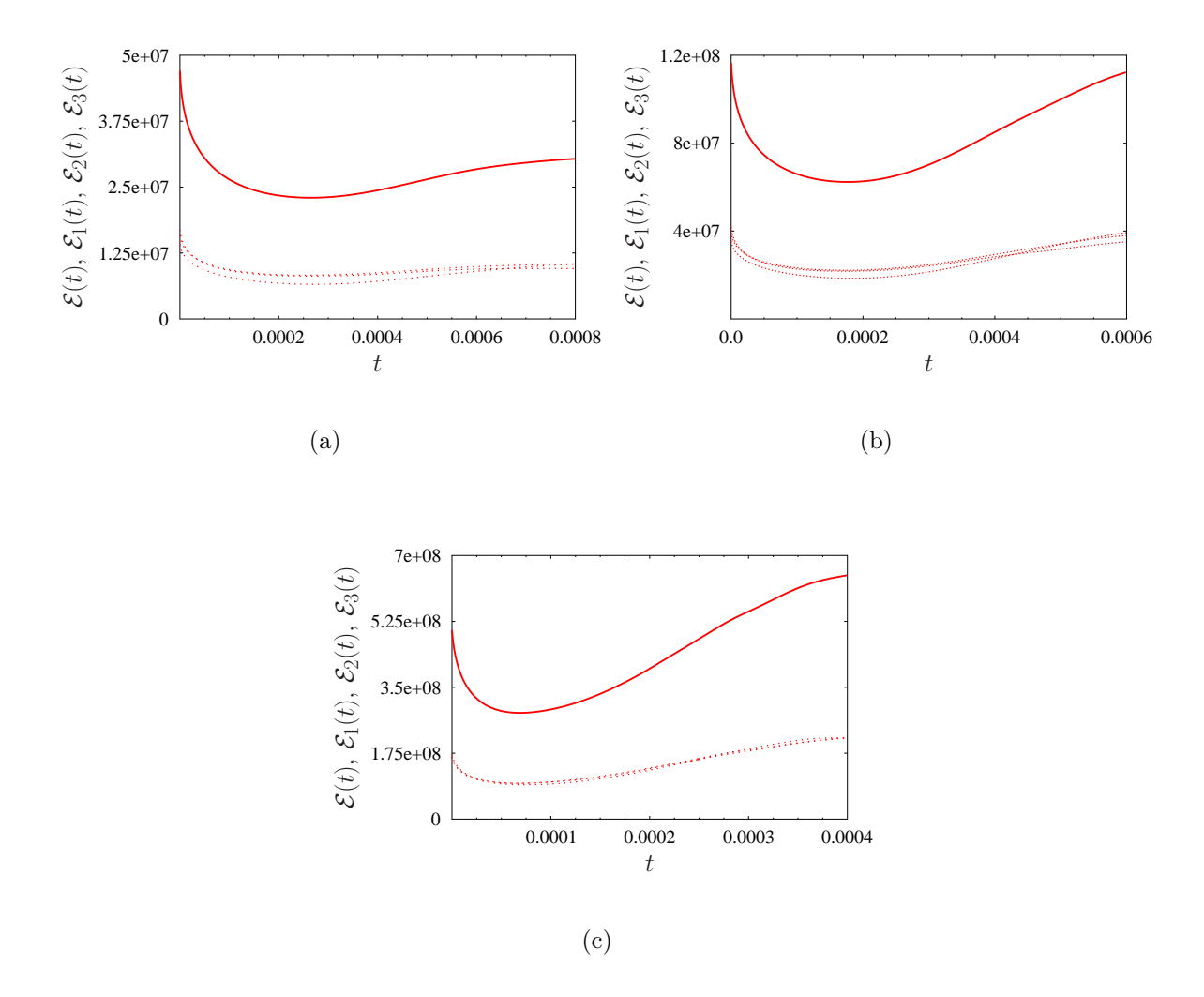


Figure 5.23: [q=5, Problem 2, symmetric flows] Evolution of (solid lines) the total enstrophy  $\mathcal{E}(t)$  and (dotted lines) the componentwise enstrophies  $\mathcal{E}_1(t)$ ,  $\mathcal{E}_2(t)$  and  $\mathcal{E}_3(t)$  for optimal solutions of Problem 1. The values of the parameters are (a) B=571,  $T=8\times 10^{-4}$  (b) B=867,  $T=6\times 10^{-4}$  and (c) B=1500.2,  $T=4\times 10^{-4}$ .

symmetric flow evolutions. Additionally, as the parameter B, increases, we observe, as expected, that the total enstrophy tends to grow more rapidly.

Below we visualize flow fields focusing on their velocity  $\mathbf{u}(\mathbf{x},t)$  and vorticity  $\boldsymbol{\omega}(\mathbf{x},t)$ . More specifically, we will show the magnitude of the vorticity  $|\boldsymbol{\omega}(\mathbf{x},t_i)|$  at different time

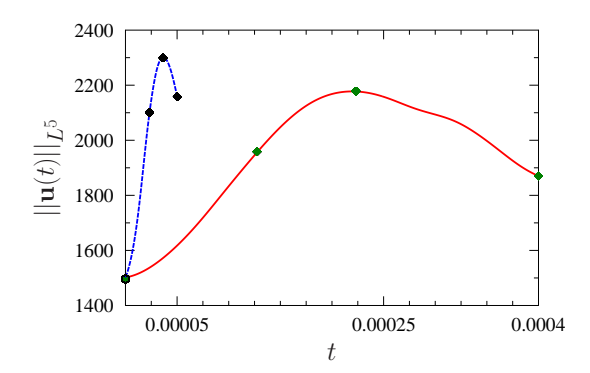


Figure 5.24: [q = 5, B = 1500.2] Time evolution of the norm  $\|\mathbf{u}(t)\|_{L^5}^5$  in the flow with the optimal initial condition that produces the maximum value of the objective functional for the largest value of the constraint in Problem 1 (blue) and Problem 2 (red). Black and green symbols represent the time instances  $t_i$ , i = 0, ..., 3, in Definition 5.1, when the flow is visualized in Figures 5.26 and 5.25.

instances  $t_i$  with i=0,...,3, together with  $|\mathbf{u}(\mathbf{x},t_i)|^5$  with  $t_i$  as in Definition 5.1. We marked these time instances with green and black symbols in Figure 5.24. The choice of the parameters B and T in Figures 5.25 and 5.26 corresponds to the maximum value of the objective functional (3.1) along the branch associated with the largest value of the constraint B. The flow structures shown in Figure 5.26 are quite similar to what we found for the case with q=4, featuring two tightly spaced vortex tubes which stretch to fill the entire flow domain, i.e., see Figure 5.13. However, we observe a different behavior at the final time  $t_3$ , where the vortex tubes appear to break up and become entangled to form a complicated flow pattern. Turbulent snapshots like this one were not observed for q=4. As for the flow structure in Figure 5.25, the time evolution of the vorticity seems to be less turbulent. We observe two closely spaced vortex tubes that stretch as time evolves. This time, however, they do not fill the entire domain. A possible explanation for the chaotic final stage evident in Figure 5.26, as opposed to the one in Figure 5.25, could be related to the function space in which the initial conditions are obtained. The fact that initial conditions obtained by solving Problem 1 possess

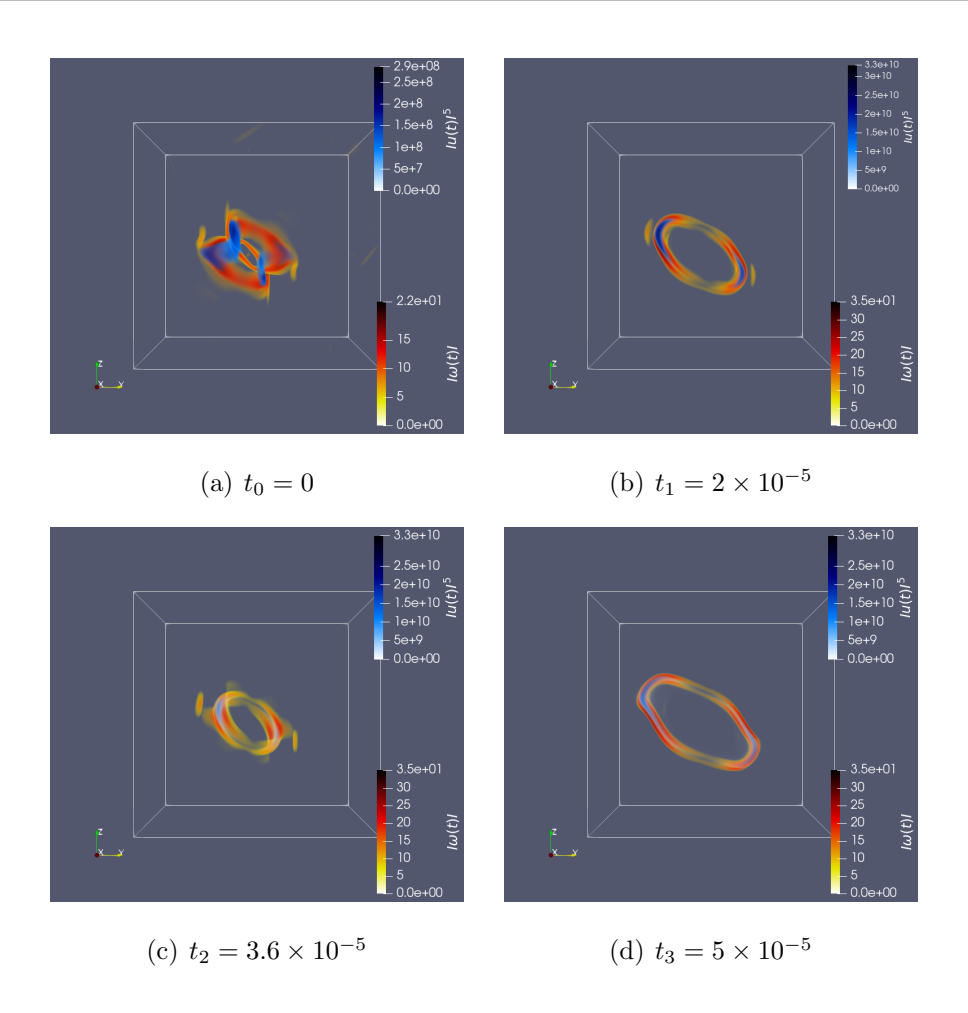


Figure 5.25:  $[q = 5, Problem 1, B = 1500.2 \text{ and } T = 5 \times 10^{-5}]$  Snapshots of the magnitude of the vorticity  $|\boldsymbol{\omega}(\mathbf{x}, t_i)|$  (red) in the solution of the Navier-Stokes system (1.1) and the quantity  $|\mathbf{u}(\mathbf{x}, t_i)|^5$  (blue) shown at the times  $t_0, ..., t_3$  defined in Definition 5.1. The values of the parameters B and T correspond to the maxima over the symmetric branch with the largest value of B in Figure 5.20(a).

certain degree of regularity may cause the time evolution of the vorticity to proceed more smoothly than when using initial conditions obtained by solving Problem 2.

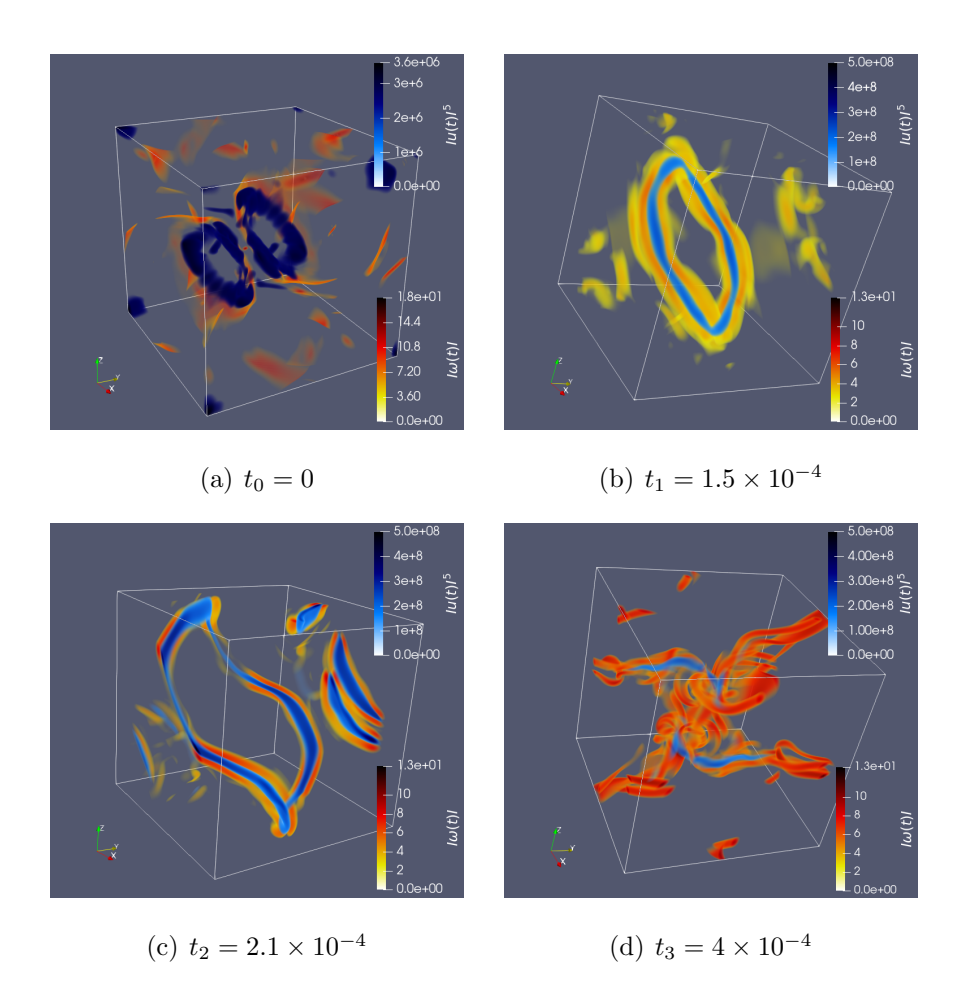


Figure 5.26:  $[q = 5, Problem 2, B = 1500.2 \text{ and } T = 4 \times 10^{-4}]$  Snapshots of the magnitude of the vorticity  $|\boldsymbol{\omega}(\mathbf{x}, t_i)|$  (red) in the solution of the Navier-Stokes system (1.1) and the quantity  $|\mathbf{u}(\mathbf{x}, t_i)|^5$  (blue) shown at the times  $t_0, ..., t_3$  defined in Definition 5.1. The values of the parameters B and T correspond to the maxima over the symmetric branch with the largest value of B in Figure 5.20(a).

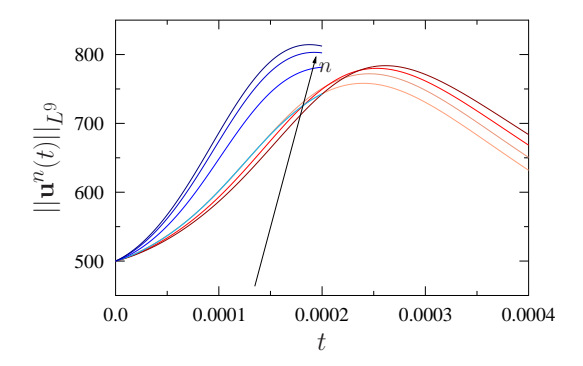


Figure 5.27: [q = 9, B = 500] Time evolution of the  $L^9(\Omega)$  norm of the velocity field at certain iterations n. Curves with darker colors correspond to later iterations closer to the local optimum of Problem 1 (blue) and Problem 2 (red). Blue and red curves correspond to optimization problems with  $T = 2 \times 10^{-4}$  and  $T = 4 \times 10^{-4}$ , respectively.

## 5.3 Extremal Flows in $L^9(\Omega)$

In this section, we consider q=9 and will vary the parameter T while keeping the parameter B fixed and equal to 500, 800 and 1200 (although some figures also use B=1037.92) in Problems 1 and 2.

Similarly as in the cases with q = 4 and q = 5, we did observe some increase of the norm  $\|\mathbf{u}(t)\|_{L^9}$ , though we did not find evidence for its unbounded growth that could signal singularity formation according to (2.30). In Figure 5.27, we see how the time evolution of the  $L^9(\Omega)$  norm of the velocity field changes with iterations as we approach the local maxima when solving Problems 1 and 2. The time window T is chosen such that it corresponds to the largest value of the objective functional obtained when solving Problems 1 and 2 for the given value of the constraint B = 500.

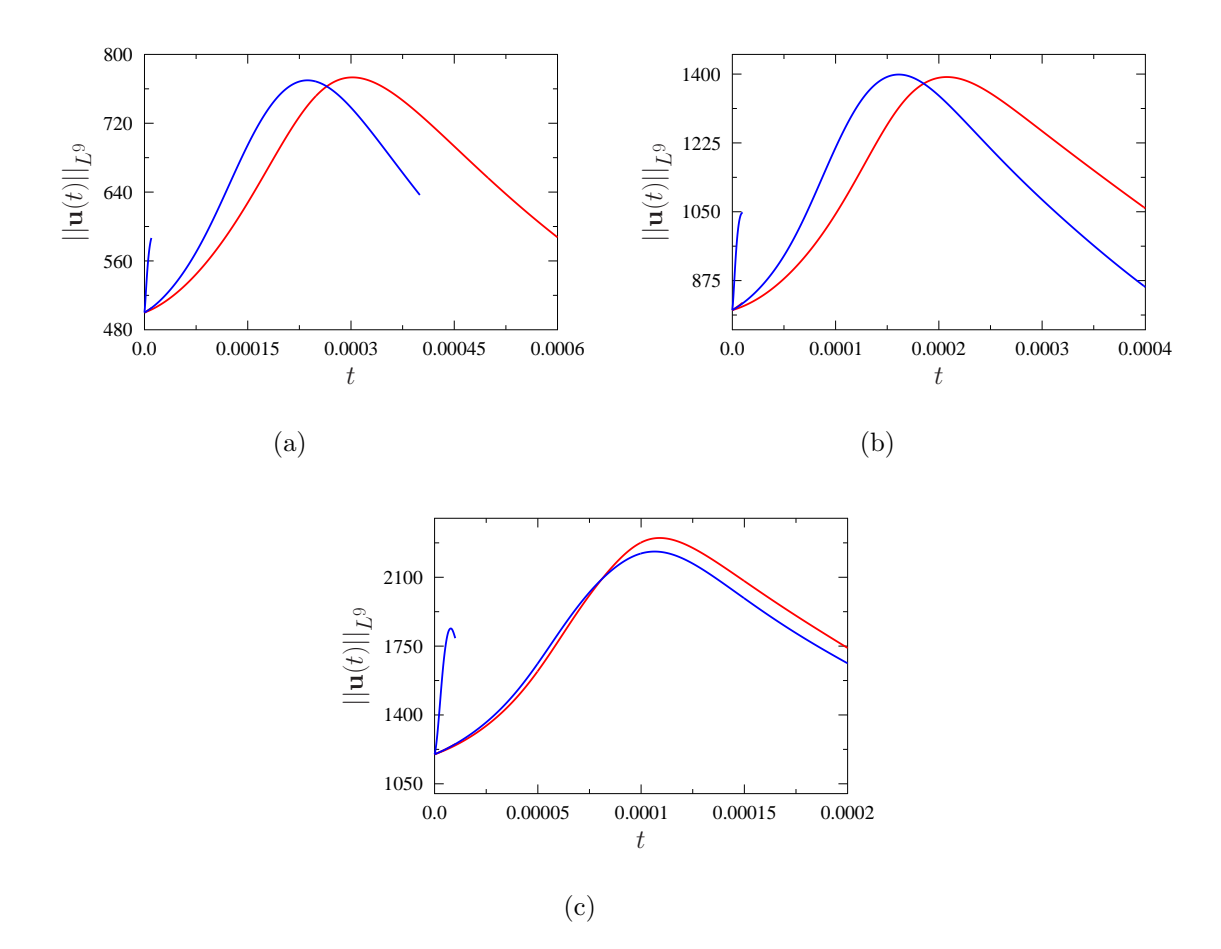


Figure 5.28: [q = 9] Time evolution of  $||\mathbf{u}(t)||_{L^9}$  for the Navier-Stokes flows with optimal initial conditions obtained by solving Problem 1 (blue) and Problem 2 (red). The values of the constraint parameter are (a) B = 500, (b) B = 800 and (c) B = 1200. Solutions are computed over the time window [0, T] where T was chosen to be the shortest and longest considered time window.

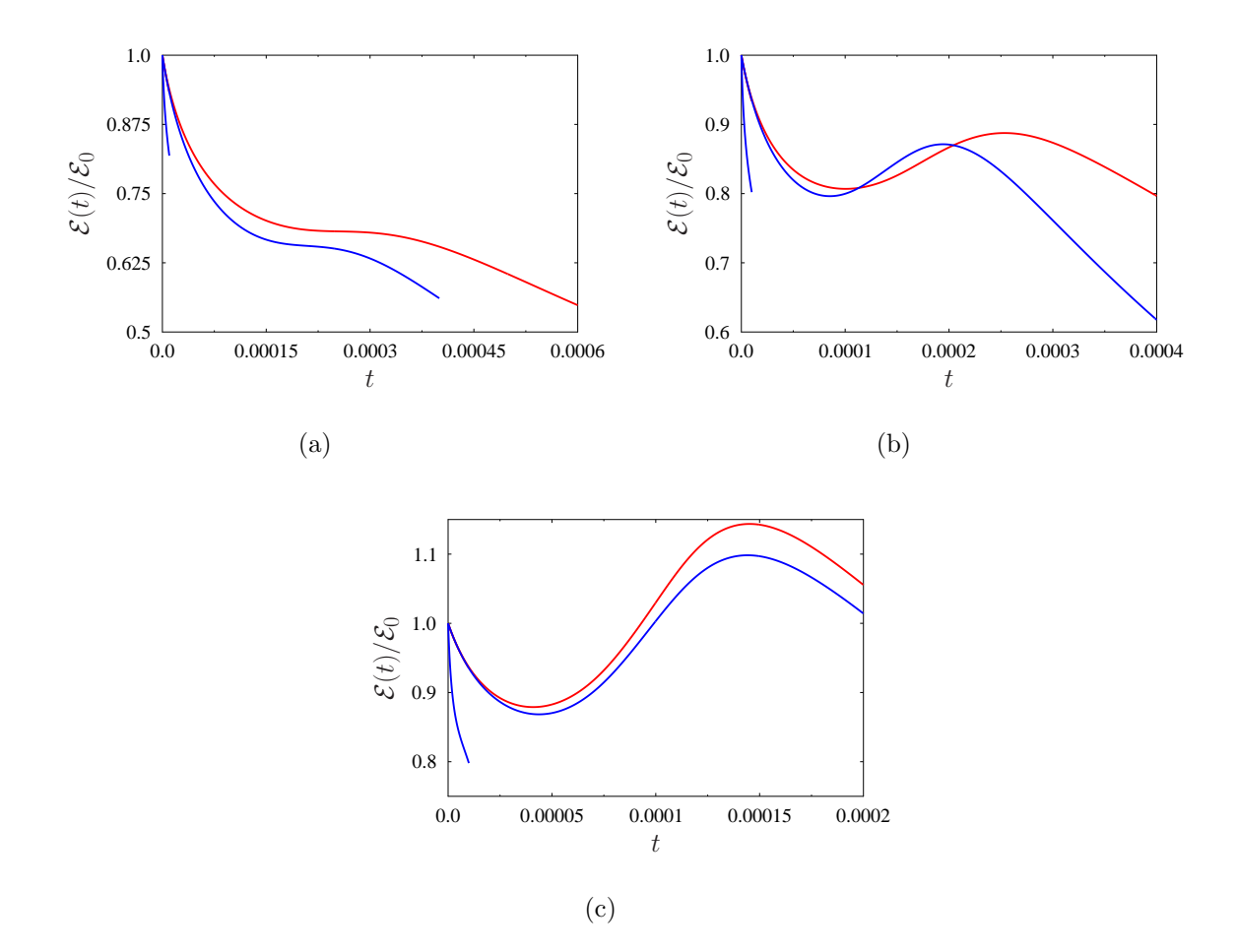


Figure 5.29: [q = 9] Time evolution of the total enstrophy  $\mathcal{E}(\mathbf{u}(t))$  normalized with respect to the initial entrophy  $\mathcal{E}_0$  in the solutions of the Navier-Stokes system (1.1) corresponding to the optimal initial conditions obtained by solving Problem 1 (blue) and Problem 2 (red). The values of the constraint parameter are (a) B = 500, (b) B = 800 and (c) B = 1200. Solutions are computed over the time window [0, T] where T was chosen to be the shortest and longest considered time window.

In Figures 5.28(a)–(c), we show the time evolution of the  $L^9(\Omega)$  norm of the solution of the Navier-Stokes system (1.1), using the optimal initial conditions found by solving Problems 1 and 2 with B=500, B=800 and B=1200.

For each value of the constraint parameter B, the evolution of the norm of the so-

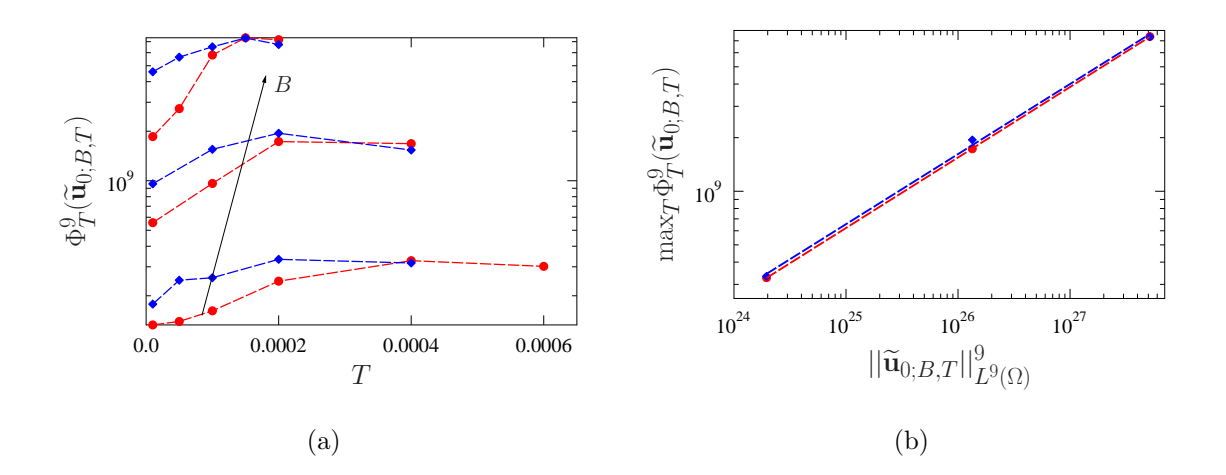


Figure 5.30: [q = 9] (a) Dependence of the local maxima of the objective functional (3.1) with q = 9 on the length of the optimization window in Problems 1 (blue) and 2 (red) for different values of the constraint B = 500, 800, 1200. The arrow indicates the trend with the increase of B. (b) Dependence of  $\max_T \Phi_T^9(\tilde{\mathbf{u}}_{0;B,T})$  on  $B^9 = ||\tilde{\mathbf{u}}_{0;B,T}||_{L^9(\Omega)}^9$ .

lution of the Navier-Stokes system (1.1) is plotted for the shortest and longest time window T considered. We observe that the maxima of  $\|\mathbf{u}(t)\|_{L^9}$  are generally larger when we use the optimal initial conditions found by solving Problem 1 than the optimal initial conditions from Problem 2. This mirrors the behavior of the norm when the optimal solutions were found in the spaces  $L^4(\Omega)$  and  $L^5(\Omega)$ , as discussed earlier, cf. Figures 5.4 and 5.18. The time evolution of the enstrophy  $\mathcal{E}(t)$  normalized with respect to the initial enstrophy  $\mathcal{E}_0$  is displayed in Figure 5.29. Values of the parameters B, T, as well as the color coding are the same as in Figure 5.28. We observed that the enstrophy initially decays and then grows, and the growth seems more prominent as the parameter B increases. This is exactly what we observed in earlier cases, cf. Figures 5.5 and 5.19, where the enstrophy initially decreases, followed by substantial growth.

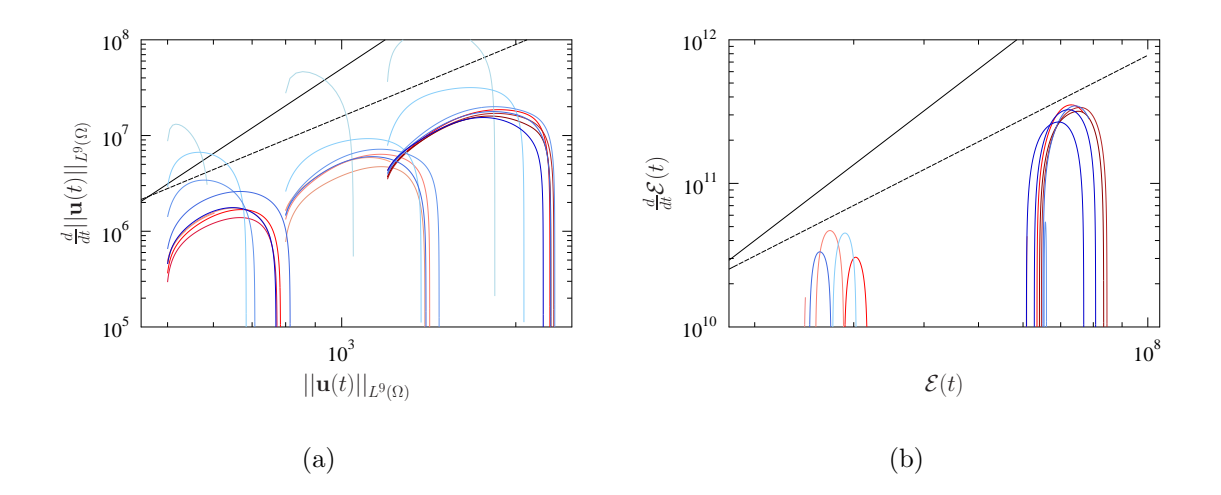


Figure 5.31: [q = 9] Navier-Stokes flows corresponding to the optimal initial conditions found by solving Problem 1 and 2 for different B and T shown using the coordinates (a)  $\{||\mathbf{u}(t)||_{L^9(\Omega)}, \frac{d}{dt}||\mathbf{u}(t)||_{L^9(\Omega)}\}$  and (b)  $\{\mathcal{E}(t), d\mathcal{E}(t)/dt\}$ . Black solid lines show the upper bounds in the rate of change of the  $L^9(\Omega)$  norm of the solution and the enstrophy given by the relations (a)  $\frac{d}{dt}||\mathbf{u}(t)||_{L^9(\Omega)} \sim ||\mathbf{u}(t)||_{L^9(\Omega)}^4$  from (2.31) and (b)  $d\mathcal{E}/dt \sim \mathcal{E}^3$ , respectively. Dashed lines show the relations (a)  $\frac{d}{dt}||\mathbf{u}(t)||_{L^9(\Omega)} \sim ||\mathbf{u}(t)||_{L^9(\Omega)}^{5/2}$  from (2.37) and (b)  $d\mathcal{E}/dt \sim \mathcal{E}^2$ . Blue trajectories are solutions of Problem 1 while red trajectories are solutions of Problem 2. The intensity of the color is related to the length of the time window with darker colors correspond to solutions with longer time windows T.

#### 5.3.1 Branches of Local Maximizers

In Figure 5.30(a) we show the dependance of the objective functional (3.1) on the length of the optimization window T for different values of the constraint B. Similarly to the observations made in the cases q = 4 and q = 5, we note that:

- i. The maximum of the objective functional (3.1) along the branch is generally higher when solving Problem 1 than when solving Problem 2.
- ii. The flows corresponding to the solutions of Problem 1 are again nonsymmetric.

iii. The branches reveal the presence of a single maximum.

The relation between the maximum value of the objective functional over each branch and the value of the constraint parameter  $B^9$  is presented in the Figure 5.30(b). By performing least-square fits, we obtain the following power-law relations describing this dependence

$$\max_{T} \Phi_{T}^{5} \left( \widetilde{\mathbf{u}}_{0;B,T} \right) \sim 0.09 \left( ||\widetilde{\mathbf{u}}_{0;B,T}||_{L^{9}(\Omega)}^{9} \right)^{0.3936}$$
(5.9)

for solutions of Problem 1 and

$$\max_{T} \Phi_{T}^{5} \left( \widetilde{\mathbf{u}}_{0;B,T} \right) \sim 0.07 \left( \left| \left| \widetilde{\mathbf{u}}_{0;B,T} \right| \right|_{L^{9}(\Omega)}^{9} \right)^{0.3958}$$
(5.10)

for solutions of Problem 2. When the exponents obtained are compared to their values in expressions (5.5), (5.6), (5.7) and (5.8), we observe that they are smaller than the exponents obtained for smaller values of q.

Figure 5.31 show the quantity  $\frac{d}{dt} ||\mathbf{u}(t)||_{L^9(\Omega)}$  as a function of  $||\mathbf{u}(t)||_{L^9(\Omega)}$  and  $d\mathcal{E}(t)/dt$  as a function of  $\mathcal{E}(t)$ , respectively. As mentioned before, we aim to observe trajectories in which the rate of growth of the enstrophy and of the  $L^9(\Omega)$  norm of the velocity field remains higher than the rate represented by the dashed lines, which is the lowest growth rate a trajectory must sustain if a singularity is to develop. In this case, a few such trajectories are observed, especially in Figure 5.31(a). However, similarly to what we saw before, their growth rate does not persist long enough for a blow-up to occur, and we eventually observe a decline in the rate of change of the norm. We then reach the same conclusion as in the cases with q=4 and q=5: although some solutions of the Navier-Stokes system (1.1) corresponding to optimal initial conditions obtained by solving Problems 1 and 2 do fall into the potential blow-up regime, the growth rate of the  $L^9(\Omega)$  norm is not sustained long enough for a singularity to develop.

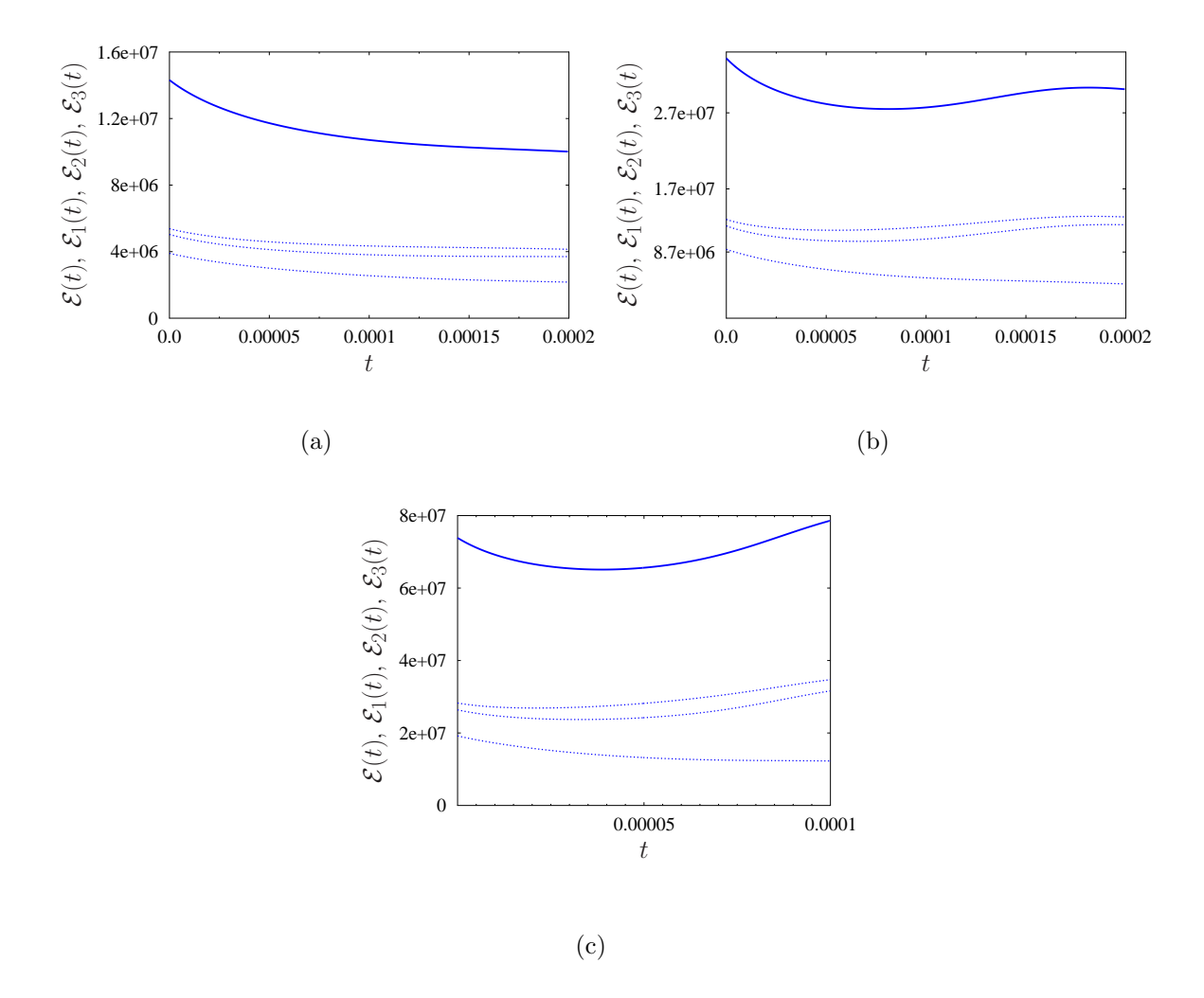


Figure 5.32: [q = 9, Problem 1] Evolution of (solid lines) the total enstrophy  $\mathcal{E}(t)$  and (dotted lines) the componentwise enstrophies  $\mathcal{E}_1(t)$ ,  $\mathcal{E}_2(t)$  and  $\mathcal{E}_3(t)$  for optimal solutions of Problem 1. The values of the parameters are (a) B = 500,  $T = 2 \times 10^{-4}$ , (b) B = 800,  $T = 2 \times 10^{-4}$ , and (c) B = 1200,  $T = 10^{-4}$ .

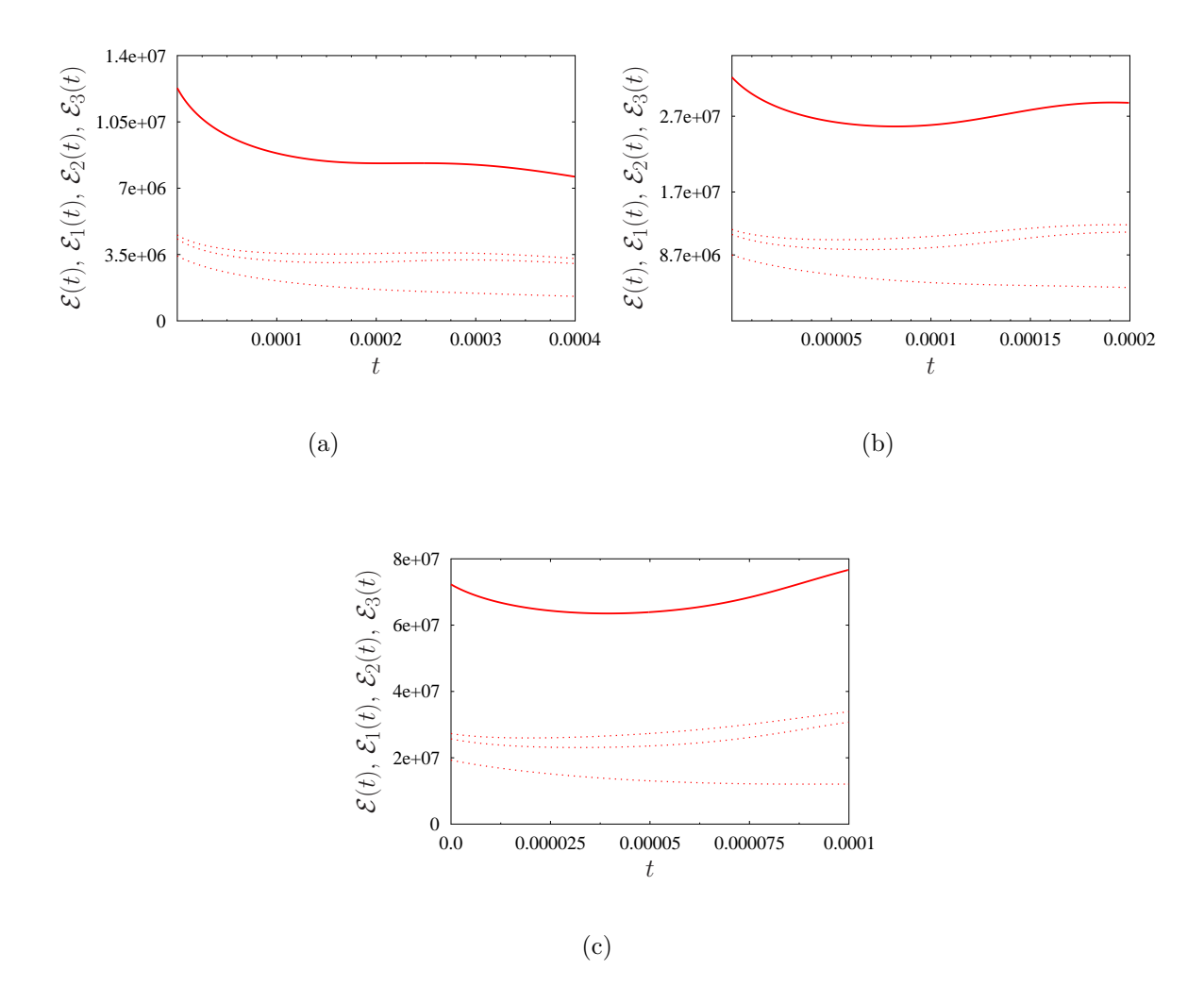


Figure 5.33: [q = 9, Problem 2] Evolution of (solid lines) the total enstrophy  $\mathcal{E}(t)$  and (dotted lines) the componentwise enstrophies  $\mathcal{E}_1(t)$ ,  $\mathcal{E}_2(t)$  and  $\mathcal{E}_3(t)$  for optimal solutions of Problem 2. The values of the parameters are (a) B = 500,  $T = 2 \times 10^{-4}$ , (b) B = 800,  $T = 2 \times 10^{-4}$ , and (c) B = 1200,  $T = 10^{-4}$ .

### 5.3.2 Structure of the Extremal Flows

Here, we discuss the structure of the extremal flows belonging to the different branches shown in Figure 5.30(a). Figures 5.32 and 5.33 show the time evolution of the com-

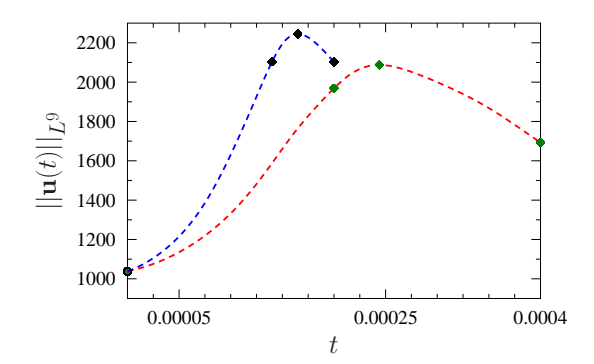


Figure 5.34: [q = 9, B = 1037.92] Time evolution of the norm  $\|\mathbf{u}(t)\|_{L^9}$  in the flow with the optimal initial condition that produces the maximum value of the objective functional in Problem 1 (blue) and Problem 2 (red). Black and green symbols represent the time instances  $t_i$ , i = 0, ..., 3, in Definition 5.1, when the flow is visualized in Figures 5.35 and 5.36.

ponentwise enstrophies (5.3) in solutions of Problem 1 and 2, respectively. The time window in each panel corresponds to the value of T for which the objective functional reaches its maximum on each branch. Unlike the case q = 5, solutions of Problem 1 and Problem 2 are both nonsymmetric. Unsurprisingly, we observe that the total enstrophy of solutions to Problems 1 and 2 initially decreases, followed by growth.

Below we visualize the flow fields focusing on their velocity  $\mathbf{u}(\mathbf{x},t)$  and vorticity  $\boldsymbol{\omega}(\mathbf{x},t)$ . More specifically, we will show the magnitude of the vorticity  $|\boldsymbol{\omega}(\mathbf{x},t_i)|$  at different time instances  $t_i$  with i=0,...,3, together with  $|\mathbf{u}(\mathbf{x},t_i)|^9$  where  $t_i$  is as in Definition 5.1. We marked these time instances as the green and black symbols in Figure 5.34. In Figure 5.35, the time evolution of the vorticity appears different from what we observed in the cases q=4 and q=5. Although we observe vortex tubes, they do not seem to close, unlike in the previous cases. As for the flow structure in Figure 5.36, they reveal similar features to what we saw for the case with q=4 and q=5, with two tightly spaced vortex rings which stretch to fill the entire flow domain, cf. Figure 5.13 and 5.26. This time, however, the rings seem to twist across the domain.

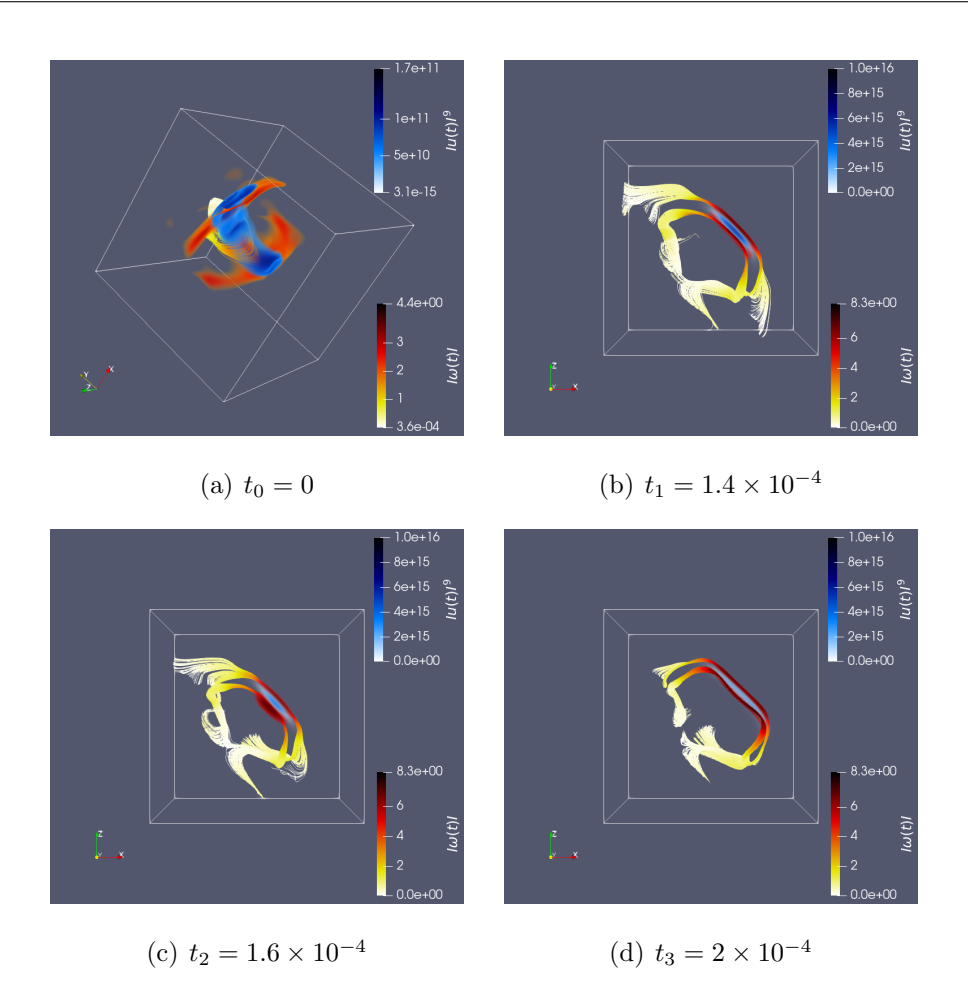


Figure 5.35:  $[q = 9, \text{ Problem 1}, B = 1037.92 \text{ and } T = 2 \times 10^{-4}]$  Snapshots of the magnitude of the vorticity  $|\boldsymbol{\omega}(\mathbf{x}, t_i)|$  (red) along with vortex lines (red) of the solution of the Navier-Stokes system (1.1) and the quantity  $|\mathbf{u}(\mathbf{x}, t_i)|^9$  (blue) shown at the times  $t_0, ..., t_3$  defined in Definition 5.1.

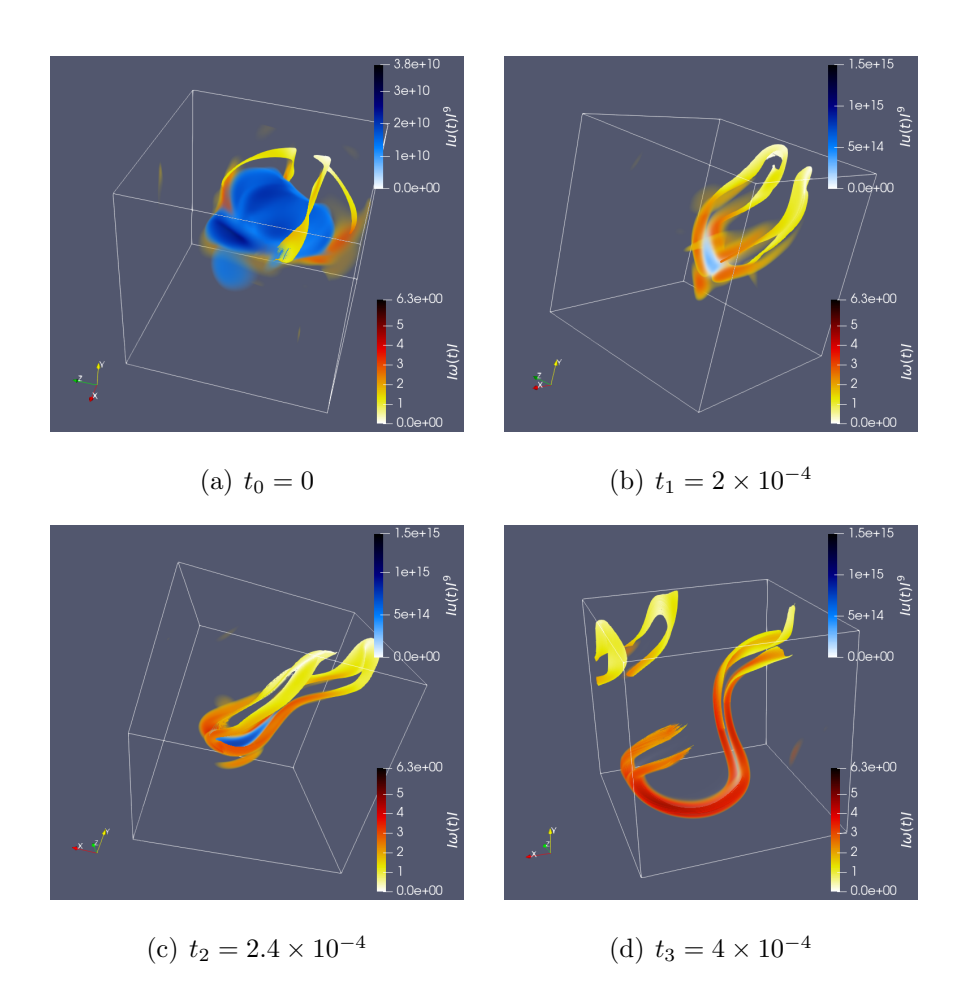


Figure 5.36:  $[q = 9, \text{ Problem 2}, B = 1037.92 \text{ and } T = 4 \times 10^{-4}]$  Snapshots of the magnitude of the vorticity  $|\boldsymbol{\omega}(\mathbf{x}, t_i)|$  (red) along with vortex lines (red) in the solution of the Navier-Stokes system (1.1) and the quantity  $|\mathbf{u}(\mathbf{x}, t_i)|^9$  (blue) shown at the times  $t_0, ..., t_3$  defined in Definition 5.1.

# **5.4** Extremal Flows in $L^3(\Omega)$

In this section, we consider the limiting case q=3 and vary the parameters B and T while solving Problems 3 and 4. As before, we found no evidence of unboundedness of the  $L^3(\Omega)$  norm of solutions to the Navier-Stokes system (1.1), which would indi-

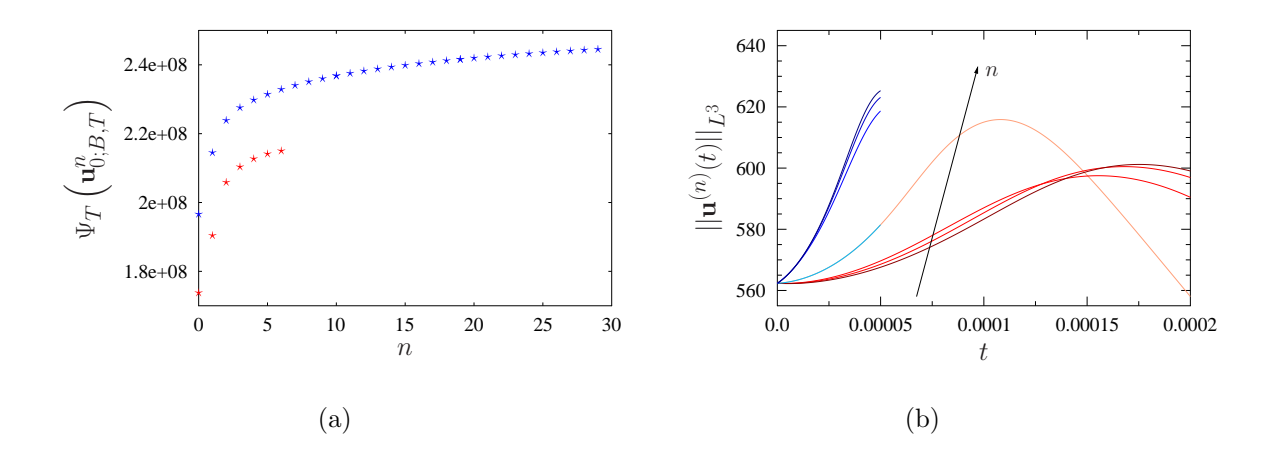


Figure 5.37: [q=3, B=562.34] (a) Dependence of the objective functional (3.9) on the iteration n when solving Problem 3 (blue) and Problem 4 (red). (b) Time evolution of the  $L^3(\Omega)$  norm of the velocity field at certain iterations n. Curves with darker colors correspond to later iterations closer to the local optimum of Problem 1 (blue) and Problem 2 (red). Blue and red curves correspond to optimization problems with  $T=5\times 10^{-5}$  and  $T=2\times 10^{-4}$ , respectively.

cate singularity formation according to (2.30). We should point out that the objective functional in this case (3.9) is different from the previous cases (3.1), and in the optimization problem, we aim to maximize the  $L^q(\Omega)$  norm at a terminal time t = T, rather than an integral of the norm over the entire time window [0,T]. Unlike the case of the other values of q considered in the previous sections, we found that the  $L^3(\Omega)$  norm of Navier-Stokes flows did not exhibit significant growth. For example, we can see in Figure 5.37(b) that the  $L^3(\Omega)$  norm at the optimal states grew less than 10%.

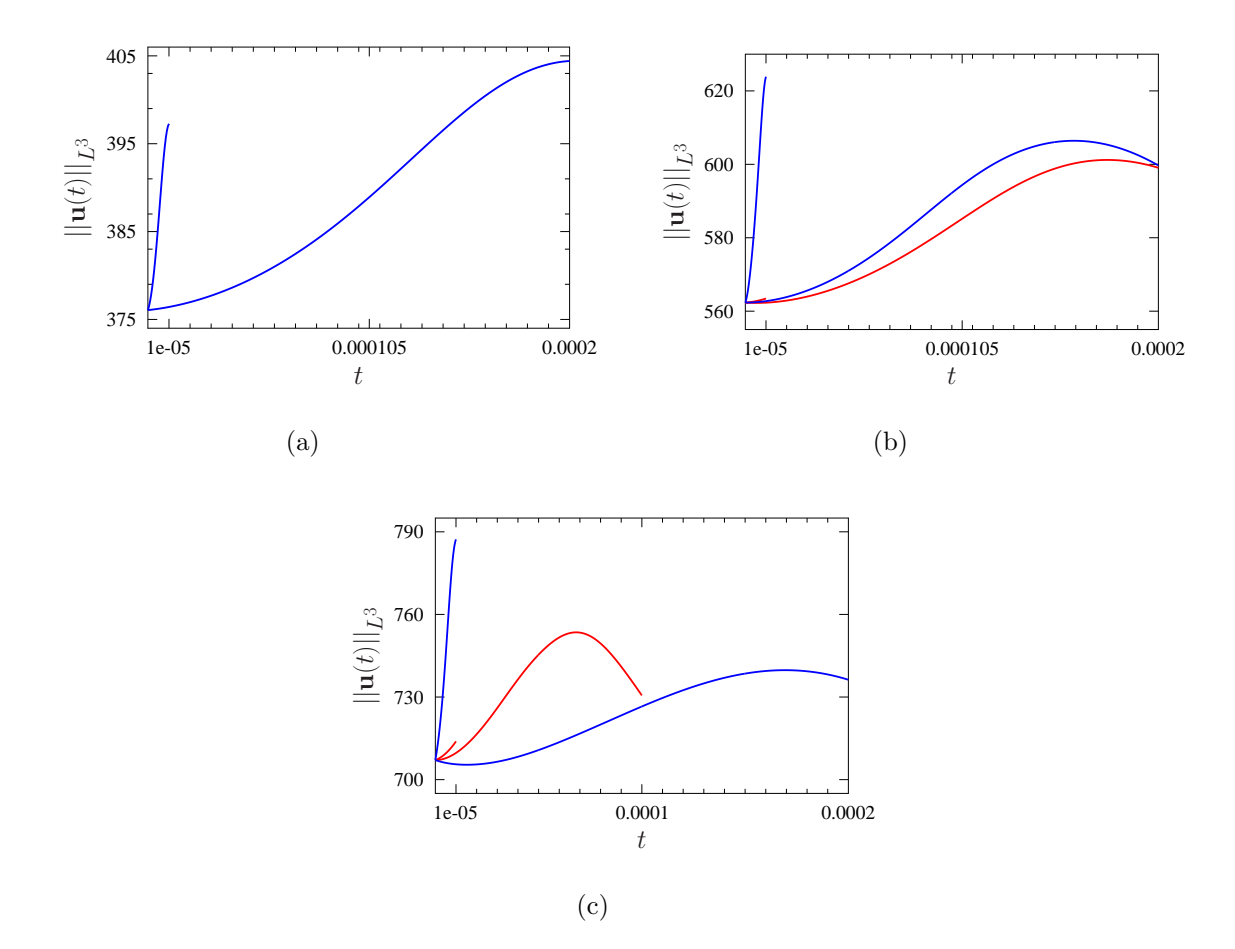


Figure 5.38: [q = 3] Time evolution of  $||\mathbf{u}(t)||_{L^3}$  in the Navier-Stokes flows with optimal initial conditions obtained by solving Problem 3 (blue) and Problem 4 (red). The values of the constraint parameter are (a) B = 376.06, (b) B = 562.34 and (c) B = 707.10. Solutions are computed over the time window [0,T] where T was chosen to be the shortest and longest considered time window.

This is unsurprising, since it is well know that the the  $L^3(\Omega)$  norm of Navier-Stokes flows grows at a slow rate [27].

In Figure 5.37(a), we observe the convergence of the objective functional (3.9) with iterations n when solving Problems 3 and 4. The constraint parameter B is fixed at 562.34, while the time window T was chosen as follows: for the solution to Problem 3,

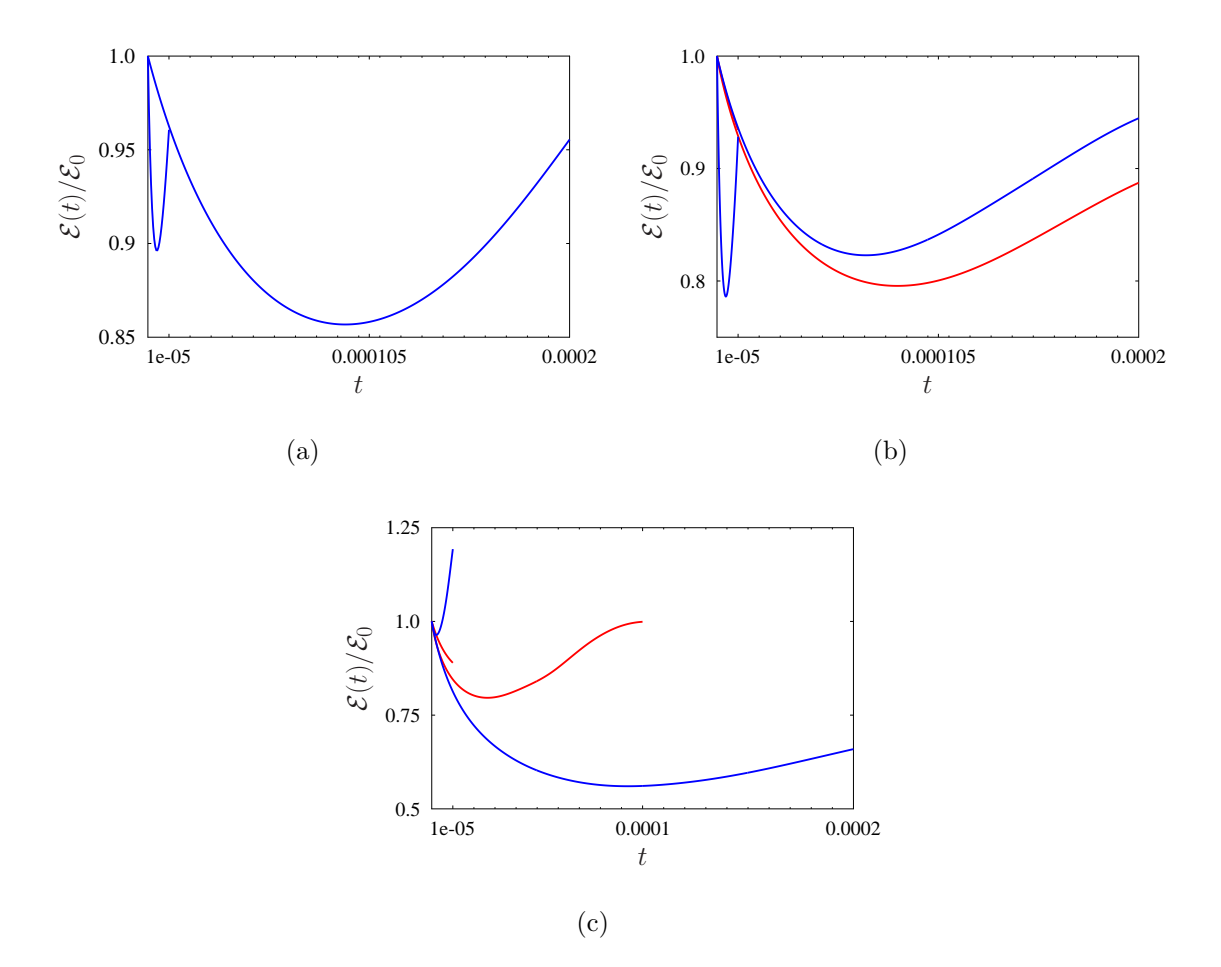


Figure 5.39: [q=3] Time evolution of the total enstrophy  $\mathcal{E}(\mathbf{u}(t))$  normalized with respect to the initial entrophy  $\mathcal{E}_0$  in the solutions of the Navier-Stokes system (1.1) corresponding to the optimal initial conditions obtanied by solving Problem 3 (blue) and Problem 4 (red). The values of the constraint parameter are (a) B=376.06, (b) B=562.34 and (c) B=707.10. Solutions are computed over the time window [0,T] where T was chosen to be the shortest and longest considered time window.

it maximizes the objective functional (3.9) along the middle branch in Figure 5.40(a), and for the solution to Problem 4, it corresponds to one of the values where more iterations were needed in (4.7).

In Figure 5.37(b), we see how the time evolution of the  $L^3(\Omega)$  norm of the velocity

field changes with iterations as we approach the local maxima. The evolution of the spectrum of the solution to the Navier-Stokes system (1.1) is not presented here, as it behaves in an analogous manner as in the cases q = 4 and q = 5, cf. see Figures 5.2, 5.3, 5.16, and 5.17.

In Figures 5.38 (a)–(c), we show the time evolution of the  $L^3(\Omega)$  norm of the solution to the Navier-Stokes system (1.1), using the optimal initial conditions found by solving Problems 3 and 4 with B=376.06, B=562.34 and B=707.10, respectively. For each value of the constraint parameter B, the evolution of its  $L^3(\Omega)$  norm is plotted for the shortest and longest time window considered T. We see that the maximum of  $\|\mathbf{u}(t)\|_{L^3(\Omega)}$  is typically larger when we use the optimal initial conditions found by solving Problem 3. This resembles the behavior we already observed in the cases with q>3 even though the objective functional here is different. The evolution of the enstrophy  $\mathcal{E}(t)$  normalized with respect to the initial enstrophy  $\mathcal{E}_0$  is displayed in Figure 5.39. The values of the parameters B, T, as well as the color coding is identical as in Figure 5.38. As in the previous cases, we observe that the enstrophy initially decays but then eventually grows. This time, however, larger values of the parameter B do not correspond to higher variation in the increasing section of the enstrophy.

#### 5.4.1 Branches of Local Maximizers

In Figure 5.40(a) we show the dependance of the objective functional (3.9) on the length of the optimization window T for different values of the constraint B. In solutions to Problems 3 and 4 flows on each branch exhibit similar behavior of the norm  $||\mathbf{u}(t)||_{L^3(\Omega)}$  in time as already shown in Figure 5.38. We observe that the maximum values of the objective functional (3.9) obtained by solving Problem 3, where the optimization is performed over the Sobolev space  $H^{1/2}$ , are larger than in Problem 4, where the optimization is performed over the Lebesgue space  $L^3(\Omega)$ . This behaviour is consistent with what was observed for the previous values of q, where solutions found in Sobolev

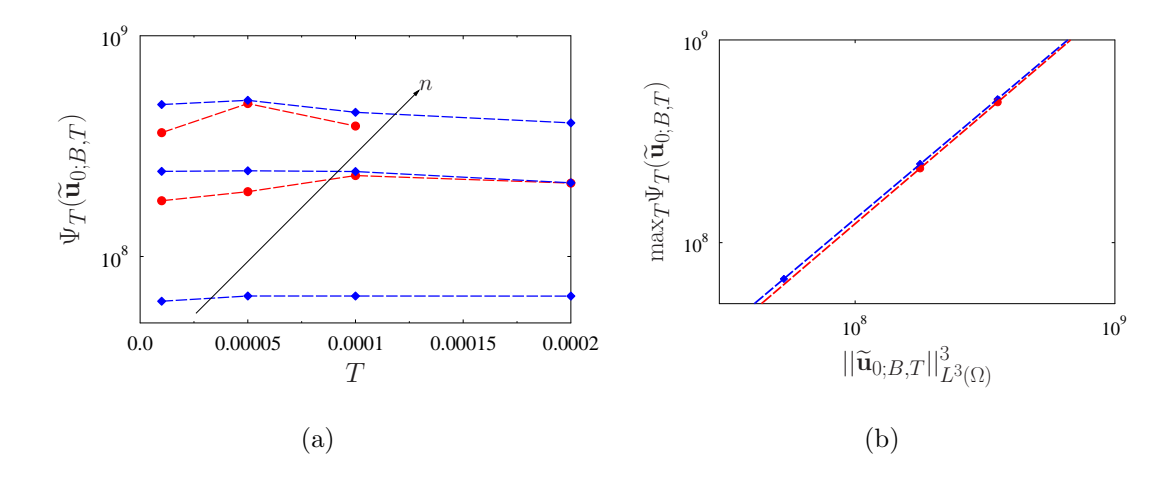


Figure 5.40: [q=3] (a) Dependence of the local maxima of the objective functional (3.1) with q=3 on the length of the optimization window in Problems 3 (blue) and 4 (red) for different values of the constraint B=376.06, B=562.34 and B=707.10. Dashed lines represent nonsymmetric branches, whereas the arrow indicates the trend with the increase of B. (b) Dependence of  $\max_T \Psi_T(\tilde{\mathbf{u}}_{0;B,T})$  on  $B^3 = ||\tilde{\mathbf{u}}_{0;B,T}||_{L^3(\Omega)}^3$ .

spaces produced larger values of the objective functional (3.1) than those over Lebesgue spaces. Furthermore, we found that the flows corresponding to the solutions of Problems 3 and 4 are always nonsymmetric. Interestingly, even though the solutions of Problems 3 and 4 preserve the same symmetry, solutions of Problem 3 continue to produce higher values of the objective functional (3.9). However, the difference between these maxima is small. Notice that all the branches reveal the presence of a single maximum which slightly shifts towards smaller values of T as the value of the constraint parameter B increases. The relation between the maximum value of the objective functional (3.9) along each branch and the value of the constraint parameter  $B^3$  is presented in the Figure 5.40(b). By performing least-square fits, we obtain the following power-law relations describing this dependence

$$\max_{T} \Psi_{T}(\tilde{\mathbf{u}}_{0;B,T}) \sim 0.31 \left( ||\tilde{\mathbf{u}}_{0;B,T}||_{L^{3}(\Omega)}^{3} \right)^{1.07}$$
(5.11)

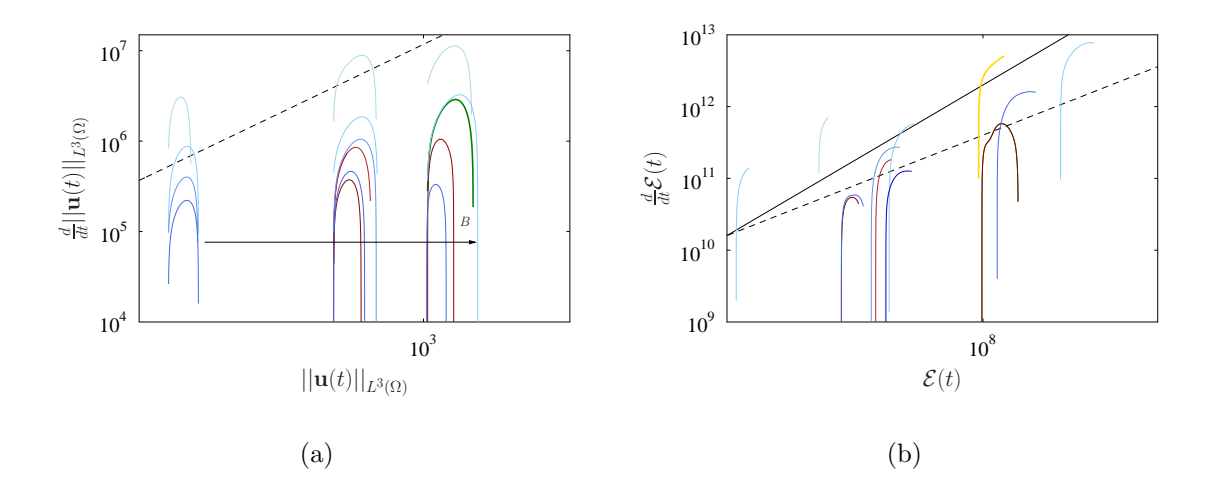


Figure 5.41: [q=3] Navier-Stokes flows corresponding to the optimal initial conditions found by solving Problem 3 and 4 for different B and T shown using the coordinates (a)  $\{||\mathbf{u}(t)||_{L^3(\Omega)}, \frac{d}{dt}||\mathbf{u}(t)||_{L^3(\Omega)}\}$  and (b)  $\{\mathcal{E}(t), d\mathcal{E}(t)/dt\}$ . Black solid line shows the upper bounds in the rate of change of the enstrophy given by the relation  $d\mathcal{E}/dt \sim \mathcal{E}^3$ . Panel (a) does not have a black solid line since an upper bound on the rate of growth of the  $L^3(\Omega)$  norm does not seem to be available. Dashed lines show the relations (a)  $\frac{d}{dt}||\mathbf{u}(t)||_{L^3(\Omega)} \sim ||\mathbf{u}(t)||_{L^3(\Omega)}^5$  from (2.37) and (b)  $d\mathcal{E}/dt \sim \mathcal{E}^2$ . Blue trajectories correspond to solutions of Problem 3 while red trajectories show solutions of Problem 4. The intensity of the color is related to the length of the time window with darker colors correspond to solutions with longer time windows T.

for solutions of Problem 3, and

$$\max_{T} \Psi_{T} \left( \widetilde{\mathbf{u}}_{0;B,T} \right) \sim 0.22 \left( ||\widetilde{\mathbf{u}}_{0;B,T}||_{L^{3}(\Omega)}^{3} \right)^{1.09}$$
(5.12)

for solutions of Problem 4. We can conclude that there appears to be a linear dependency between the maximum of the objective functional (3.9) and the constraint parameter  $B^3$ .

In Figure 5.41, we now plot the corresponding time-dependent trajectories using the coordinates  $\{||\mathbf{u}(t)||_{L^3(\Omega)}, \frac{d}{dt} ||\mathbf{u}(t)||_{L^3(\Omega)}\}$  and  $\{\mathcal{E}(t), d\mathcal{E}(t)/dt\}$ . As in Sections 5.1.1,

5.2.1 and 5.3.1, we aim to check whether or not there are trajectories in which the rate of growth of the enstrophy and the  $L^3(\Omega)$  norm of the velocity field remains higher, for a sufficient long time, than the rate represented by the dashed lines. Unlike the cases with q>3, in this limiting case we observe only a few trajectories that satisfy this condition, e.g., the green and the gold trajectories in Figures 5.31(a) and 5.31(b), respectively. These correspond to solutions of Problem 3 (Figure 5.31(b)) and Problem 4 (Figure 5.31(a)). However, their rate of growth does not persist long enough for a blow-up to occur and we eventually observe a decline in the rate of change of the

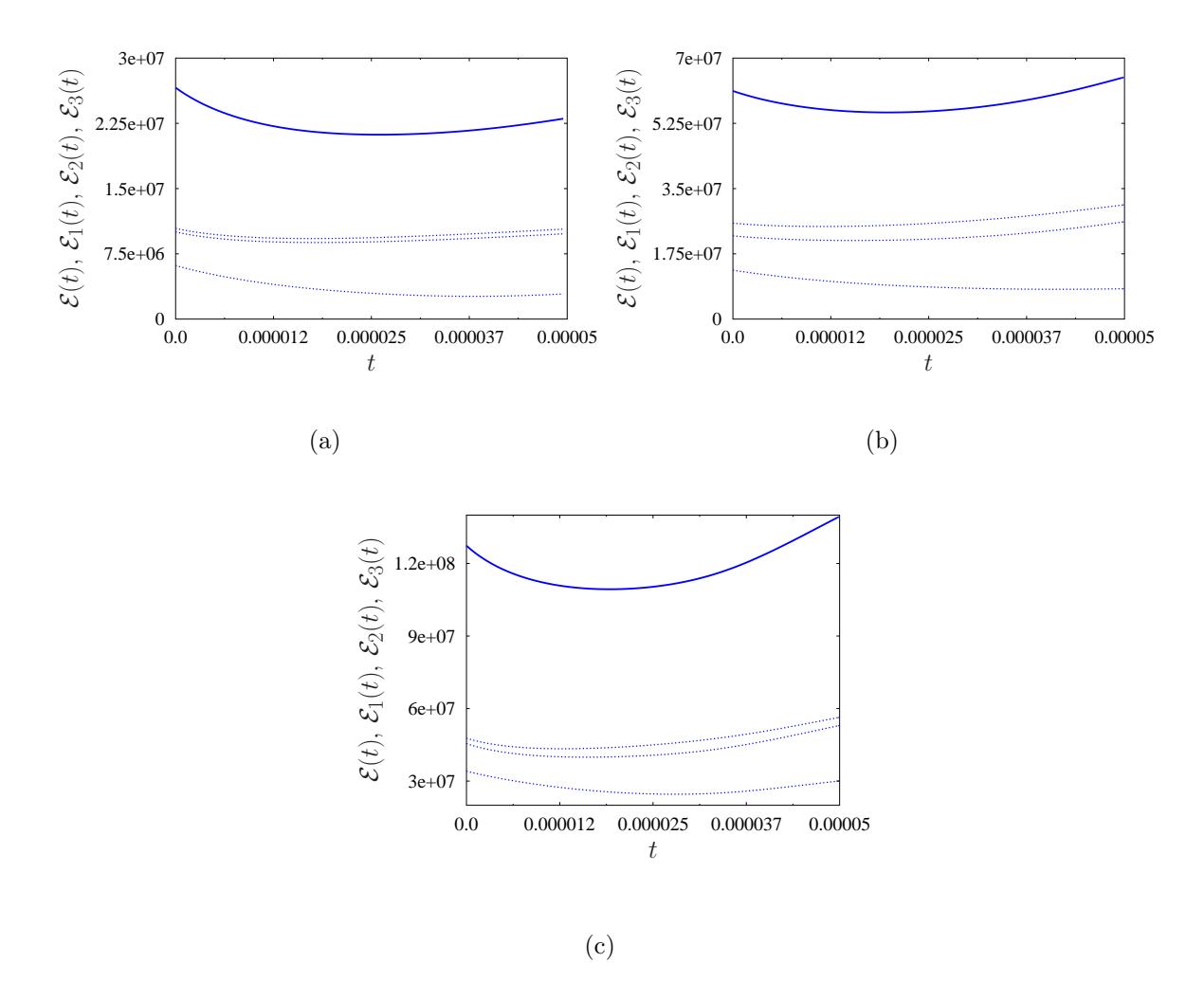


Figure 5.42: [q=3, Problem 3] Evolution of (solid lines) the total enstrophy  $\mathcal{E}(t)$  and (dotted lines) the componentwise enstrophies  $\mathcal{E}_1(t)$ ,  $\mathcal{E}_2(t)$  and  $\mathcal{E}_3(t)$  for optimal solutions of Problem 3. The values of the parameters are (a) B=53.18,  $T=5\times 10^{-5}$  (b) B=177.82,  $T=5\times 10^{-5}$  and (c) B=353.55,  $T=5\times 10^{-5}$ .

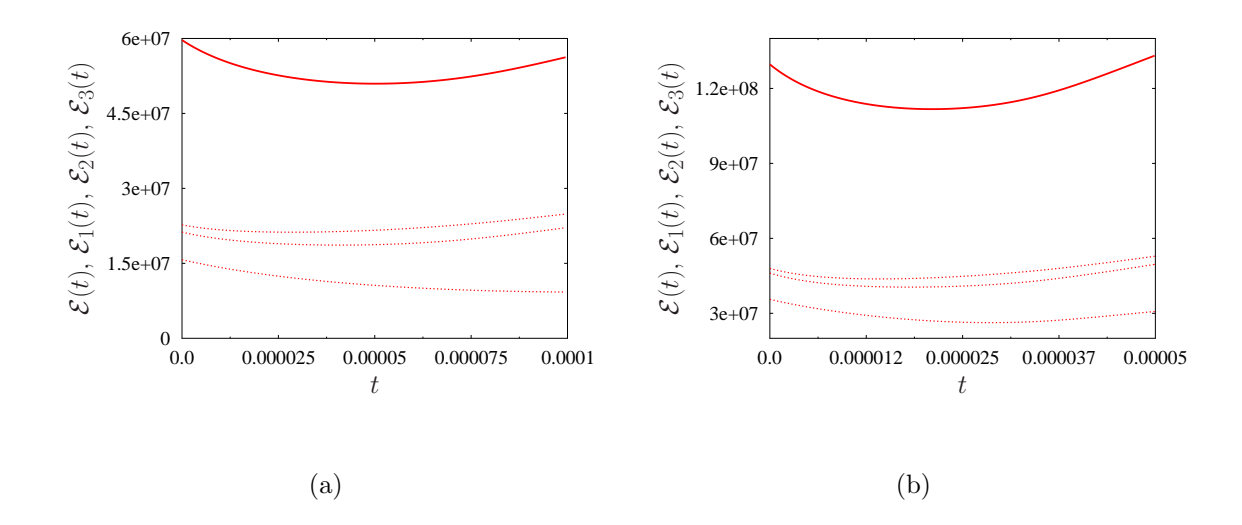


Figure 5.43: [q = 3, Problem 4] Evolution of (solid lines) the total enstrophy  $\mathcal{E}(t)$  and (dotted lines) the componentwise enstrophies  $\mathcal{E}_1(t)$ ,  $\mathcal{E}_2(t)$  and  $\mathcal{E}_3(t)$  for optimal solutions of Problem 4. The values of the parameters are (a) B = 562.34,  $T = 10^{-4}$  and (b) B = 707.10,  $T = 5 \times 10^{-5}$ .

norm. The gold trajectory is particularly interesting because it appears to grow in proportion to the upper bound on the rate of change of the enstrophy represented by the black solid line. We then reach a similar conclusion that only a few solutions of the Navier-Stokes system (1.1), corresponding to the optimal initial conditions obtained by solving Problems 3 and 4, fall into the potential blow-up regime. Nevertheless, this behavior does not persist long enough to trigger a singularity. This time, however, there are considerably fewer such trajectories.

#### 5.4.2 Structure of the Extremal Flows

We will now discuss the structure of the extremal flows belonging to the different branches shown in Figure 5.40(a). Figures 5.42 and 5.43 show the time evolution of the componentwise enstrophies (5.3) for different values of the constraint parameter B in solutions of Problems 3 and 4, respectively. The time window in each panel corresponds

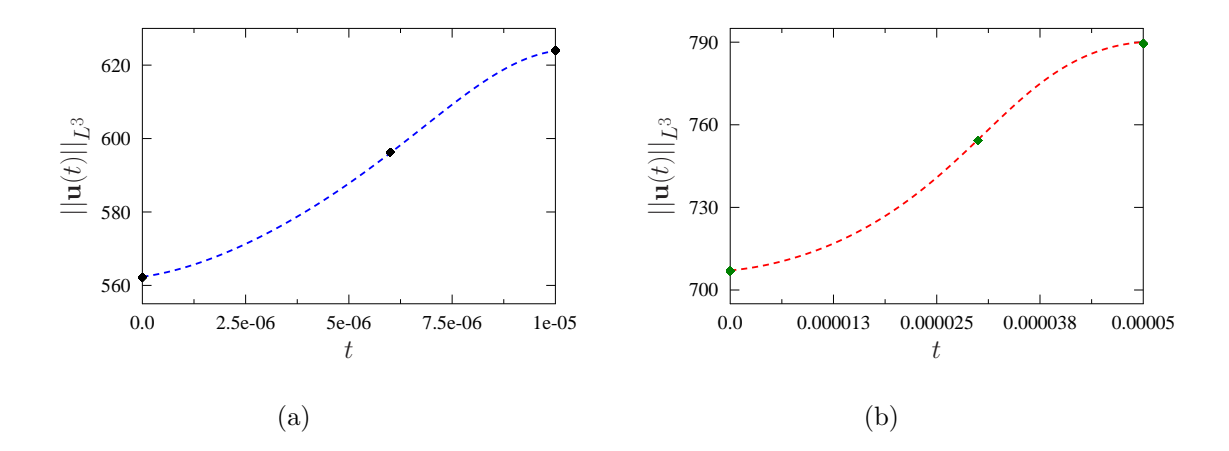


Figure 5.44: [q=3] Time evolution of the norm  $\|\mathbf{u}(t)\|_{L^3}^3$  in the flow with the optimal initial condition that produces the maximum value of the objective functional for solutions of (a) Problem 3, and (b) Problem 4. Black and green symbols represent the time instances  $t_i$ , i=0,...,2, in Definition 5.1, when the flow is visualized in Figures 5.46 and 5.45. The parameter values are (a) B=562.34 and  $T=10^{-5}$ , and (b) B=707.10 and  $T=5\times 10^{-5}$ .

to when the objective functional reaches its maximum on each branch. Unlike in Figures 5.11, 5.24 and 5.34,  $t_3$  as defined in Definition 5.1 does not appear in Figure 5.44. This is because of the form of the objective functional (3.9) in the limiting case. Since it involves the  $L^3(\Omega)$  norm at the terminal point t = T, it is natural that the maximum of the  $L^3(\Omega)$  norm is attained at or very close to the end point t = T. Therefore, in this case  $t_2 \sim t_3$  in Definition 5.1.

The flow structures shown in Figure 5.46 are quite similar to what we obtained in the case q = 4 (see Figure 5.12); both cases were obtained by solving the optimization problem over a Lebesgue space. We observe a bent vortex ring that stretches as time evolves. As before, we note that the maxima of  $|\mathbf{u}(\mathbf{x},t)|^3$  occur within the gap formed by the vortex ring as it entangles and these are precisely the regions driving the growth of the objective functional (3.9). It is likely that such similarity is related to the fact

that the gradient descent method converges within a few iterations. As regards the solutions of Problem 3, the time evolution of the vorticity is shown in Figure 5.45.

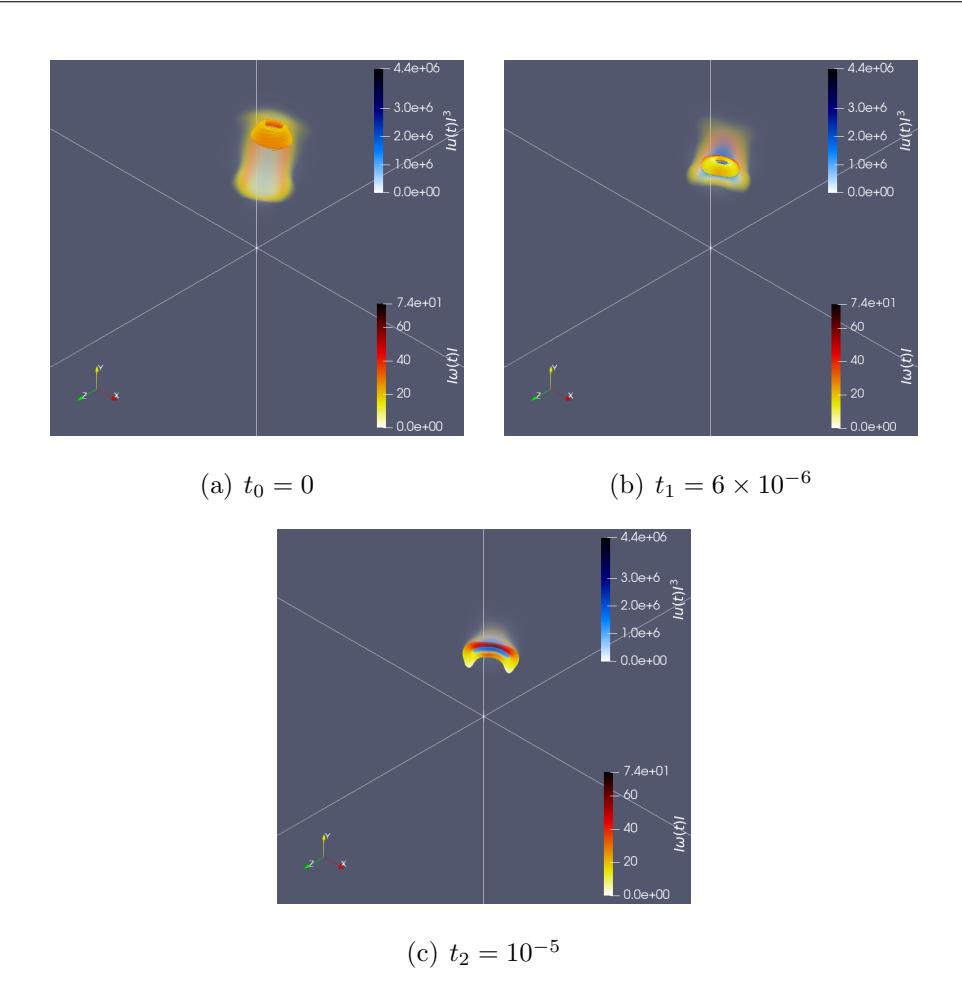


Figure 5.45:  $[q = 3, Problem 3, B = 562.34 \text{ and } T = 10^{-5}]$  Snapshots of the magnitude of the vorticity  $|\boldsymbol{\omega}(\mathbf{x}, t_i)|$  (red) in the solution of the Navier-Stokes system (1.1) along with vortex lines (red) and the quantity  $|\mathbf{u}(\mathbf{x}, t_i)|^3$  shown at the times  $t_0, ..., t_2$  defined in Definition 5.1. The values of the parameters B and T correspond to the gold trajectory in Figure 5.41(b).

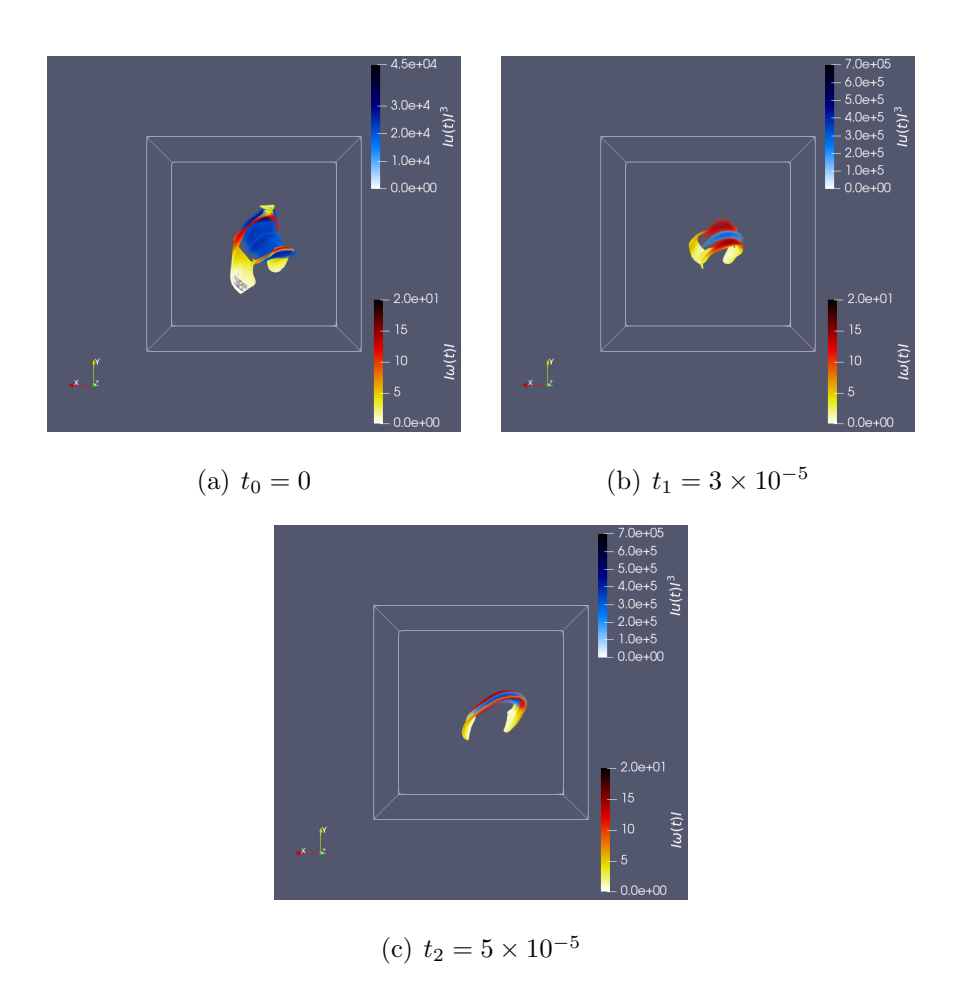


Figure 5.46:  $[q = 3, \text{ Problem 4}, B = 707.10 \text{ and } T = 5 \times 10^{-5}]$  Time evolution of the vorticity's magnitude  $|\boldsymbol{\omega}(\mathbf{x}, t_i)|$  (red) of the solution of the Navier-Stokes system (1.1) shown at the times  $t_0, ..., t_2$  defined in Definition 5.1. The values of the parameters B and T correspond to the green trajectory in Figure 5.41(a).

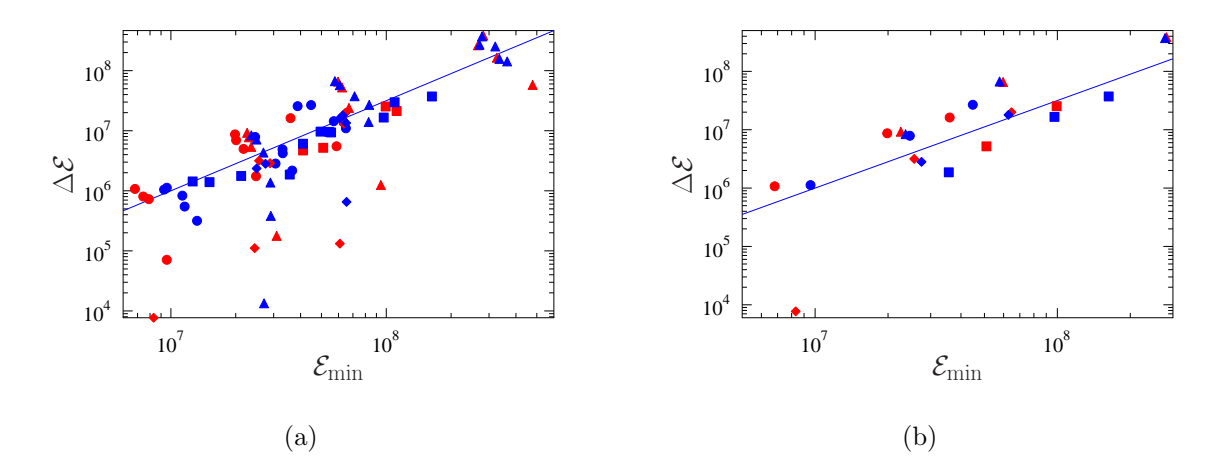


Figure 5.47: Dependence of  $\Delta \mathcal{E}$  defined in (5.13) on the initial enstrophy  $\mathcal{E}_0$  in Navier-Stokes flows with the optimal initial conditions constructed in (blue) a Sobolev space, i.e., solutions of Problems 1 and 3, and in (red) a Lebesgue space, i.e., solutions of Problems 2 and 4. Each symbol corresponds to a different value of q, (squares) q = 3, (circles) q = 4, (triangles) q = 5 and (diamonds) q = 9. Solid blue straight lines represent the relation  $\max_{t\geq 0} \mathcal{E}(t) \sim C\mathcal{E}_0^{3/2}$  with different values of C. Panel (b) shows a subset of points from Panel (a), where each point corresponds to the maximum value per branch taken from Figures 5.6(a), 5.20(a), 5.30 and 5.40(a).

#### 5.5 Diagnostic Quantities in the Extremal Flows

In this section we consolidate all the data obtained in this study to identify some general trends. First, we focus on quantifying the maximum growth of the enstrophy. It is important to note that, unlike in the work of Kang et al. in [29], the enstrophy was not directly controlled (via imposed constraints) in this investigation, therefore, what we observe here is an outcome of optimization performed while constraining other quantities (the  $L^q(\Omega)$  norms). A similar approach to analyzing the enstrophy growth using initial conditions from the solutions to Problems 1, 2, 3 and 4 involves defining

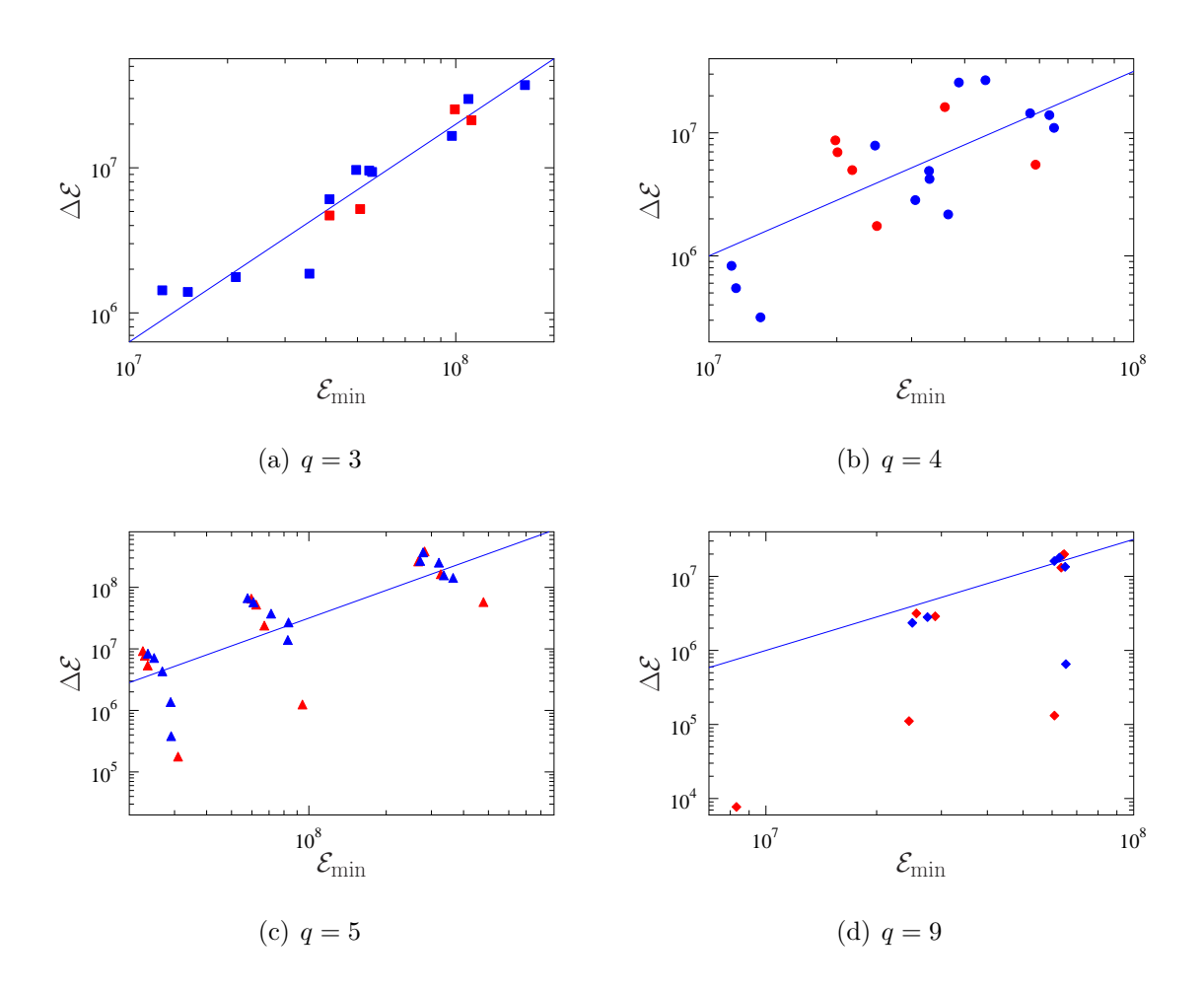


Figure 5.48: Dependence of  $\Delta \mathcal{E}$  (5.13) on the initial enstrophy  $\mathcal{E}_0$  in Navier-Stokes flows with the optimal initial conditions constructed in (blue) solutions in a Sobolev space, i.e., solutions to Problems 1 and 3 and in (red) a Lebesgue space, i.e., solutions to Problems 2 and 4. Each panel shows a subset of points from Figure 5.47(a) associated to different values of q, (a) q = 3, (b) q = 4, (c) q = 5, and (d) q = 9. Straight lines represent the relation  $\max_{t\geq 0} \mathcal{E}(t) \sim C\mathcal{E}_0^{3/2}$  with different values of C.

the following quantity

$$\Delta \mathcal{E} := \max_{t \in \left[ \operatorname{argmin}_{s \in [0,T]} \mathcal{E}(s), T \right]} \mathcal{E}(t) - \mathcal{E}_{\min}, \tag{5.13}$$

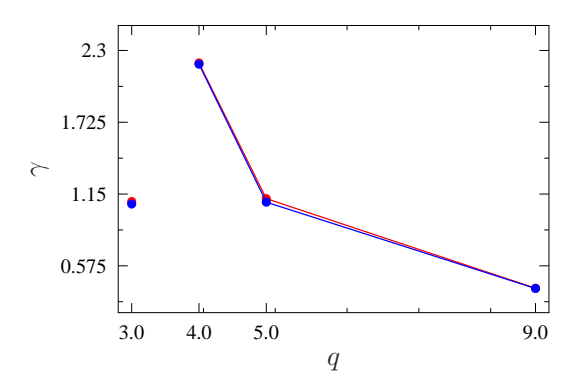


Figure 5.49: Dependence of the exponent  $\gamma$  in expression (5.4) on the value of q for flows with optimal initial conditions constructed in (blue) a Sobolev space, i.e., solutions of Problems 1 and 3 and in (red) a Lebesgue space, i.e., solutions of Problems 2 and 4.

where

$$\mathcal{E}_{\min} := \min_{t \in [0,T]} \mathcal{E}(t). \tag{5.14}$$

The value of  $\Delta \mathcal{E}$  therefore captures the growth of the enstrophy from its lowest value during the flow evolution to its maximum. The definition of  $\Delta \mathcal{E}$  is motivated by Figures 5.5, 5.19, and 5.39 where an initial decay in the enstrophy is followed by a prominent increase. Interestingly, we observe in Figure 5.47 that the variation of the enstrophy  $\Delta \mathcal{E}$  seems to follows the relation  $\max_{t\geq 0} \mathcal{E}(t) \sim C\mathcal{E}_0^{3/2}$  described by Ayala & Protas in [5] and Kang et al. in [29]. However, this trend seems to be mostly realized by the cases q=3 and q=5 as shown in Figures 5.48(a) and 5.48(c). The cases q=4 and q=9, shown in Figures 5.48(b) and 5.48(d), seem to follow a slightly steeper relation, however, more data is necessary to confirmed this finding.

Finally, in Figure 5.49 we show how the exponent  $\gamma$  in expression (5.4) depends on the parameter q. We observe a decreasing trend in  $\gamma$  for values of q greater than 3. The change of the trend at q=3 might be due to the fact that the this case employs a different objective functional. We confirm that the value of  $\gamma$  obtained in this study for q=4 is consistent with the result reported by Kang & Protas in [28]. It is interesting

that the values of  $\gamma$  for q=5 and q=3 are quite similar and are approximately half smaller than the value of  $\gamma$  for q=4.

#### Chapter 6

## **Summary and Conclusions**

In this thesis, we conducted an extensive search for singularities in Navier-Stokes flows on a periodic domain using a systematic computational approach. We solved a series of PDE-constrained optimization problems based on the LPS conditions (2.27), where we sought initial conditions  $\tilde{\mathbf{u}}_0$  such that the corresponding Navier-Stokes flows maximize the objective functionals (3.1) and (3.9). Those initial conditions were determined in the Sobolev-Hilbert spaces  $H^s(\Omega)$  (see Problems 1 and 3) and Lebesgue spaces  $L^q(\Omega)$ (see Problems 2 and 4). The latter case was particularly challenging due to the lack of an inner product structure on top of the lack of regularity. To solve these optimization problems, we used the "optimize-then-discretize" approach involving a state-of-the-art adjoint-based Riemannian gradient method (4.5) and (4.7). However, the solution of Problems 2 and 4 required a novel approach using metric gradients [23], and even in this new setup where we search for extreme flows, we found no evidence of unbounded growth of the quantities of interest, and thus, no indication of singularity formation. This research is a continuation of a series of earlier studies where a systematic computational search for singularities in the Navier-Stokes system (1.1) was conducted based on different regularity conditions [34, 8, 29, 47, 28]. In our study, we considered different values of the Lebesgue exponent q (3, 4, 5 and 9), different "sizes" of the initial data B

and several time windows T. Then, given q, we chose s as the index that makes  $H^s(\Omega)$  the largest Sobolev-Hilbert space embedded in  $L^q(\Omega)$  (Theorem 2.1) to solve Problems 1 and 3.

The flows with initial data constructed in Sobolev spaces, i.e., solutions of Problems 1 and 3, were found to lead to larger values of the objective functional (3.1) as compared to flows with initial data constructed in Lebesgue spaces, i.e., solutions of Problems 2 and 4 for all the considered values of q (see Figures 5.6, 5.20, 5.30 and 5.40). This is a counterintuitive result since optimal initial conditions in Problems 2 and 4 are sought in a "larger" space. An intuitive result, though, is that the optimal initial conditions obtained in Problems 2 and 4 are considerably less regular than those from Problems 1 and 3, respectively (see Figures 5.2(a), 5.3(a), 5.16(a), and 5.17(a)). Additionally, we found numerically that local maximizers of Problems 1 and 3 are also local maximizers of Problems 2 and 4, respectively. However, the converse is not true. This observation can be rigorously justified as the following theorem

**Theorem 6.1.** Consider the following optimization problems defined on the Banach spaces X and Y,

$$\max_{\mathbf{z} \in X} \varphi(\mathbf{z}) \tag{P1}$$

and,

$$\max_{\mathbf{z} \in Y} \boldsymbol{\varphi}(\mathbf{z}),\tag{P2}$$

where X is densely embedded in Y and  $\varphi(\mathbf{z})$  is a Fréchet differentiable objective functional defined on X and Y. If  $\mathbf{z}_0$  is a local solution of (P1), then  $\mathbf{z}_0$  is also a local solution of (P2).

Although Problems 1–4 are constrained, we can always write them as unconstrained problems using Lagrange multipliers, and then invoke Theorem 6.1. The proof of this theorem is in Appendix B.

We explored several ways to solve Problems 1–4, and also derived a Riemannian conjugate-gradient method to solve optimization problems formulated in Banach spaces (see Section 4.6). The motivation behind this effort was that conjugate-gradient methods have demonstrated better performance than gradient descent methods, even in infinite-dimensional spaces [14, 59]. However, in our case, we did not observe any noticeable improvement in performance in either the number of iterations required to converge or the structure of the optimal solution reflected in the values of the objective functionals (3.1) and (3.9). Therefore, for simplicity, we decided to continue using the Riemannian gradient descent method rather than the Riemannian conjugate-gradient method. Although our study did not directly benefit from this approach, the method we introduced could be applicable to other optimization problems posed on infinite-dimensional Banach spaces. Recent applications of such type include, for example, image recovery problems [30].

After a comprehensive search for extreme behavior by varying the parameters q, B and T, we constructed maximizing branches for Problems 1 and 2 illustrated in Figures 5.6, 5.20, 5.30. Additionally, Figure 5.40 shows the maximizing branches from solutions to Problems 3 and 4. Even though the values of the objective functionals (3.1) and (3.9) are large, we found no evidence of unbounded growth of the quantities represented by the objective functionals. This conclusion is supported by the observation that the objective functionals begin to decay for longer time windows T. To understand the dynamics of the solutions of the Navier-Stokes system (1.1) with initial conditions given by the optimal solutions of Problems 1–4, we studied the diagnostic quantities  $\|\mathbf{u}(t)\|_{L^q(\Omega)}$  and the enstrophy  $\mathcal{E}(t)$ . In Figures 5.4, 5.18, 5.28(a) and 5.38, we observe a rapid growth of  $\|\mathbf{u}(t)\|_{L^q(\Omega)}$  driven by the nonlinear term followed by a decay as a result of the dominance of the dissipative term. Similarly, Figures 5.5, 5.19, 5.29(a) and 5.39 show the evolution of the enstrophy normalized with the initial enstrophy  $\mathcal{E}_0$ . Here, we observe that in most of the cases, the enstrophy starts decreasing initially but this is

then followed by a rapid growth if the parameters T and B are "large" enough.

Symmetry of the velocity field, introduced in Table 5.1, is a feature defined based on the behavior of its componentwise enstrophy (2.7). If the componentwise enstrophies are similar in both magnitude and monotonicity, the velocity field is considered symmetric; otherwise, it is considered nonsymmetric. Interestingly, the solutions of Problem 1 and 3 are nonsymmetric flows across different values of q (see Figures 5.6, 5.20, 5.30 and 5.40). However, solutions to Problem 2 can be either symmetric or nonsymmetric flows. Regarding the solutions of Problem 4, they were found to be nonsymmetric. Additionally, for the cases where symmetric and nonsymmetric velocity fields were found, the nonsymmetric branches yielded higher values in the objective functional. This is consistent with Kang's & Protas' findings in [28]. Additionally, we noticed that the values of the objective functional obtained using random initial guesses in iterations (4.5) were comparable with the values presented in Figures 5.6, 5.20, 5.30, and 5.40.

In expression (2.37), we presented explicit bounds for the rate of growth of the  $L^q(\Omega)$  norm of solutions to the Navier-Stokes system (1.1) that have bounded norm at all times. By combining these results with a priori bounds on the rate of growth of the  $L^q(\Omega)$  from expression (2.31), we identify regimes in terms of the rate of growth of the  $L^q(\Omega)$  norm in which the solutions to the Navier-Stokes equations must lie in order to develop a singularity, provided that the growth of the  $L^q(\Omega)$  norm is sustained over a sufficiently long time. These regimes are presented in Figure 2.1. We observe a significant transient growth of both the  $L^q(\Omega)$  norm and of the enstrophy for all the studied values of q in Figures 5.7, 5.21, 5.31 and 5.41. However, the growth of the  $L^q(\Omega)$  norm was not sustained long enough to lead to singularity formation in a finite time. Although we did not work with parameters that allow us to control the enstrophy, in Figures 5.7, 5.21, 5.31 and 5.41 we did observe trajectories corresponding to solutions of Problems 1–4 where the rate of growth of the enstrophy fell into the regime where a singularity could form. However, similarly to what was observed for the  $L^q(\Omega)$  norm,

this growth was not sustained for a sufficiently long time to trigger a singularity.

It is interesting that the optimal solutions of Problems 1–4 can share some similarities in terms of their flow structure, despite being obtained over different function spaces and with distinct objective functionals. For example, consider Figures 5.13 and 5.14, which visualize the flow fields obtained as solutions of Problems 1 and 2, respectively. They present the quantities  $|\omega(\mathbf{x},t)|$  and  $|\mathbf{u}(\mathbf{x},t)|^4$  at the time instances  $t_i$  given in Definition 5.1. Both figures show the formation of two flat vortex tubes that enclose a region contributing most to the value of the objective functional (3.1). Another interesting flow structure, observed in problems solved with different values of q, is a bent vortex tube, as shown in Figures 5.12 and 5.46. These figures visualize the flow fields obtained as solutions of Problems 1 and 4, respectively. Although they represent optimal solutions constructed in spaces with different topologies, the vortex tube remains confined in both cases. However, there are other cases in which the tube stretches across the entire domain, as seen in Figure 5.36, which corresponds to solutions of Problem 2. These appear to be the two predominant structures in the extreme flows corresponding to the optimal initial conditions obtained by solving Problems 1–4, for different values of q.

Another interesting finding is related to the scaling of the maximum attained enstrophy in terms of the initial enstrophy  $\mathcal{E}_0$ . Although this relation is presented in a different way to what Ayala & Protas in [5] and Kang et al. in [28] did, we observed that the maximum variation of the enstrophy  $\Delta \mathcal{E}$  (5.13) also scales as  $C\mathcal{E}_0^{\frac{3}{2}}$ . This behavior is especially evident for the cases q = 3 and q = 5 (see Figure 5.48). The reason for introducing  $\Delta \mathcal{E}$  was the need to measure the total enstrophy growth since, in most cases, the enstrophy initially decreased and growth occurred only after certain period of time.

We acknowledge that the approach of searching for singularities by solving Problems 1, 2, 3 or 4 has several limitations. From one side, we have the inability to distinguish

between local and global maximizers, which is an inherent issue when solving nonconvex optimization problems such as Problems 1, 2, 3 or 4. On the other hand, we have the computational cost of the numerical method used to solve the PDE problems. A solution of Problem 1, 2, 3 or 4 with typical values of the parameters B and T would take several days to complete while using  $\mathcal{O}(10) - \mathcal{O}(100)$  CPUs, and refining the resolution globally would lead to even longer computation times. However, overcoming these limitations offers valuable directions for future studies. For example:

- The use of a different numerical method, such as a variant of an adaptive finiteelement or finite-difference method that allows for local refinements, rather than the uniform refinements used currently, could improve computational efficiency while maintaining accuracy in regions of interest. This would be particularly beneficial for capturing small-scale features of the extreme solutions.
- Exploring extreme solutions to Problem 5 in Sobolev spaces  $W^{n,q}(\Omega)$  for n, q > 1.
- Solving Problems 1–4 over nontrivial, non-slip, bounded domains.
- Solving analogous optimization problems for 3D Euler equations where, unlike the Navier-Stokes system (1.1), there is numerical evidence of singularity formation using smooth initial data in specific domains [26, 59].

## Appendix A

# Rederivation of Inequality (2.31)

In this appendix we derive inequality (2.31) following Robinson's and Sadowski's work [50]. First, multiplying the momentum equation (1.1a) by  $\mathbf{u}|\mathbf{u}|^{q-2}$  and integrating in space, we obtain

$$\int_{\Omega} \mathbf{u}_t \cdot \mathbf{u} |\mathbf{u}|^{q-2} d\mathbf{x} - \int_{\Omega} \Delta \mathbf{u} \cdot \mathbf{u} |\mathbf{u}|^{q-2} d\mathbf{x} + \int_{\Omega} (\mathbf{u} \cdot \nabla) \mathbf{u} \cdot \mathbf{u} |\mathbf{u}|^{q-2} d\mathbf{x} = -\int_{\Omega} \nabla p \cdot \mathbf{u} |\mathbf{u}|^{q-2} d\mathbf{x}.$$

Now, we will analyze all terms, starting with the first one on the left-hand side,

$$\int_{\Omega} \mathbf{u}_t \cdot \mathbf{u} |\mathbf{u}|^{q-2} d\mathbf{x} = \frac{1}{q} \frac{d}{dt} \int_{\Omega} |\mathbf{u}|^q d\mathbf{x}.$$
 (A.1)

The second term of the left hand side can be bounded using Lemma 1 in [50] as

$$-\int_{\Omega} \Delta \mathbf{u} \cdot \mathbf{u} |\mathbf{u}|^{q-2} d\mathbf{x} \ge \int_{\Omega} |\nabla \mathbf{u}|^2 |\mathbf{u}|^{q-2} d\mathbf{x}. \tag{A.2}$$

The third term on the left-hand side vanishes since

$$\int_{\Omega} (\mathbf{u} \cdot \mathbf{\nabla}) \mathbf{u} \cdot \mathbf{u} |\mathbf{u}|^{q-2} d\mathbf{x} = \frac{1}{2} \int_{\Omega} |\mathbf{u}|^{q-2} \mathbf{\nabla} |\mathbf{u}|^{2} \cdot \mathbf{u} d\mathbf{x}$$

$$= \frac{1}{q} \int_{\Omega} \mathbf{\nabla} |\mathbf{u}|^{q} \cdot \mathbf{u} d\mathbf{x}$$

$$= -\frac{1}{q} \int_{\Omega} |\mathbf{u}|^{q} (\mathbf{\nabla} \cdot \mathbf{u}) d\mathbf{x} \quad \text{(integration by parts)}$$

$$= 0.$$
(A.3)

The right-hand side term.

$$-\int_{\Omega} \boldsymbol{\nabla} p \cdot \mathbf{u} |\mathbf{u}|^{q-2} d\mathbf{x} = \int_{\Omega} p \, \mathbf{u} \cdot \boldsymbol{\nabla} |\mathbf{u}|^{q-2} d\mathbf{x} \qquad \text{(integration by parts)}$$

$$= \frac{q-2}{2} \int p \, |\mathbf{u}|^{q-4} \mathbf{u} \cdot \boldsymbol{\nabla} |\mathbf{u}|^2 d\mathbf{x}$$

$$\leq \frac{q-2}{2} \int |p| \, |\mathbf{u}|^{q-4} |\mathbf{u} \cdot \boldsymbol{\nabla} |\mathbf{u}|^2 | d\mathbf{x}$$

$$\leq \frac{q-2}{2} \int |p| \, |\mathbf{u}|^{q-4} |\mathbf{u} \cdot \boldsymbol{\nabla} |\mathbf{u}|^2 | d\mathbf{x}$$

$$\leq (q-2) \int |p| \, |\mathbf{u}|^{q-4} |\mathbf{v} \cdot \boldsymbol{\nabla} |\mathbf{u}|^2 | d\mathbf{x} \qquad \text{since } |\mathbf{u} \cdot \boldsymbol{\nabla} |\mathbf{u}|^2 | \leq 2|\mathbf{u}|^2 |\boldsymbol{\nabla} \mathbf{u}|$$

$$\leq \int_{\Omega} |\mathbf{u}|^{q-2} \left( \frac{(q-2)^2 |p|^2}{2} + \frac{|\boldsymbol{\nabla} \mathbf{u}|^2}{2} \right) d\mathbf{x} \qquad \text{(Young's inequality)}$$

$$= \frac{(q-2)^2}{2} \int_{\Omega} |\mathbf{u}|^{q-2} |p|^2 d\mathbf{x}$$

$$+ \frac{1}{2} \int_{\Omega} |\mathbf{u}|^{q-2} |\boldsymbol{\nabla} \mathbf{u}|^2 d\mathbf{x}. \qquad (A.4)$$

To estimate the pressure term, we proceed as follows

$$\frac{(q-2)^{2}}{2} \int_{\Omega} |\mathbf{u}|^{q-2} |p|^{2} d\mathbf{x} \leq \frac{(q-2)^{2}}{2} ||p||_{L^{q}}^{2} ||\mathbf{u}||_{L^{q}}^{q-2} \qquad (\text{H\"older's inequality})$$

$$\leq c ||\mathbf{u}||_{L^{q}}^{4} ||\mathbf{u}||_{L^{q}}^{q-2} \qquad (\text{Lemma 3 in [50]})$$

$$\leq c ||\mathbf{u}||_{L^{q}}^{q-1} ||\mathbf{u}||_{L^{3q}}^{3}, \qquad (\text{Lebesgue interpolation})$$

$$||\mathbf{u}||_{L^{2q}} \leq ||\mathbf{u}||_{L^{q}}^{1/4} ||\mathbf{u}||_{L^{3q}}^{3/4}$$

$$\leq c_{1} ||\mathbf{u}||_{L^{q}}^{q(q-1)/(q-3)} + \frac{1}{2c_{2}} ||\mathbf{u}||_{L^{3q}}^{q}$$

$$\leq c_{1} ||\mathbf{u}||_{L^{q}}^{q(q-1)/(q-3)} + \frac{1}{2} \int_{\Omega} |\mathbf{u}|^{q-2} |\nabla \mathbf{u}|^{2} d\mathbf{x}.$$

$$(A.5)$$

Combining equalities (A.1) and (A.3) with estimates (A.2), (A.4) and (A.5), we obtain inequality (2.31)

$$\frac{d}{dt} \|\mathbf{u}(t)\|_{L^{q}(\Omega)} \le C \|\mathbf{u}(t)\|_{L^{q}(\Omega)}^{\frac{3(q-1)}{q-3}}, \quad q > 3.$$
(A.6)

#### Appendix B

#### Proof of Theorem 6.1

In this appendix we prove Theorem 6.1.

Proof:

Suppose that  $\mathbf{z}_0 \in X$  is a local solution of (P1). Therefore, it satisfies the optimality condition

$$\varphi'(\mathbf{z}_0, \mathbf{w}') = \lim_{\epsilon \to 0} \frac{\varphi(\mathbf{z}_0 + \epsilon \mathbf{w}') - \varphi(\mathbf{z}_0)}{\epsilon} = 0, \text{ for all } \mathbf{w}' \in X.$$
 (B.1)

We wish to verify that the following optimality condition holds as well

$$\varphi'(\mathbf{z}_0, \mathbf{z}') = \lim_{\epsilon \to 0} \frac{\varphi(\mathbf{z}_0 + \epsilon \mathbf{z}') - \varphi(\mathbf{z}_0)}{\epsilon} = 0, \text{ for all } \mathbf{z}' \in Y.$$
 (B.2)

Since  $\varphi$  is a Fréchet differentiable functional on Y,  $\varphi'(\mathbf{z}, \cdot)$  is a bounded linear operator (and hence continuous) for every  $\mathbf{z} \in Y$ . Given that X is dense in Y, then every  $\mathbf{z}' \in Y$  can be approximated with a sequence of elements in X i.e., there exists a sequence  $\{\mathbf{z}'_n\}_{n\in\mathbb{N}}$  in X such that

$$\lim_{n\to\infty}\mathbf{z}'_n=\mathbf{z}'.$$

In particular, we have that for any  $n \in \mathbb{N}$  expression (B.1) implies

$$0 = \lim_{n \to \infty} 0 = \lim_{n \to \infty} \lim_{\epsilon \to 0} \frac{\varphi(\mathbf{z}_0 + \epsilon \mathbf{z}'_n) - \varphi(\mathbf{z}_0)}{\epsilon}$$

$$= \lim_{n \to \infty} \varphi'(\mathbf{z}_0, \mathbf{z}'_n)$$

$$= \varphi'(\mathbf{z}_0, \lim_{n \to \infty} \mathbf{z}'_n) \quad \text{(By the continuity of } \varphi'\text{)}$$

$$= \varphi'(\mathbf{z}_0, \mathbf{z}').$$

Hence,  $\mathbf{z}_0$  is also a local solution of Problem (P2).

# Appendix C

#### Validation of the Gradients

The purpose of this section is to validate the computation of the  $L^2$  gradient of the objective functionals (3.1) and (3.9). This is a key step to ensure the correct evaluation of the gradient in the Lebesgue spaces  $L^q(\Omega)$ ,  $q \geq 3$  and the Sobolev-Hilbert spaces  $H^s(\Omega)$ . To do so, we compute the quantities

$$\kappa_1(\epsilon) = \frac{\epsilon^{-1} \left[ \Psi_T(\mathbf{u}_0 + \epsilon \mathbf{u}_0') - \Psi_T(\mathbf{u}_0) \right]}{\left\langle \nabla^{L^2} \Psi_T, \mathbf{u}_0' \right\rangle}, \quad \epsilon > 0,$$
 (C.1)

and

$$\kappa_2(\epsilon) = \frac{\epsilon^{-1} \left[ \Phi_T^q(\mathbf{u}_0 + \epsilon \mathbf{u}_0') - \Phi_T^q(\mathbf{u}_0) \right]}{\left\langle \nabla^{L^2} \Phi_T^q, \mathbf{u}_0' \right\rangle}, \quad \epsilon > 0, \ q > 3,$$
 (C.2)

with fixed vector fields  $\mathbf{u}_0$ ,  $\mathbf{u}'_0$ , time window T and several decreasing values of  $\epsilon$ . Numerators in (C.1)-(C.2) represent a first-order finite-difference approximation of the Gâteaux differential (4.8) while denominators are given by the Riesz form (4.9) of the Gateaux differentials. We then expect that  $\kappa_i(\epsilon) \approx 1$ , i = 1, 2, however, the evaluation of these quantities could give rise to a combination of three distinct types of errors:

• "Gradient errors" which are due to the discretization of the different PDE systems (1.1) and (4.13) in space and time. These errors are controlled by the time step  $\Delta t$  and the resolution N.

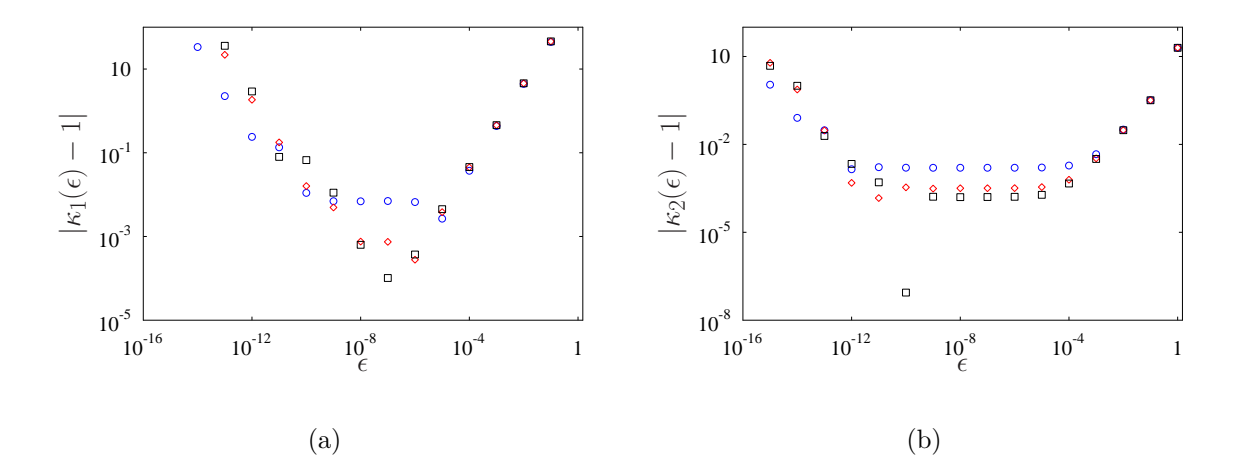


Figure C.1:  $[T=10^{-4}, N=128^3]$  Dependance of (a)  $|\kappa_1(\epsilon)-1|$  and (b)  $|\kappa_2(\epsilon)-1|$  on  $\epsilon$  is presented in logarithmic scale. Blue circles in (a) were obtained by evaluating expression C.1 with time step  $\Delta t = 10^{-4}$ , red diamonds with  $\Delta t = 10^{-5}$ , black squares with  $\Delta t = 10^{-6}$ , while the constraint parameter  $B^4$  is  $2 \times 10^{10}$ . Blue circles in (b) were obtained by evaluating expression C.2 with time step  $\Delta t = 5 \times 10^{-6}$ , red diamonds with  $\Delta t = 10^{-6}$ , black squares with  $\Delta t = 5 \times 10^{-7}$ , while the constraint parameter  $B^3$  is  $2 \times 10^8$ .

- Truncation errors that are triggered by the finite-difference formula in the numerators in (C.1)-(C.2). These errors are  $\mathcal{O}(\epsilon)$ .
- Round-off errors resulting from subtractive cancellation, which are of order  $\mathcal{O}(\epsilon^{-1})$ .

As explained in [39], the dependence of  $\log_{10}|\kappa_i(\epsilon) - 1|$  on  $\epsilon$  for i = 1, 2, exhibits a plateau-like shape and it is naturally divided into three regimes depending on the values of  $\epsilon$ . For "large" values of  $\epsilon$ , we observe that truncation errors dominate, while "small" values trigger round-off errors and for some intermediate values of  $\epsilon$  we observe gradient errors. To validate the evaluation of the  $L^2$  gradient, we want to show that the gradient errors vanish as the parameters  $\Delta t$  and N are refined. In our case, however, we fix the resolution N and vary only  $\Delta t$  since the truncation errors associated with  $\Delta t$ 

tend to be larger than those related to N. This behavior is manifested in the lowering of the plateau as  $\Delta t$  decreases.

Figures C.1(a) and C.1(b) show the dependance of  $|\kappa_i(\epsilon) - 1|$ , i = 1, 2 on  $\epsilon$  as the parameter  $\Delta t$  is refined. We observe that the values of  $\kappa_i(\epsilon)$ , i = 1, 2, diverge away from unity for both "small" and "large" values of  $\epsilon$  due to the round-off and truncation errors, respectively. However, for intermediate values of  $\epsilon$ , the gradient errors vanish as we refine  $\Delta t$ . This demonstrates that the accuracy of the  $L^2$  gradient computation improves as the time discretization is refined, thus providing the required validation.

## Bibliography

- [1] P.-A. Absil, R. Mahony, and R. Sepulchre. *Optimization Algorithms on Matrix Manifolds*. Princeton University Press, 2008.
- [2] R. Adams and J. Fournier. Sobolev Spaces. Elsevier, 2005.
- [3] D. Albritton, E. Brué, and M. Colombo. Non-uniqueness of Leray solutions of the forced Navier-Stokes equations. *Annals of Mathematics*, 196(1):415–455, 2022.
- [4] D. Ayala. Extreme Vortex States and Singularity Formation in Incompressible Flows. PhD thesis, McMaster University, 2014. available at http://hdl.handle.net/11375/15453.
- [5] D. Ayala and B. Protas. On maximum enstrophy growth in a hydrodynamic system. *Physica D*, 240:1553–1563, 2011.
- [6] D. Ayala and B. Protas. Maximum palinstrophy growth in 2D incompressible flows. *Journal of Fluid Mechanics*, 742:340–367, 2014.
- [7] D. Ayala and B. Protas. Vortices, maximum growth and the problem of finite-time singularity formation. *Fluid Dynamics Research*, 46(3):031404, 2014.
- [8] D. Ayala and B. Protas. Extreme vortex states and the growth of enstrophy in 3D incompressible flows. *Journal of Fluid Mechanics*, 818:772–806, 2017.

- [9] M. Berger. Nonlinearity and Functional Analysis. Academic Press, Cambridge, 1977.
- [10] T. Bewley. Numerical Renaissance. Renaissance Press, 2009.
- [11] M. Brachet. Direct simulation of three-dimensional turbulence in the Taylor-Green vortex. Fluid Dynamics Research, 8:1–8, 1991.
- [12] H. Brezis. Functional Analysis, Sobolev Spaces and Partial Differential Equations. Springer, 2011.
- [13] T. Buckmaster and V. Vicol. Nonuniqueness of weak solutions to the Navier-Stokes equation. *Annals of Mathematics*, 189(1):101–144, 2019.
- [14] I. Danaila and B. Protas. Computation of round states of the Gross-Pitaevskii functional via Riemannian optimization. SIAM Journal on Scientific Computing, 39(6):B1102–B1129, 2017.
- [15] C. Doering and J. Gibbon. Applied Analysis of the Navier-Stokes Equations. Cambridge University Press, 1995.
- [16] L. Escauriaza, G. Seregin, and V. Sverak.  $L_{3,\infty}$ -solutions of the Navier-Stokes equations and backward uniqueness. Russian Mathematical Surveys, 58(2):211–250, apr 2003.
- [17] L. Evans. Partial Differential Equations, volume 19 of Graduate Studies in Mathematics. American Mathematical Society, 1998.
- [18] C. Fefferman. Existence and smoothness of the Navier-Stokes equation. available at http://www.claymath.org/sites/default/files/navierStokes.pdf, 2000. Clay Millennium Prize Problem Description.
- [19] C. Foias, O. Manley, R. Rosa, and R. Temam. Navier-Stokes Equations and Turbulence. Cambridge University Press, 2001.

- [20] C. Foias and R. Temam. Gevrey class regularity for the solutions of the Navier-Stokes equations. *Journal of Functional Analysis*, 87:359–369, 1989.
- [21] U. Frisch. Turbulence: The Legacy of A.N. Kolmogorov. Cambridge University Press, 1995.
- [22] J. Gibbon. Weak and strong solutions of the 3D Navier-Stokes equations and their relation to a chessboard of convergent inverse length scales. *Journal of Nonlinear Science*, July 2018. (published on-line).
- [23] M. Golomb and R. Tampia. The metric gradient in normed linear spaces. Numerische Mathematik, 20:115–124, 1972.
- [24] M. Gunzburger. Perspectives in Flow Control and Optimization. SIAM, 2003.
- [25] E. Hopf. über die aufgangswertaufgave für die hydrodynamischen grundliechungen. Mathematische Nachrichten, (4):213–231, 1951.
- [26] T. Hou. Blow-up or no blow-up? a unified computational and analytic approach to 3D incompressible Euler and Navier-Stokes equations. Acta Numerica, pages 277–346, 2009.
- [27] T. Hou. Potentially singular behavior of the 3D Navier–Stokes equations. Foun-dations of Computational Mathematics, 23:2251–2299, 2022.
- [28] D. Kang and B. Protas. Searching for singularities in Navier–Stokes flows based on the Ladyzhenskaya–Prodi–Serrin conditions. *Journal of Nonlinear Science*, 32(6):81, 2022.
- [29] D. Kang, D. Yun, and B. Protas. Maximum amplification of enstrophy in three-dimensional Navier-Stokes flows. *Journal of Fluid Mechanics*, 893:A22, 2020.
- [30] Y. Kimura and K. Nakajo. The problem of image recovery by the metric projections in banach spaces. *Abstract and Applied Analysis*, 2013(1):817392, 2013.

- [31] A. Kiselev and O. Ladyzhenskaya. On the existence and uniqueness of the solution of the nonstationary problem for a viscous, incompressible fluid. *Izvestiya Akademii Nauk SSSR. Seriya Matematicheskaya*, 21(5):655–680, 1957.
- [32] J. Leray. Sur le mouvement d'un liquide visqueux emplissant l'espace. *Acta Mathematica*, 63(1):193–248, 1934.
- [33] J.-L. Lions. Quelques résultats d'existence dans des équations aux dérivées partielles non linéaires. Bulletin de la Société Mathématique de France, 87:245–273, 1959.
- [34] L. Lu and C. Doering. Limits on enstrophy growth for solutions of the threedimensional Navier-Stokes equations. *Indiana University Mathematics Journal*, 57:2693–2727, 2008.
- [35] D. Luenberger. Optimization by Vector Space Methods. John Wiley and Sons, 1969.
- [36] G. Luo and T. Hou. Potentially singular solutions of the 3D axisymmetric Euler equations. *Proceedings of the National Academy of Sciences*, 111(36):12968–12973, 2014.
- [37] G. Luo and T. Hou. Toward the finite-time blowup of the 3D incompressible Euler equations: a numerical investigation. SIAM: Multiscale Modeling and Simulation, 12(4):1722–1776, 2014.
- [38] T. Luo and E. Titi. Non-uniqueness of weak solutions to hyperviscous Navier-Stokes equations: on sharpness of J.-L. Lions exponent. Calculus of Variations and Partial Differential Equations, 59(3):92, 2020.
- [39] P. Matharu and B. Protas. Adjoint-based enforcement of state constraints in PDE optimization problems. *Journal of Computational Physics*, 517:113298, 2024.

- [40] J. Neuberger. Sobolev Gradients and Differential Equations. Springer, 2nd edition, 2010.
- [41] J. Nocedal and S. Wright. Numerical Optimization. Springer, 1999.
- [42] K. Ohkitani. Late formation of singularities in solutions to the Navier-Stokes equations. *Journal of Physics A: Mathematical and Theoretical*, 49(1):015502, dec 2016.
- [43] P. Orlandi, S. Pirozzoli, and G. Carnevale. Vortex events in Euler and Navier-Stokes simulations with smooth initial conditions. *Journal of Fluid Mechanics*, 690:288–320, 2012.
- [44] W. Press, B. Flannery, S. Teukolsky, and W. Vetterling. *Numerical Recipes*. Cambridge University Press, 1986.
- [45] G. Prodi. Un teorema di unicità per le equazioni di Navier-Stokes. *Annali di Matematica Pura ed Applicata*, 48(1):173–182, Dec 1959.
- [46] B. Protas. Adjoint-based optimization of PDE systems with alternative gradients. Journal of Computational Physics, 227:6490–6510, 2008.
- [47] B. Protas. Systematic search for extreme and singular behaviour in some fundamental models of fluid mechanics. *Philosophical Transactions of the Royal Society* A, 2022.
- [48] B. Protas, T. Bewley, and G. Hagen. A comprehensive framework for the regularization of adjoint analysis in multiscale PDE systems. *Journal of Computational Physics*, 195:49–89, 2004.
- [49] L. Richardson. Weather Prediction by Numerical Process. Cambridge University Press, 1922.

- [50] J. Robinson, J. Rodrigo, and W. Sadowski. A local smoothness criterion for solutions of the 3D Navier-Stokes equations. Rendiconti del Seminario Matematico della Università di Padova, 131:159–178, 2014.
- [51] J. Robinson, J. Rodrigo, and W. Sadowski. *The Three-Dimensional Navier-Stokes Equations: Classical Theory*. Cambridge University Press, 2016.
- [52] J. Serrin. On the interior regularity of weak solutions of the Navier-Stokes equations. Archive for Rational Mechanics and Analysis, 9(1):187–195, Jan 1962.
- [53] I. Stein. Conjugate gradient methods in Banach spaces. *Nonlinear Analysis*, 63:e2621–e2628, 2005.
- [54] T. Tao. Quantitative bounds for critically bounded solutions to the Navier-Stokes equations. arXiv:1908.04958, 2020.
- [55] L. N. Trefethen. Spectral Methods in Matlab. SIAM, 2000.
- [56] Y. Wang, S. Čanić, M. Bukač, C. Blaha, and S. Roy. Mathematical and computational modeling of poroelastic cell scaffolds used in the design of an implantable bioartificial pancreas. *Fluids*, 7(7), 2022.
- [57] Z. Xin, Y. Shi, Yu. Zhang, and Yi. Zhang. A one-way coupled Navier-Stokes-Serre model for simulating the generation and propagation of tsunami waves. Pure and Applied Geophysics, 2024.
- [58] D. Yun and B. Protas. Maximum rate of growth of enstrophy in solutions of the fractional Burgers equation. *Journal of Nonlinear Science*, 28(1):395–422, Feb 2018.
- [59] X. Zhao and B. Protas. Systematic search for singularities in 3D Euler flows. Journal of Nonlinear Science, 33(6):120, 2023.